LEVEL

RADC-TR-79-131
Final Technical Report
June 1979

A072379

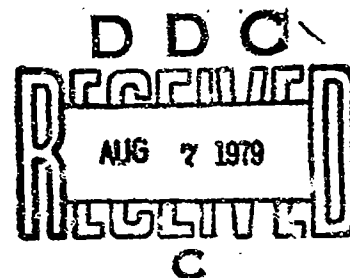# TURBULENCE ENVIRONMENT CHARACTERIZATION

AVCO Everett Research Laboratory, Inc.

M. G. Miller
P. L. Zieske

DDC
RECEIVED
AUG 7 1979
RECEIVED
C

APPROVED FOR PUBLIC RELEASE; DISTRIBUTION UNLIMITED

The views and conclusions contained in this document are those of
the authors and should not be interpreted as necessarily representing
the official policies, either expressed or implied, of the Defense
Advanced Research Projects Agency or the U. S. Government.

ROME AIR DEVELOPMENT CENTER
Air Force Systems Command
Griffiss Air Force Base, New York 13441

79 08 06 075

This report has been reviewed by the RADC Information Office (OI) and is releasable to the National Technical Information Service (NTIS). At NTIS it will be releasable to the general public, including foreign nations.

RADC-TR-79-131 has been reviewed and is approved for publication.

APPROVED: *Barry G Morgan*

BARRY G. MORGAN, Captain, USAF
Project Engineer

REPORT DOCUMENTATION PAGE	READ INSTRUCTIONS BEFORE COMPLETING FORM

1. REPORT NUMBER	2. GOVT ACCESSION NO.	3. RECIPIENT'S CATALOG NUMBER
RADC-TR-79-131		

4. TITLE (and Subtitle)	5. TYPE OF REPORT & PERIOD COVERED
TURBULENCE ENVIRONMENT CHARACTERIZATION	Final Technical Report, 15 Oct 75 - 30 Sep 78
	6. PERFORMING ORG. REPORT NUMBER
	N/A

7. AUTHOR(s)	8. CONTRACT OR GRANT NUMBER(s)
M. G. Miller P. L. Zieske	F30602-76-C-0054

9. PERFORMING ORGANIZATION NAME AND ADDRESS	10. PROGRAM ELEMENT, PROJECT, TASK AREA & WORK UNIT NUMBERS
AVCO Everett Research Laboratory, Inc. 2385 Revere Beach Parkway Everett MA 02149	62301E 26460115

11. CONTROLLING OFFICE NAME AND ADDRESS	12. REPORT DATE
Defense Advanced Research Projects Agency 1400 Wilson Blvd Arlington VA 22209	June 1979
	13. NUMBER OF PAGES
	133

14. MONITORING AGENCY NAME & ADDRESS(if different from Controlling Office)	15. SECURITY CLASS. (of this report)
Rome Air Development Center (OCSE) Griffiss AFB NY 13441	UNCLASSIFIED
	15a. DECLASSIFICATION/DOWNGRADING SCHEDULE N/A

16. DISTRIBUTION STATEMENT (of this Report)

Approved for public release; distribution unlimited.

17. DISTRIBUTION STATEMENT (of the abstract entered in Block 20, if different from Report)

Same

18. SUPPLEMENTARY NOTES
RADC Project Engineer: Captain Barry Morgan (OCSE)

19. KEY WORDS (Continue on reverse side if necessary and identify by block number)
Turbulence
Seeing
Atmospheric Optics

20. ABSTRACT (Continue on reverse side if necessary and identify by block number)

This report presents discussions of a variety of activities and results related to the characterization of atmospheric turbulence and its effects on optical propagation at the AMOS Observatory on Maui, Hawaii. The report is divided into two major parts.

The first part summarizes the measurements carried out during the entire program and presents an integrated view of the AMOS turbulence environment. Numerical values and the statistics of several optical parameters such as the

DD FORM 1473
1 JAN 73

79 08 06 075

Mutual Coherence Function correlation scale, (r_o), and the aperture averaged (36cm) log-amplitude variance are discussed. Furthermore, an averaged AMOS turbulent profile based on data from several different instrumental systems is defined. Values of optical parameters derived from this profile are in good agreement with their directly measured values. The most important conclusion drawn from this analysis is that sufficient information now exists to provide a consistent model of the average AMOS environment. However, due to a variety of short term behavior, the application of this model to the detailed operation of various systems should be approached with care.

The second part discusses the activities carried out during the period 1 October 1977 - 30 September 1978. Included is a discussion of experimental operations, instrumentation status and data reduction and analysis.

A detailed comparative study of profile derived and directly measured values of r_o demonstrate good agreement for long term averages but substantial dispersion for single night averages. The differences are thought to be due to atmospheric non-homogeneity, non-stationarity and the use of different spatial and temporal propagation paths.

The reprocessed model I Star Sensor data is in substantial agreement with model II data. While numerical values have changed, conclusions regarding the statistics of upper atmospheric turbulence remain the same. The noise characteristics of the model II device have been determined and a model which can be used to replace the calibration procedure has been generated.

A study of the angular dependence of r_o indicates that the data does not support the theoretical scaling law; however, a physically motivated two layer model does fit the data with modest success. Short term r_o data shows probable non-isotropy, non-stationarity and intermittency on time scales in the range from seconds to minutes.

A single, very limited RTAM data set was processed and analyzed. The resulting value of r_o is consistent with the simultaneous measurement made with the Seeing Monitor.

An average turbulent profile developed primarily from microthermal, acoustic sounder and Star Sensor data is quite consistent with directly measured optical parameters. Furthermore, the statistical variation of this profile has been estimated. While the profile shows a change in characteristic behavior in the vicinity of the tropopause, its shape significantly different than the Hufnagel wind correlated model. This may be due, in part, to the broad altitude weighing function inherent in the high altitude data.

The operation of the routine meteorological instrumentation, microthermal probes, acoustic sounder, Seeing Monitor and Star Sensor have been reduced to a routine level. Operational documentation and data transmittal procedures have been developed. This was the final step in establishing a routine resident capability which can be used in support of a variety of other programs and requirements.

TURBULENCE ENVIRONMENT CHARACTERIZATION

M. G. Miller
P. L. Zieske

PREFACE

This report is the final technical report submitted in compliance with the requirements of Contract F30602-76-C-0054 and covers work carried out during the period 15 October 1975 to 30 September 1978. In addition, a summary report covering the entire contract period is included. Details of earlier work are reported in RADC-TR-77-70 (March 1977), RADC-TR-77-232 (July 1977) and RADC-TR-78-72 (April 1978). Related work under a previous contract (F30602-75-C-0012) is reported in RADC-TR-75-185 (July 1975) and RADC-TR-76-189 (June 1976).

TABLE OF CONTENTS

4

LIST OF ILLUSTRATIONS

6

LIST OF TABLES

1.0 INTRODUCTION

1.1 BACKGROUND AND OBJECTIVES

Atmospheric turbulence can have significant effects on the operation of a variety of optical systems. The origin of these effects are small scale temperature fluctuations which contribute a random component to the index of refraction. Consequently, when an optical wave propagates through the atmosphere, a random phase is added to the wavefront. Provided the propagation path is of sufficient length, these phase perturbations can become important and manifest themselves in a variety of ways such as scintillation, image wander and image blurring. In astronomy, these effects are sometimes referred to collectively as s·eing. For large telescopes, seeing imposes a system independent resolution limit which has serious consequences for classical imaging techniques. For communication systems, the atmosphere imposes a limit on signal-to-noise ratios and causes other problems such as signal fading. The accuracy of metric information is also limited by these effects. Except for several techniques such as Michelson and Intensity (Hanbury - Brown and Twiss) Interferometry, little has been done historically to overcome these limitations. However, during the last few years, the development of techniques designed to overcome atmospheric turbulence effects has become an active research area. At present, a variety of techniques have been defined and in some cases reduced to practice. Still others are in the development and/or fabrication stage. In general, three different classes can be defined: post-detection processing, interferometry, and predection compensation. The first detects and records the degraded signal along with, in some cases, ancillary information and subjects these data to a variety of processing algorithms in order to extract the desired information. The second class are interferometric in nature in that higher order statistical moments of the optical field are the primary data of interest. The third class seeks to measure and correct the distortions in realtime using adaptive optical components yielding a distortion free optical field before detection. An important example of this type is the DARPA Compensated Imaging System which, in fact, combines predetection compensation with post-detection processing. As this new technology progressed, it became essential that quantitative information about the spectrum of turbulence effects be obtained so that system performance could be evaluated and specifications established.

This program, Turbulence Environment Characterization, was undertaken in response to this requirement. In broad terms, the objective was to experimentally investigate and characterize atmospheric turbulence and its effects on optical propagation. While the emphasis in this program was placed on visible wavelengths, the resulting information is also of interest to other portions of the electromagnetic spectrum provided the theoretically predicted wavelength scaling laws are valid. The program was implemented by deploying a variety of instrumentation at the DARPA Maui Optical Station (AMOS) atop Haleakala on the island of Maui, Hawaii. Instrumentation included devices to measure the statistics and vertical distribution of the underlying turbulent field as well as devices designed to directly measure propagation parameters. As a result, the data base obtained can be used to investigate the utility of theoretical models and to predict numerical values for important parameters which are not readily accessible to the available experimental techniques.

Specific tasks carried out under this program were as follows:

- Deployment, checkout, operation and maintenance of the experimental instruments.

- Data collection and reduction for a variety of purposes including the development of a data base relative to long-term statistics, instrument validation and performance measurements, comparative studies of results from several devices, and the investigation of specific effects.

- Analysis, evaluation and interpretation of the resulting data.

- Integration of the complete data base obtained with the objective of developing a consistent understanding of the AMOS turbulent environment.

1.2 REPORT ORGANIZATION

This report is the final technical report for the program. It is organized into two major sections.

Section 2.0 is a summary of the information, understanding and results obtained not only for this entire program but also for a previous program under which many of the measurement activities were started. Furthermore, results from other experiments carried out at AMOS but funded from other sources are included where appropriate. The objective of this summary is to give a brief but hopefully comprehensive and consistent picture of the

12

AMOS turbulent environment as it effects optical propagation.
Some discussion of and comparison with data from other sites is
also included. An attempt has been made to make this section
self-contained so that all important results and conclusions
appear in a single document without being obscured by excessive
details relating to experimental and analysis procedures. How-
ever, the section has been carefully referenced so that the in-
terested reader can find the more detailed discussions of the
instruments, experiments and analyses.

The details of the activities carried out in the final
reporting period of the contract are given in Section 3.0. The
significant accomplishments of the final reporting period are
given in Section 3.1. The results and conclusions obtained during
this period are summarized in Section 3.2. Section 3.3 discusses
the experimental operations and instrumentation changes which have
occurred since the last report. The details of the data collected
and analyses carried out are given in the final Section 3.4. In-
cluded are discussions of microthermal and acoustic sounder data,
Seeing Monitor measurements, Star Sensor data, comparisons between
the various experimental results and processed RTAM data.

2.0 THE AMOS TURBULENT ENVIRONMENT - SUMMARY

2.1 GENERAL

The purpose of this section is to summarize the measurements carried out during this program and to present an integrated view of the AMOS turbulent environment and its effect on optical propagation. The data and information now available are extensive and are documented in a number of reports, not all of which were written as part of this effort. Therefore, it seems advisable to present a self-contained, albeit brief description of the most important results and understanding achieved by the rather diverse activities which have occurred during the past four years. While the main emphasis is on the results obtained during this contract, work carried out under a previous contract as well as that performed by several other experimental groups funded from other sources is also included.

Some of the results included here have been published in the open literature. These publications will be referenced at the appropriate places. In addition, a number of reports are available from RADC.(1-6)

1. M.G. Miller and P.F. Kellen, Turbulence Characterization and Control, Interim Technical Report, Contract F30602-75-C-0012 (Avco Everett Research Laboratory, Inc.), Rome Air Development Center Technical Report #RADC-TR-75-185 (July 1975).

2. M.G. Miller, P.L. Zieske and G.L. Dryden, Turbulence Characterization and Control, Final Technical Report, Contract F30602-75-C-0012 (Avco Everett Research Laboratory, Inc.), Rome Air Development Center Technical Report #RADC-TR-76-189 (June 1976).

3. M.G. Miller and P.L. Zieske, Turbulence Environment Characterization, Interim Technical Report, Contract F30602-76-C-0054 (Avco Everett Research Laboratory, Inc.), Rome Air Development Center Technical Report #RADC-TR-77-70 (March 1977).

4. M.G. Miller, P.L. Zieske, A.J. Sofia and R.J. Pepe, Turbulence Environment Characterization, Interim Technical Report, Contract F30602-76-C-0054 (Avco Everett Research Laboratory, Inc.), Rome Air Development Center Technical Report #RADC-TR-77-232 (July 1977).

5. M.G. Miller and P.L. Zieske, Turbulence Environment Characterization, Interim Technical Report, Contract F30602-76-C-0054 (Avco Everett Research Laboratory, Inc.), Rome Air Development Center Technical Report #RADC-TR-78-72 (April 1978).

6. D.P. Greenwood, D.O. Tarazano, D.A. Haugen, J.C. Kaimal, J. Newman, P.F. Kellen and M.G. Miller, AMOS Seeing Quality Measurements, Rome Air Development Center In-House Technical Report #RADC-TR-75-295 (January 1976).

The organization of this summary is as follows. Section 2.2 gives a physical description of AMOS, the various experimental systems implemented and the kinds of operations carried out. Numerical values for several important optical parameters are given in Section 2.3. A quasi-empirical average turbulent profile is presented in Section 2.4. Comparisons between profile derived and directly measured optical parameters and data from other sites and models are discussed in Section 2.5. The final section includes the most important, general conclusions drawn from this data base.

2.2   INSTRUMENTATION AND OPERATIONS

The ARPA Maui Optical Station (AMOS), Figure 1, is located atop Haleakala on Maui, Hawaii. This island, located at approximately 21° north latitude, is the second largest of the Hawaiian chain. The observatory is at an altitude of ∼ 3 km above mean sea level and is just below the summit. The area around the observatory is covered by dust, cinders, small rocks and boulders of volcanic origin with virtually no vegetation. The prevailing trade winds are from the northeast and blow across a large volcanic and erosion crater before they reach AMOS.

The observatory, Figure 2, includes four domes. The two largest house a 1.6 m aperture telescope and twin 1.2 m aperture telescopes on a single mount, respectively. All three are Cassegrain instruments. The 1.2 m telescopes are primarily used for photometric and radiometric observations at visible and LWIR wavelengths. The 1.6 m telescope is a high quality visible instrument which is scheduled to receive the DARPA sponsored Compensated Imaging System presently under development. The other domes house a laser beam director and the NOAA Star Sensor.

The experimental systems which have been deployed and used to obtain data include the following.

2.2.1   Differential Hartmann [1,7]

A small (18 cm aperture) telescope was equipped with an aperture mask containing two small holes and a film camera which recorded an out of focus image of a star. In response to uncorrelated wavefront tilt across the two apertures, the separation

7.   M.G. Miller and P.F. Kellen, Proceedings of the AAS/SAO/OSA/ SPIE Topical Meeting on Imaging in Astronomy, Cambridge, Mass. (1975), Paper WB-3.

16

Figure 1   AMOS and Other Facilities Atop Haleakala, Maui, Hawaii
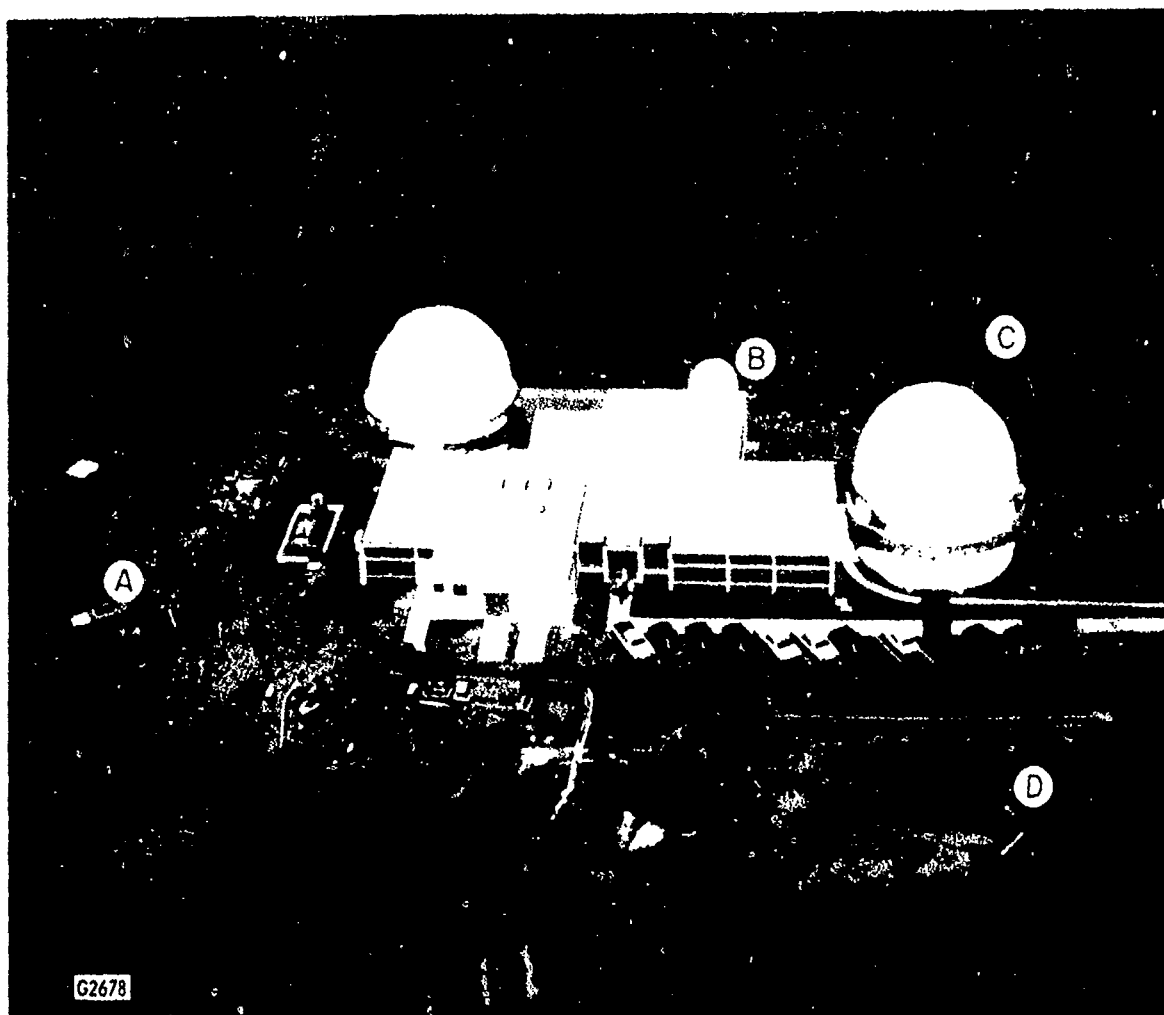
Figure 2   AMOS Site Locations of Atmospheric Instrumentation: A) Acoustic Sounder Antenna; B) 16 ft Dome Housing Star Sensor; C) North Meteorological Tower; D) South Meteorological Tower

of the two images varies with time. By collecting a series of short exposure images and carrying out a statistical analysis of image separation, estimates of the turbulence inspired image wander and correlation scale can be obtained.

2.2.2 Microthermal Probes [2,6,8]

Early in the measurements program, a number of microthermal probes were located in and around the observatory for a short period of time. Subsequently, they were replaced by triangular arrays of probes, ~ 20 m above the ground, located on two towers which are nominally upwind and downwind of the observatory. When taken in pairs, they provide a direct estimate of the temperature structure constant, [9] C_T^2. Simultaneous measurement of the required meteorological parameters (pressure and temperature) allow these data to be converted to the index of refraction structure constant, [9] C_n^2.

2.2.3 Routine Meteorological Instrumentation [2]

Each tower noted above is equipped with an anemometer to provide wind velocity data. One tower is also equipped with a temperature and dew point sensor and barometer. In addition to providing the meteorological information necessary for micro-thermal and acoustic sounder data processing, remote signals from these devices are periodically recorded with a data logger to provide a routine measurement of meteorological conditions.

2.2.4 Airborne Microthermal Probes [3,10]

During a relatively short period, a light aircraft instrumented with a microthermal probe was flown over the observatory. These operations and the subsequent data processing were carried out by personnel from the NOAA Environmental Research Laboratories.

8. D.P. Greenwood and D.B. Youmans, Rome Air Development Center Technical Report #RADC-TR-75-240 (December 1975).

9. R. Lawrence and J. Strohbehn, Proc. IEE 58, 1523 (1970).

10. R.S. Lawrence, G.R. Ochs and S.F. Clifford, J. Optc. Soc. Am. 60, 826 (1971).

2.2.5 Acoustic Sounder[2,6,11]

This device is a monostatic acoustic radar which measures the backscattered energy from small scale temperature variations. A simultaneous measurement of temperature and humidity allows this data to be reduced to estimates of the structure constant, C_n^2. The operational range of the acoustic sounder is, in principle, 30 to 300 m. In practice, the results are often dominated by noise at ranges in excess of 150 m.

2.2.6 Star Sensor[2,5,12]

The Star Sensor is essentially a scanning, spatially filtered photometer mounted on a 36 cm telescope. By analyzing the spatial frequency content of stellar scintillation patterns, estimates of the index of refraction structure constant, C_n^2, can be obtained. A direct measure of the aperture-averaged-log-amplitude variance[9] is also available from the measurements. Because scintillation is most strongly coupled to high altitude turbulence, the range of operation for this device is above 1 km. The reduced data corresponds to turbulence levels associated with several layers of varying widths. In addition to this spatial averaging, temporal averaging is also present because of the time necessary to scan the entire frequency range of interest. Two versions of this device have been used at AMOS.

2.2.7 Small Aperture Photometer[2,3]

One of the 1.2 m telescopes was instrumented with a photometer and aperture stop (36 cm effective entrance aperture) and used to make measurements of the scintillation log-amplitude variance. This system provided independent data for direct comparison with the Star Sensor.

2.2.8 Seeing Monitor[2,13]

This device is a scanning spatial-frequency photometer which is used to analyze the frequency content of stellar images as observed through a large telescope. As such, it yields a direct measure of the Modulation Transfer Function (modulus of the Optical Transfer Function) with an equivalent exposure time of

11. F.F. Hall in, *Temperature and Wind Structure Studies by Acoustic Echo Sounding*, ed. by V.E. Derr, U.S. Government Printing Office 0322-0011 (1972).

12. G.R. Ochs, Ting-i Wang, R.S Lawrence and S.F. Clifford, App. Opt. <u>15</u>, 2504 (1976).

13. C.R. Giuliano, et al., *Space Object Imaging*, Final Report, Contract F30602-74-C-0237 (Hughes Research Laboratory), Rome Air Development Center Technical Report #RADC-TR-76-54 (1976).

1 msec. Internal analog electronics are used to estimate the spatial frequency at which the MTF drops to one-half its initial value. This signal is processed with an on-line computer which calculates the mean and variance subject to programmable conditions. The resulting average value is then fit to a theoretical model to provide an estimate of the Mutual Coherence Function correlation scale,[14] r_o. The Seeing Monitor has been used on the 1.6 m telescope and one of the 1.2 m telescopes.

2.2.9 Speckle Interferometer[15]

A Speckle Interferometer is essentially a high quality, high resolution, short exposure camera (film or video) mounted at the image plane of a large telescope. Multiple short exposure images are Fourier transformed yielding a high spatial resolution data base which can be used to statistically characterize a variety of effects. The technique was originally conceived as a means of overcoming the degrading effects of atmospheric seeing on high resolution imaging. However, if simple objects (unresolved stars or binary systems) are observed, detailed information about the atmospheric propagation path can be obtained. Data has been collected with this device on both the 1.6 m and one of the 1.2 m telescopes.

2.2.10 Realtime Atmospheric Measurement System (RTAM)[16]

This device is a shearing interferometer based instrument which processes the signal in realtime and provides as output the optical transfer function (modulus and phase) in two orthonal directions. As such, its data is equivalent to that obtained with the Speckle Interferometer. Analog processing electronics[4] were built in order to provide data processing equivalent to the Seeing Monitor.

2.2.11 Operations

A number of different types of experimental operations and data collection activities have been carried out during this program. A significant amount of time has been spent in the obviously necessary step of preparing and evaluating the performance of the various instruments.

---

14. D.L. Fried, J. Opt. Soc. Am. 56, 1372 (1966). Related results are given in R.E. Hufnagel and N.R. Stanley, J. Opt. Soc. Am. 54, 52 (1964).

15. A.M. Schneiderman and D.P. Karo, Opt. Eng. 16, 72 (1977). The Speckle Interferometer work was funded by other sources.

16. A.J. MacGovern, Real Time Atmospheric Monitor, Final Report, Contract F30602-74-C-0147 (Itek Corporation), Rome Air Development Center Report #RADC-TR-78-80 (April 1978).

Early in the program, an intensive measurements period was carried out using ground level microthermal probes, the acoustic sounder and the differential Hartmann sensor. The major objective of these tests was to investigate the possible presence of locally inspired turbulence due to the existence and operation of the observatory. Although strong turbulence was consistenly observed within the 1.2 m telescope dome, no such obvious effects were found elsewhere in the observatory; naturally occurring atmosphere turbulence was found to dominate all other measurements.

Once the Star Sensor and Seeing Monitor became available, a more routine operational mode was developed. This involved scheduling data collection on a regular basis and maintaining near identical procedures. While the desire was to obtain data on a regular basis, this was not always possible due to schedule conflicts and necessary instrument maintenance. Hence, the data and results obtained tend to be concentrated in relatively short periods (several weeks to several months) separated by somewhat longer periods (months) in which little or no data were obtained.

From time to time, concentrated measurement activities were carried out. These operations typically dealt with specific objectives such as the detailed characterization of the angular behavior of r_o or comparative studies of the various data.

The data upon which the results and conclusions of the next sections are based are generally characterized by the following conditions and parameters.

Because of the detailed nature of the data obtained with the Speckle Interferometer, virtually all information relative to the validation of theoretical predictions has been derived from this instrument. However, because of the extensive amount of data generated in a short period of time, this instrument is not as convenient for the study of the long term statistics of atmospheric seeing as are others. The Speckle Interferometer was deployed on two occasions for periods of approximately two weeks.

Data suitable for the long term characterization of atmospheric seeing was obtained with the Seeing Monitor. The half-frequency output was averaged in realtime using a PDP-8 computer. Averaging periods were typically 10 min in length corresponding to a 1350 member ensemble. Over six hundred sample averages taken on over fifty nights have been collected to date. On several occasions, shorter averaging periods were used.

Because of the availability of speckle data and limited RTAM sensitivity, the RTAM was exercised on only a single occasion for a period of approximately one week. The objective of these operations was to obtain an independent and simultaneous measurement of r_0 for comparison with the Seeing Monitor.

The microthermal probes, acoustic sounder and Star Sensor yield information on the strength of turbulence as a function of altitude. Star Sensor data was obtained on fifty occasions. Ground level microthermal and acoustic sounder data is not as extensive due to a variety of reasons including routine maintenance, data processing requirements and instrument malfunctions and failures. Airborne microthermal data was collected on only four occasions over a one week period.

The primary objective of the small aperture photometer was to provide independent data for comparison with the total log-amplitude scintillation results obtained with the Star Sensor. After several short but concentrated data collection periods which yielded the data necessary to fulfill this objective, operations with this system were discontinued. After the Seeing Monitor became available, data collection activities with the Hartmann sensor were also discontinued.

2.3 OPTICAL PARAMETERS

The empirically derived MTF[17] agrees quite reasonably with models[18] based on a Kolmogorov spectrum of turbulence and the Rytov approximation. This means that this fundamental characterization of an imaging system can be adequately modeled from knowledge of the optical system and a single atmospheric parameter (r_0). At low spatial frequencies, the fall-off of the MTF is clearly proportional to the (5/3) power of spatial frequency as opposed to a Gaussian.[19] The short-term statistics of the Phase Transfer Function (PTF) are consistent with models which predict that the PTF at high spatial frequencies is a zero mean, uniformly (modulo-2π) distributed random variable.[20] This information was essential for validating the models used to reduce the data from other instruments.

17. D.P. Karo and A.M. Schneiderman, J. Opt. Soc. Am. 66, 1252 (1976).

18. D. Korff, J. Opt. Soc. Am. 63, 971 (1973).

19. D.P. Karo and A.M. Schneiderman, J. Opt. Soc. Am. 67, 1583 (1977).

20. D. Korff, G.L. Dryden and M.G. Miller, Opt. Comm. 5, 187 (1972).

The cumulative probability distribution function for the correlation scale, r_0, at 5000 Å is given in Figure 3. The straight line represents a Gaussian distribution with the empirical mean and variance. As can be seen, the data is consisent with Gaussian statistics. Over data collection runs of two to four hours in length, a variety of behavior has been observed including near constant conditions, large fluctuations (factor of two) and trends towards both improving and degrading conditions.[3,4,21] Data taken with short averaging times indicates the existence, on occasion, of probable nonisotropy, temporal nonstationarity and intermittency on time scales of seconds to minutes.[22]

A study of the wavelength scaling of r_0 indicates a $(\lambda)^{6/5}$ dependence as predicted by theory.[23] Studies of angular behavior do not confirm the $(\cos \theta)^{3/5}$ dependence predicted by theory.[22] A possible cause for this may be the existence of a "boundary layer" around the mountain which leads to a model with both an angular dependent and independent term in the integrated turbulence. The data is more consistent with such a model, but only modestly so.

Cumulative probability distributions for the log-amplitude variance averaged over a 36 cm aperture are given in Figures 4 and 5.[3] The former is for data collected on a single evening whereas the latter is for a period of approximately fifty nights. The straight lines are Gaussian distributions with the empirical means and variances. As can be seen, the single-night data are consistent with Gaussian statistics, whereas the multi-night data are not.

The entire set (20 points) of reduced angle-of-arrival (Hartmann) data are displayed in Figure 6.[1,7] The three symbols used indicate different locations of the instrument, whereas the bars represent the $\pm$ one sigma value of the reduced results. The values plotted are the rms image wander appropriate to a 6 cm aperture and the associated value of r_0. While the individual ensembles of data used to determine a single value of image wander display Gaussian statistics, insufficient data exist to reach any conclusion regarding the long-term statistics of this parameter.

21. M.G. Miller and P.L. Zieske, J. Opt. Soc. Am. 67, 1680 (1977).

22. Section 3 of this report.

23. A.M. Schneiderman and D.P. Karo, J. Opt. Soc. Am. 68, 480 (1978).
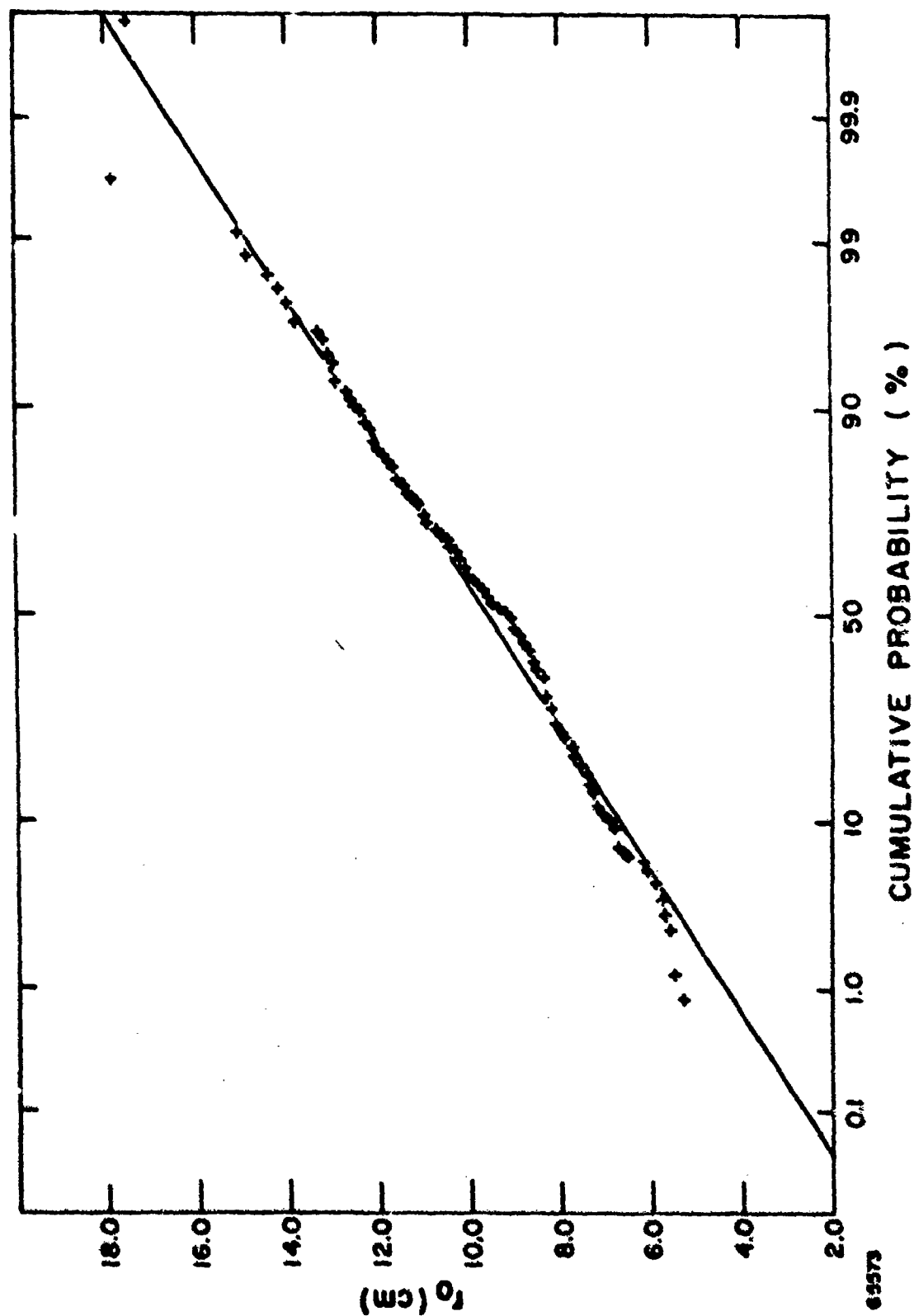
Figure 3   Atmospheric Correlation Scale: Cumulative Probability.
The straight line is for Gaussian statistics with the
empirical mean and variance.

25
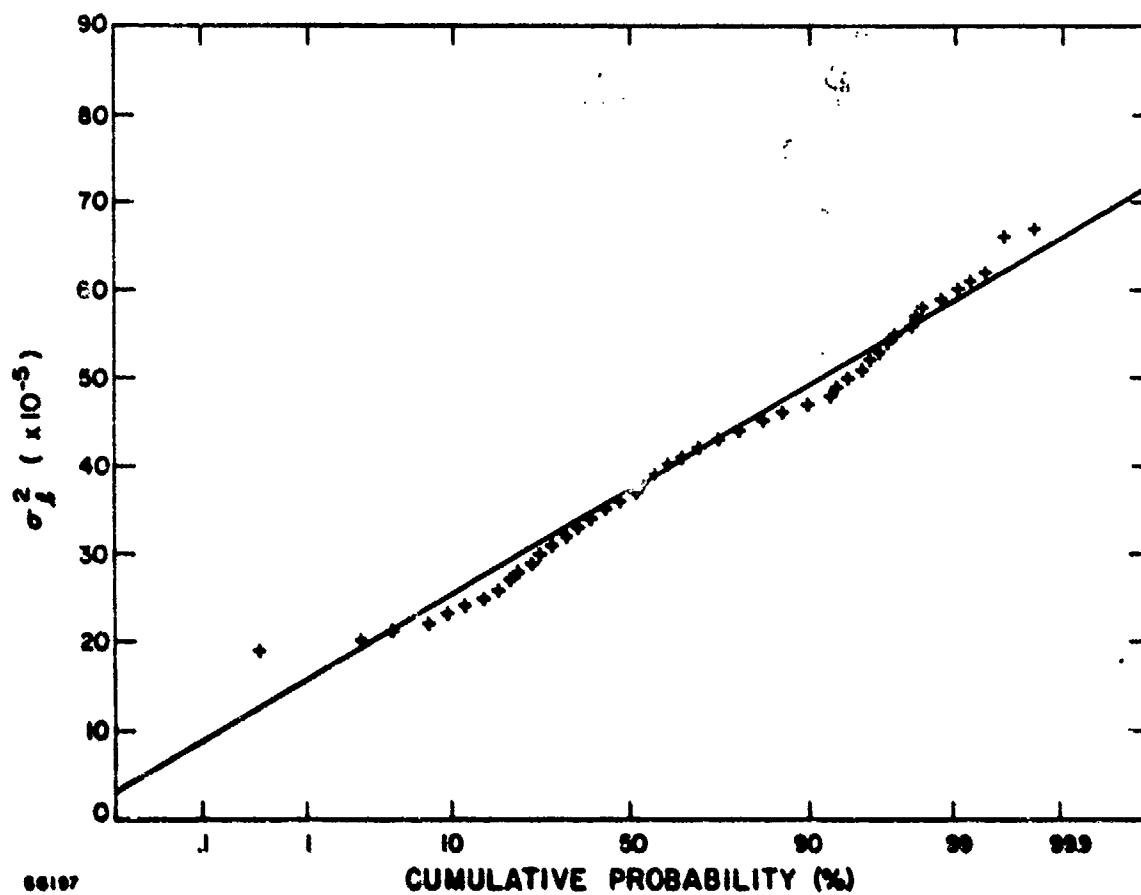
Figure 4   Aperture Averaged Scintillation: Cumulative Probability for One Night. The straight line is for Gaussian statistics with the empirical mean and variance.
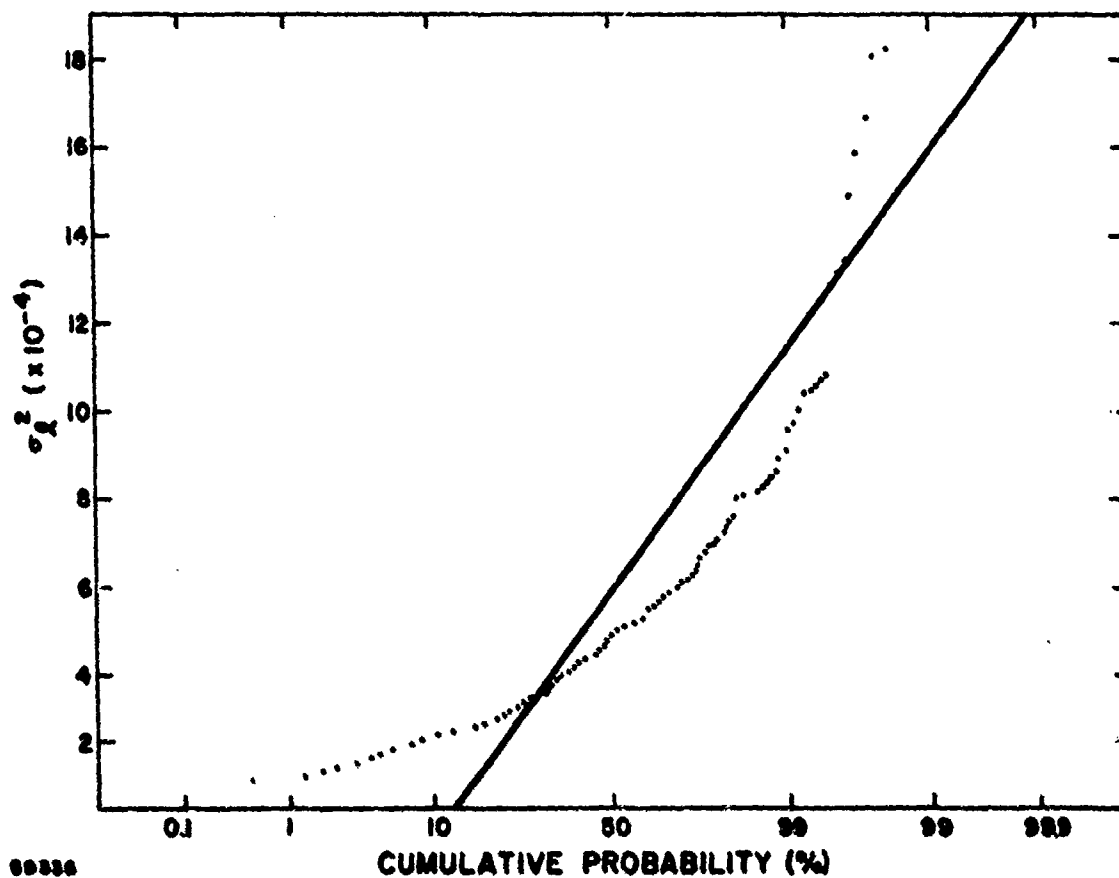
Figure 5   Aperture Averaged Scintillation: Cumulative Probability.
Each point is the average value for a single night. The
straight line is for Gaussian statistics with the
empirical mean and variance.
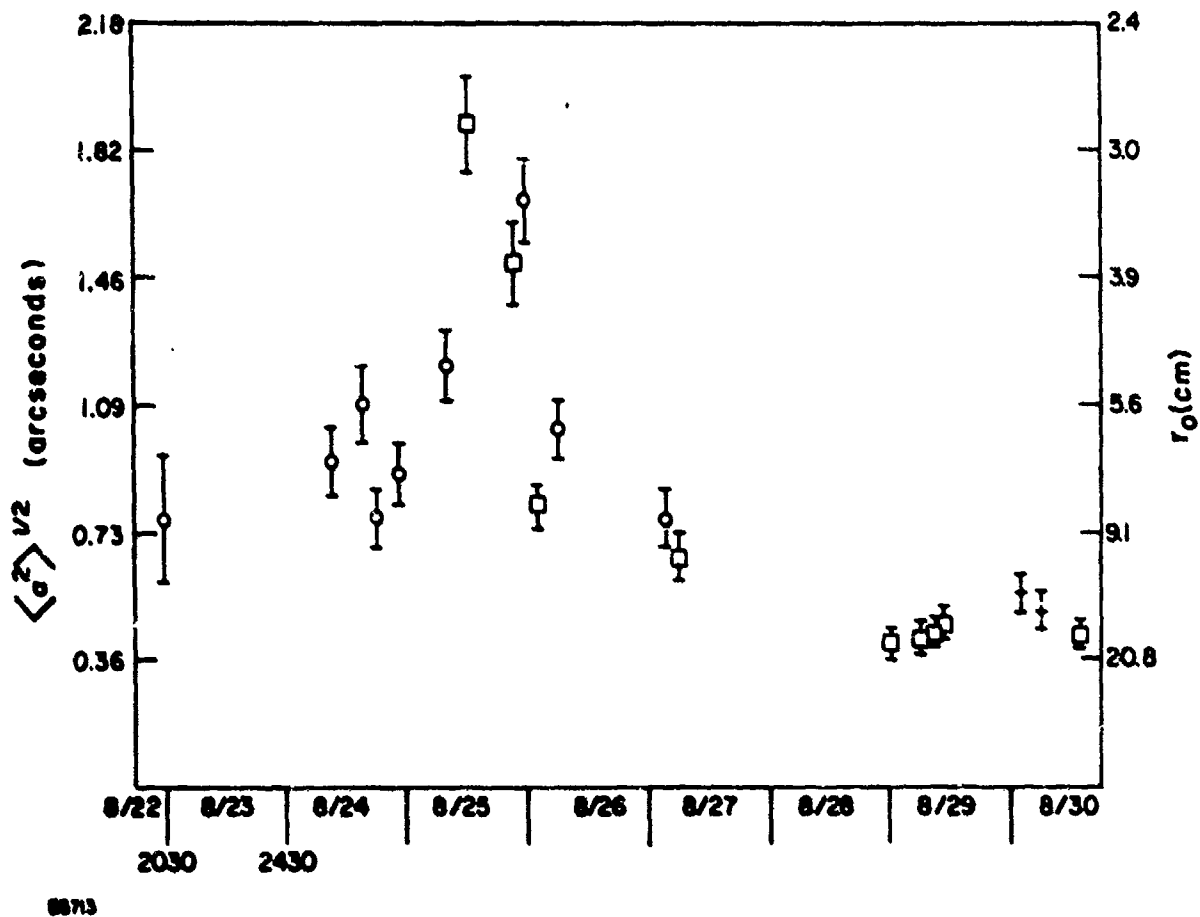
Figure 6   Angle-of-Arrival Data. The three different symbols
            represent results from three different locations.

A limited study[24] of nonisoplanacity effects indicates that such effects become important for objects larger than (2-4) arcsec. In addition, there appear to be significant differences between the detailed structure of the empirical result and the theoretical prediction;[25] however, this may be due to the turbulence profiles assumed in the theory.

The numerical values measured for these four direct optical parameters are summarized in Table 1. Included are mean value and range of each data set.

2.4 AVERAGE TURBULENT PROFILE

The ground level (18.5 m) microthermal sensors have yielded[22] values of C_n^2 in the range from 4×10^{-16} m-2/3 to 39×10^{-15} m-2/3 with a mean value of $\sim 8.4 \times 10^{-15}$ m-2/3. The very limited airborne data[3] fluctuates over approximately an order of magnitude in the altitude range from 100 m to 1000 m above the site. The median value for this range is of order 10^{-16} m-2/3.

The acoustic sounder typically indicates a rather rapid fall-off of C_n^2 with altitude. The data clearly decreases faster than the $h^{-2/3}$ with dependence which is often associated with the boundary layer at night under stable conditions. An analysis of a limited data[6] set taken early in the program indicates an average slope of (-1.4). However, more recently the fall-off has been observed to be more rapid. An average[22] of all data is $\sim h^{-2}$.

The Star Sensor yields values of C_n^2 associated with four (Model I) or seven (Model II) layers of varying widths at altitudes above 1 km (above the site). The data[22] from the two devices are consistent and indicates that two characteristic regimes are present. In the altitude range from ~ 1 km to 7 km, the fall-off with altitude is quite rapid. The central points of the data in this range can be successfully fit with an h^{-3} slope. In contrast, the data for altitudes from 7 km to 20 km show a more gentle slope of $\sim h^{-1/2}$.

Based on these data and the optical parameters of Table 1, the average AMOS turbulent profile of Figure 7 has been developed. [22] The absolute level of the profile has been fixed by the average ground level microthermal value and the best fit h^{-3} and $h^{-1/2}$ slopes of the Star Sensor

24. A.M. Schneiderman and D.P Karo, J. Opt. Soc. Am. 68, 338 (1978).

25. D. Korff, G. Dryden and R. Leavitt, J. Opt. Soc. Am. 65, 1321 (1975).

TABLE 1

OPTICAL PARAMETERS

Parameter	Mean Value	Range
Mutual Coherence Function Correlation scale: r_o (cm)	9.8	3.6-17.8
Log-Amplitude Variance (36 cm aperture)	5.8×10^{-4}	$(1.6-28) \times 10^{-4}$
Angle-of-Arrival Variance (6 cm aperture (arcseconds)	0.9	(0.4-1.9)
Isoplanatic Angle	$\geq$ 2 arcseconds	
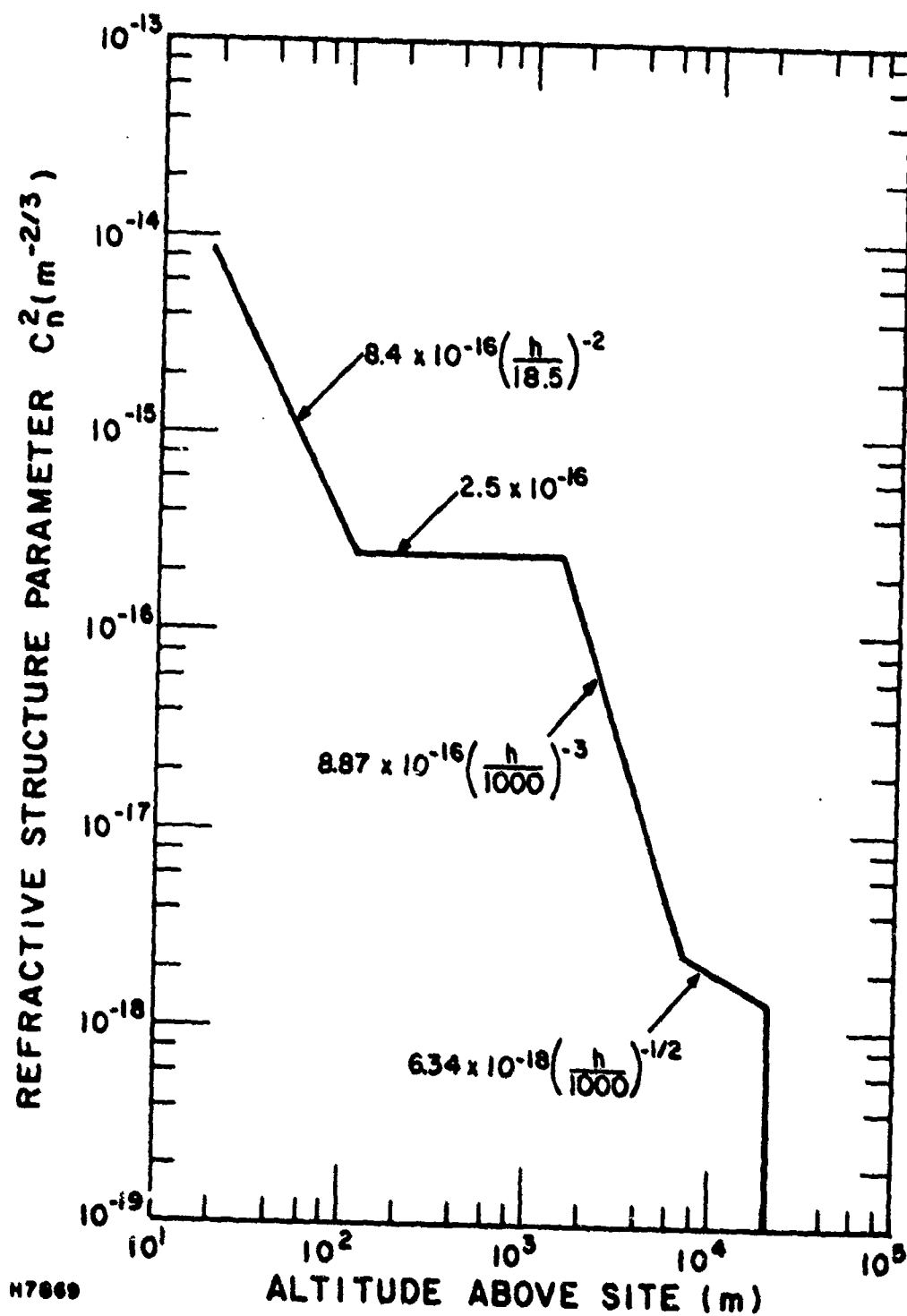
Figure 7   The Average AMOS Turbulent Profile. This profile is
based on microthermal, acoustic sounder and Star
Sensor data.

data in the range (1-7) km and (7-20) km, respectively. The characteristic acoustic sounder h^{-2} slope was adopted for the (20-100) m range although the numerical value of the coefficient was adjusted to fit the microthermal data. Because of the limited amount and scatter in the data for the range from 100 m to 1000 m, it is not possible to model this region in detail. Therefore, a constant value, consistent with the lower and higher altitude results, as well as the limited airborne data was assigned to this region. Although the very high altitude data (above 7 km) can also be successfully fit with an exponential, this introduces an additional free parameter (scale height) which must be fit to the five average data points existing in this range. In addition, an exponential model yields incomplete gamma functions when several interesting integral properties of the profile are evaluated. The $h^{-1/2}$ slope yields closed expressions. However, without a high altitude cut-off, several of these integrals will not converge. This cut-off was established by requiring the model to have the same amount of integrated turbulence as the data above 7 km.

Sufficient data on high altitude (> 1 km) turbulence also exist to investigate statistical behavior. The probability distribution function[22] for normalized values of C_n^2 determined with the Model I Star Sensor is given in Figure 8. As can be seen, the data are consistent with the straight line which represents a Gaussian distribution with the empricial mean and variance.

2.5 DATA COMPARISONS

Independent and simultaneous measurements of the aperture averaged log-amplitude variance were carried out on a number of occasions using the Star Sensor and small aperture photometer. The same stars were used as objects and identical averaging times were employed. Therefore, except for the central obscuration of the Star Sensor telescope, these two measurements were completely equivalent. While an apparent dc bias between the two data sets was observed, the results obtained were very consistent ($\pm$ 10%) when care was taken to assure simultaneity.[3] Furthermore, the bias, which was typically 10% of the observed variances, was of the order of the noise in the Star Sensor signal as determined by independent noise evaluation tests.

Two different sets of comparative measurements of r_0 were obtained during this program. The first involved the Seeing Monitor mounted on the 1.6 m telescope and the Speckle Interferometer mounted on one of the 1.2 m telescopes in the other dome.[4] The results of these measurements did not show good
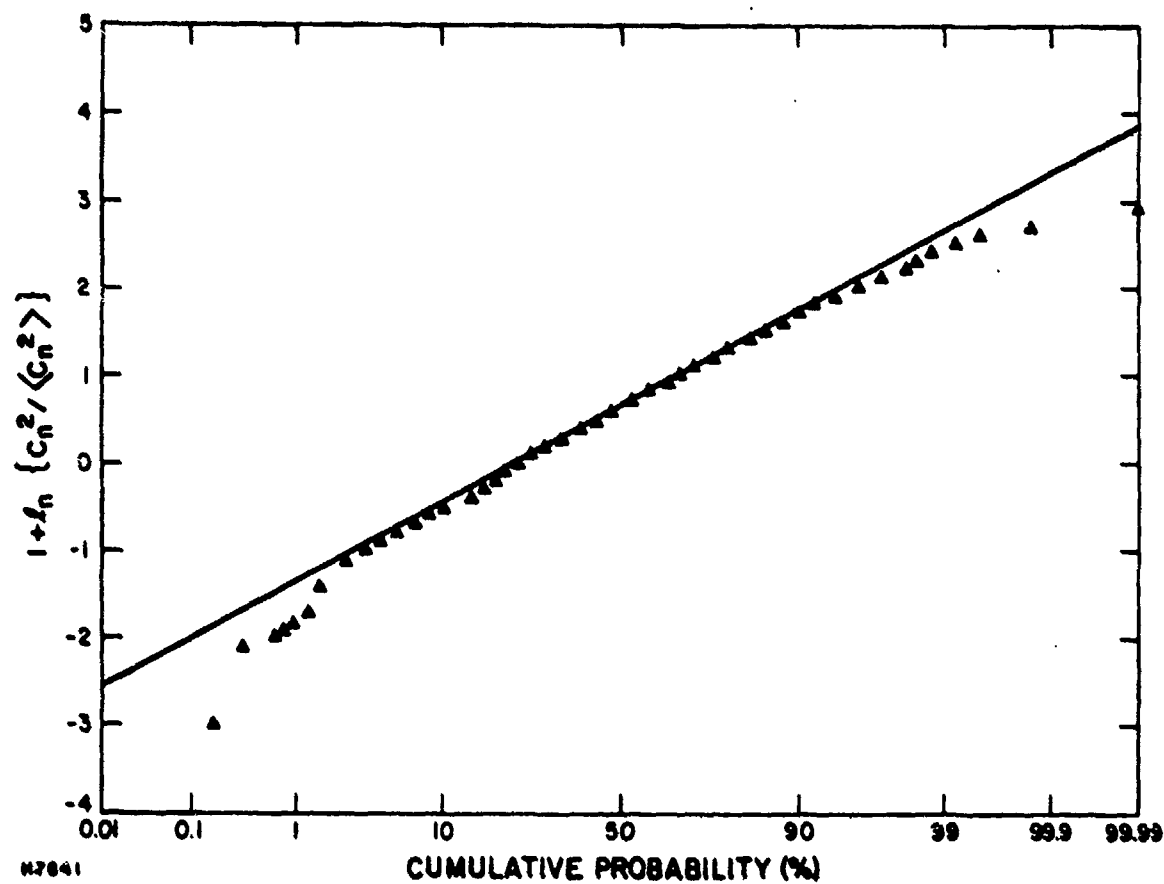
Figure 8   Normalized Upper Atmospheric Turbulence Levels. Data
is from Model I Star Sensor. The straight line is for
Gaussian statistics with the empirical mean and vari-
ance.

consistency. The causes for this may be the nonexistence of true simultaneity, different averaging times, spatial separation of the two instruments and the localized turbulence in the 1.2 m dome reported previously.[6]

Truly simultaneous measurements using identical propagation paths were obtained with the Seeing Monitor and RTAM.[22] For these experiments both instruments were mounted on the 1.6 m telescope and shared the same optical beam. Unfortunately, due to the lack of sensitivity of the RTAM, only a single 15 min data run taken against the brightest star available was of sufficient quality to be processed. During the period of observations, the SM measured a value for r_O of 11.5 cm with an accuracy of 10%. RTAM processing was complicated by high levels of noise, low system bandwidth and difficulty with establishing an absolute calibration of the output. The best estimate of r_O obtained was 12.6 cm with a probable accuracy of 15%. The two nominal values overlap within the estimated accuracies of the measurements and hence demonstrate consistency, at least for the small data sample available.

Because some of the instrumentation yields information relative to the profile of turbulence while other devices provide a direct estimate of optical parameters, it is possible to carry out direct comparisons of these two types of data. Three integral properties of the average profile discussed in Section 2.4 and three associated optical parameters are given in Table 2. The optical parameters are defined by:

$$r_O = [0.42 \ (2\pi/\lambda)^2 \int C_n^2(h)dh]^{-3/5} \tag{1}$$

$$\sigma_1^2(pt) = 0.56 \ (2\pi/\lambda)^{7/6} \int C_n^2(h)h^{5/6} \ dh \tag{2}$$

$$\Theta_c = [0.42 \ (2\pi/\lambda)^2 \int C_n^2(h)h^{5/3} \ dh]^{-3/5} \tag{3}$$

where λ is wavelength (5000 Å). $\sigma_1^2(pt)$ is the log-amplitude variance associated with propagation from a point source (star) to a point detector on the ground.[9] The aperture averaged log-amplitude variance for a 36 cm aperture is derived from this value by multiplying by the aperture averaging factor of 0.019 derived from theory.[26] The parameter Θ_c is physically equal

---

26. H. Yura, Aerospace Corporation Technical Report #TR-0077 (2756)-1 (1976).

34

TABLE 2

AVERAGE PROFILE - INTEGRAL PROPERTIES

$\int C_n^2$ (h) dh: $\qquad$ $6.9 \times 10^{-13} \ m^{1/3}$

$\qquad$ r_o $\qquad\qquad\qquad$ 10 cm

$\int C_n^2$ (h) $h^{5/6}$ dh: $\qquad$ $2.8 \times 10^{-10} \ m^{7/6}$

$\qquad$ σ_1^2 (pt) $\qquad\qquad\quad$ 0.030

$\qquad$ σ_1^2 (36 cm) $\qquad\quad$ 5.7×10^{-4}

$\int C_n^2$ (h) $h^{5/3}$ dh: $\qquad$ $3.1 \times 10^{-7} \ m^2$

$\qquad$ θ_c $\qquad\qquad\qquad$ 8.5 arcsec

35

to the ratio of the correlation scale, r_0, for propagation from a point source on the ground to an observation plane above the atmosphere to the altitude of observation.[27] It is associated with nonisoplanatic effects and is related to the angular parameters defined by Shapiro[28] and Fried[29] by multiplicative factors of $(3.44)^{-3/5}$ and $(6.88)^{-3/5}$, respectively. Furthermore, nonisoplanatic effects in speckle interferometry[24,25] become important for angular separations of $\sim 0.5\ \Theta_c$. Comparison of the numerical values given in Tables 1 and 2 show that the average AMOS profile of Figure 7 agrees quite favorably with the average values of the direct optical measurements.

Similar comparisons for nightly averaged data and single point data have also been carried out on several occasions. The results for the log-amplitude variance are consistent.[3] In some cases, those for r_0 are not.[22] While the exact cause of the disagreement is not known, the probable causes include non-stationarity, incomplete and inadequate coverage with profile instrumentation and the use of somewhat different spatial and temporal propagation paths. More detail is provided in Section 3.

Some information can also be generated relative to the variations in the average profile of Figure 7. While sufficient data exists to assign statistics to the ground level and high altitude values of C_n^2, it seems more advisable to simply scale the entire profile of Figure 7 due to the lack of information in the important intermediate range of altitudes. Based on an analysis of all available information, the average profile should be scaled by factors of 5.1, 0.32 and 1.7 to determine a maximum value, minimum value and mean plus one standard deviation profile, respectively.[22] The resulting profiles yield values of r_0 and σ_1^2 (36 cm) which agree reasonably well with the direct measurements of Table 1 and Figures 3 and 5. It should be emphasized that these scaling factors are rather subjective and are mainly included to demonstrate that a consistent, quasi-empirical profile appropriate to AMOS can be defined.

A number of measurements of r_0 for near vertical propagation paths have been carried out at other sites. Results obtained with a coherent interferometer[30] at Mauna Kea (120 km

---

27. D.L. Fried, J. Opt. Soc. Am. 56, 1380 (1966).

28. J.H. Shapiro, J. Opt. Soc. Am. 65, 65 (1975).

29. D.L. Fried, The Optical Sciences Company Report #TR-249 (March 1977).

30. J.C. Dainty and R.J. Scadden, Mon. Not. R. Astr. Soc. 170, 519 (1975).

southeast of AMOS) yielded an average value of 12.7 cm with a range from 4.1 cm to 18.5 cm. Knife edge data taken at the U.S. Naval Observatory at Flagstaff, Arizona and at Kitt Peak National Observatory yields[31] a median value of 6.7 cm. Analysis of star trail data taken in New Mexico has yielded[32] a nighttime average value of $\sim$ 8 cm. These results suggest that, on the average, AMOS has better seeing than the sites in the southwestern U.S. but is inferior to Mauna Kea; however, because the data base is limited, this conclusion is speculative.

Scintillation data has been collected for a considerable period of time at a number of different sites. Average properties of this data base are given in Ref. 33. Results are given in terms of the variance to mean value ratio of the integrated irradiance as seen by a 10 cm aperture. This parameter was found to be an approximate log-Gaussian random variable with a median value of 0.06 and a standard deviation of log 2.1. Scaling our results to a 10 cm aperture yields a median value of 0.04 and a standard deviation of log 2. Hence, the AMOS data is quite consistent with results taken at other sites; however, as noted in the previous section, the long term statistics of the AMOS data are non-Gaussian.

This same data base has been used by Hufnagel[33] to generate a statistical model for C_n^2 appropriate to altitudes above 3 km. A comparison of the Star Sensor data with the best fit average Hufnagel wind correlated model is given in Figure 9. The best fit value of the average upper atmospheric wind speed (w) is very close to the average value of 27 m/s given in the model. However, except for this and the fact that the change in slope of the data occurs at approximately the same altitude as the tropopause bump, the data and model bear little similarity. It should be noted that some caution should be exercised in comparing these two results due to the coarse altitude resolution of the data.

31. D.L. Fried and G.E. Mevers, App. Opt. 13, 2620 (1974); ibid., 14, 2567 (1975); ibid., 16, 549 (1977).

32. D.L. Walters, J. Opt. Soc. Am. 67, 1377A (1977); ibid., 68, 1368A (1978).

33. R.E. Hufnagel, CSA Topical Meeting on Optical Propagation Through Turbulence, Boulder, Colorado (1974), paper WA-1.
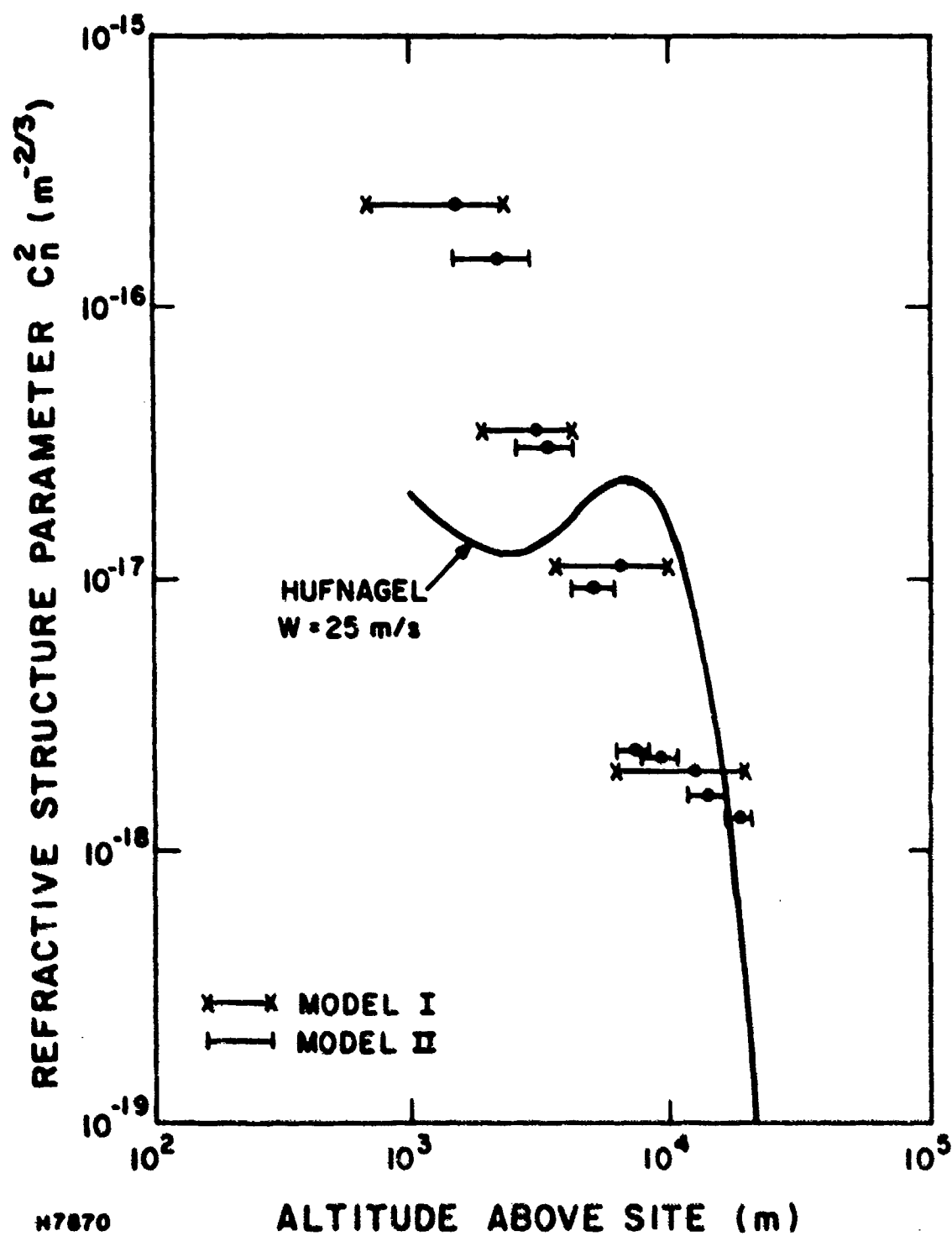
Figure 9   High Altitude AMOS Data. The solid line is the best
fit of the data to the average Hufnagel wind corre-
lated model.

38

Hufnagel also defines a random variable, $r(h,t)$ (h = altitude; t = time), which controls the statistics of C_n^2. This parameter is equivalent to the quantity plotted in Figure 8 and is assumed to be a Gaussian random variable with zero mean and a variance of two. The data has a mean of 0.66 and a variance of 0.76. The non-zero mean is probably due to the finite and non-zero threshold of the Star Sensor. The variance of $r(h,t)$ assumes, of course, point averaging in time and space. The covariance function of $r(h,t)$ has two characteristic time scales (5 and 80 min) and height scales (100 and 2000 m). The instrument bases its estimate of C_n^2 on data collected over a 20 min time period and averaged over altitude ranges considerably wider than 100 m. Therefore, the empirical statistics displayed in Figure 8 are considered to be consistent with the model.

Several other measurements of isoplanatic effects have been recently carried out. Speckle Interferometric data has been obtained at AMOS by another group.[34] Their results appear to be similar to those reported here. An experiment[35] using adaptive optics techniques leads to a similar conclusion.

Data relative to upper atmospheric turbulence levels have been collected on a number of occasions at other locations. Recently, balloon borne microthermal data collected at three sites in Europe have been reported.[36] A Model II Star Sensor has also been deployed at sites in New Mexico.[37] While it is difficult to compare the Star Sensor data with the microthermal data due to differences in altitude resolution, it appears that the AMOS data has a stronger dependence on altitude, being higher at lower altitudes and lower at higher altitudes than the other two results. Only the balloon data shows the possible existence of a significant enhancement of turbulence in the vicinity of the tropopause.

---

34. P. Nisenson and R.V. Stachnik, J. Opt. Soc. Am. 68, 169 (1978).

35. S. Pollaine, Lawrence Berkley Lab., private communication.

36. R. Barletti et al., J. Opt. Soc. Am. 66, 1380 (1976).

37. C. Hogge, Air Force Weapons Lab., private communication.

2.6 CONCLUSIONS

The preceeding sections briefly describe the instrumentation, operations and some of the results obtained during a program which was implemented with the objective of quantifying and characterizing atmospheric turbulence and its effects on optical propagation at the AMOS observatory. A considerable data base relative to several important propagation parameters has been accumulated. Furthermore, sufficient data relative to the strength of turbulence as a function of altitude exists to develop an AMOS turbulent profile which is consistent with all available information.

The comparison of AMOS data with results obtained at other sites generally supports the conclusion that this site has excellent seeing characteristics. Differences seen can be associated with normal variations and do not point to any major inconsistencies.

In summary, sufficient information and data have been obtained to confirm theory and provide a characterization of the average AMOS turbulent environment. The resulting model should be of value in carrying out system level performance analysis for optical systems which must operate in this environment. However, due to a variety of behavior including probable non-isotropy, temporal nonstationarity and intermittency, the application of existing theory and "average" properties to the detailed operation of such systems should be approached with care and some caution.

3.0 PROGRAM ACTIVITIES: 1 OCT. 1977 - 30 SEPT. 1978

3.1 PROGRAM STATUS AND ACCOMPLISHMENTS

As of the date of this report, the status of the instrumention is as follows:

- Data collection with the meteorological instrumentation, Seeing Monitor, Star Sensor, microthermal probes and acoustic sounder has been reduced to a routine operation.

- Several upgrades to the VR3700B tape recorder have been accomplished to provide more flexibility in operation.

- The PDP-8 mean and variance II and Mark V acoustic sounder data processing software is now operational.

Significant accomplishments during this reporting period include:

- Processing of five acoustic sounder data runs.

- The definition of data transmittal procedures.

- The generation of routine operational documentation.

- The analysis of five nights of simultaneous data using the microthermal probes, acoustic sounder, Seeing Monitor and Star Sensor II.

- Collection and Processing of Star Sensor II noise characterization data.

- Reprocessing of the Model I Star Sensor Data to correct an inaccurate assumption in the original algorithm.

- Investigation of the angular dependence and short-term statistics of seeing.

- Processing of RTAM data.

- Development of an average AMOS turbulent profile.

41

3.2 RESULTS AND CONCLUSIONS

The most important results and conclusions obtained during this period of the contract are as follows:

- The analysis of five nights of simultaneous data taken during the summer of 1977 yield a total integrated turbulence which is consistent with that measured by the Seeing Monitor. This consistency was established by normalizing the acoustic sounder data to the ground level microthermal data.

- The noise characteristics of the Model II star Sensor are slightly better than those of Model I. An empirical model developed from this data is probably of sufficient accuracy to replace the currently used calibration procedure.

- The reprocessed, four level, Model I star Sensor data are in substantial agreement with the Model II data. Furthermore, these new values result in somewhat better consistency in the comparative study of simultaneous data taken in the fall of 1975. However, there is still substantial dispersion in the results.

- The angular dependence of seeing does not support the theoretical scaling law. However, it can be modeled with a physically motivated two layer model with moderate success.

- Seeing Monitor data collected with short averaging times shows probable non-isotropy, non-stationarity and intermittency on time scales in the range from seconds to minutes.

- The processing of a single, very limited RTAM data set yields results which are consistent with the simultaneous data obtained with the Seeing Monitor.

- The average AMOS turbulence profile developed primarily from the results of the profiling instrumentation is quite consistent with the average properties of the directly measured optical parameters.

3.3 OPERATIONS AND INSTRUMENTATION

3.3.1 Operations Summary

During this period of the contract, activities at AMOS emphasized establishing a routine operational status for all atmospheric instrumentation. The systems for which such status has been achieved include: (1) microthermal probes, (2) meteorological sensors, (3) acoustic sounder, (4) Star Sensor and (5) Seeing Monitor. The upgrades and other development work required to achieve this objective are detailed in Section 3.3.2.

A special series of optical alignment tests were carried out on the Star Sensor. This was done because an alignment problem was found in the duplicate Star Sensor which has been deployed at White Sands. The results of these tests were negative and verified that the device was operating as designed.

Special emphasis was given to the acoustic sounder due to the sensitive calibration technique required. Seven data runs were reduced in detail (20 levels) using the Mk 5.0 reduction software. The AMOS SNDR PLOT program was used to plot the final results to allow a convenient graphical display. To complete the checkout of the acoustic sounder system, a special test and compatibility tape was generated and sent to RADC.

A variety of nondata collection and processing activities were also carried on during this period. These included modifications to the two processing sytems (PDP-8 and NOVA 2/10), calibration and checkout of the dew point sensor, expansion of the VR3700B tape recording capability, installation of voltage control and noise suppression devices and the writing of operational documentation. The latter was necessary to establish procedures so that data collection can be carried out by the normal operations crew with a minimum of additional manpower.

As a final validation, a special data run was conducted using all sensors. This operation verified that all systems fulfilled the requirements for routine data collection.

During the summer of 1978, a special test series was implemented. The objectives of these activities were three-fold. The first was to obtain data relating to the angular dependence and short term statistics of seeing using the Seeing Monitor. Star Sensor (Model II) noise characterization data were also collected. Finally, existing RTAM data, which was taken simultaneously with Seeing Monitor data, were processed. The results of these tests are discussed in Sections .4.2, 3.4.3.4 and 3.4.5, respectively.

3.3.2 Instrumentation Status

During this final period of the contract several upgrades
and system improvements were made to the atmospheric sensor sys-
tems. Systems affected were: (1) microthermal probes, (2) PDP-8I
computer, (3) routine meteorological sensors, (4) Star Sensor,
(5) dew point sensor, (6) acoustic sounder, and (7) VR3700B Instru-
mentation tape recorder. These sensor upgrades and modifications
are discussed below along with other relevant, peripheral systems
improvements.

3.3.2.1 Microthermal Probe Systems

The microthermal probe systems in use at the AMOS site have
evolved over the contract period from fine-wire types to a more
rugged fat-wire tape. Although these fat-wire probes proved to
be more durable in regard to sensing element lifetime, they were
still plagued by weather related corrosion induced failures. A
weather resistant version was fabricated at RADC and subsequently
installed at AMOS. The new probe replaces two nonweather proof
Amphenol type connectors with a single weather proof connector,
thereby eliminating the electrical failures resulting from con-
nector pin corrosion. All switching functions were incorporated
into a single switch. Heavier gasketing was installed under the
cover plates used to seal the electronics compartment. Perhaps
the single most significant improvement was the incorporation of
a plug-in sensor head. This interchangeability allows the quick
replacement of a broken sensing wire by exchanging sensor heads,
thereby eliminating the need to replace the complete probe. The
new systems have operated reliably throughout most of 1978.

3.3.2.2 PDP-8I Computer Software

The PDP-8I computing system was upgraded last year by the
replacement of its teletype peripheral with a new unit. The con-
trolling software that had been previously used to process micro-
thermal probe, routine met and Seeing Monitor data, computed only
the means, variances and covariances for the 15 channels involved.
New software called the M&V II program has now been installed and
provides the added capability of some data reduction. Microthermal
data are averaged for a programable number of samples and then used
to calculate C_n2 values for all three probe combinations on each
tower. In addition, the wind speed and direction are averaged for
both towers and tabulated with their respective variances. The
mean temperature, dew point and barometric pressure are also tab-
ulated. Seeing Monitor data are averaged and the data then used
to compute values of r_o for the two Seeing Monitor channels.

44

3.3.2.3 Routine Meteorological Sensors

The data from the routine met sensors had been previously collected only when the PDP-8I data processing system was operating. To provide continuous data collection a Keithly System 70 Datalogger was installed. This system provides an hourly printed record of wind speed (2), wind direction (2), temperature, dew point and pressure. These data are collected 24 hours a day, seven days a week. The operation is independent of all other systems.

3.3.2.4 Star Sensor

In July 1977 the original Star Sensor system was replaced by a newer version. Model II operated well until the fall of 1978. At that time a 15-volt power supply failed and during its repair another problem dealing with the X and XF circuits was identified and also repaired. Furthermore, an internal inspection of the electro-optical mechanical package revealed excessive galling and wear on the cardioid scanning cam. Subsequently the following repairs were made: (1) a new cam was fabricated from thicker stock, (2) the cam follower spring was replaced with one of smaller spring constant, and (3) the cam follower roller bearing was replaced. These repairs combined with an electronic alignment and wavelength calibration have returned the Star Sensor System to operational status.

3.3.2.5 EG&G Model 110S-M Dew Point Sensor

Dew point data from the 110S-M has been extensively compared with psychrometrically determined data since August 1978. By use of the sling psychrometer and National Weather Service Tables for the 711 mb level, dew points were determined coincidentally with those from the Model 110S-M set. A system bias was detected and removed. During the course of the investigation several things were observed: (1) during conditions of low humidity, the servo circuit that controls the mirror cooling module in the 110S-M system tracks the dew point better with the Auto Balance Circuit disabled provided a manual balance is performed once a week, and (3) the system tracks the dew point more reliably if the condensate thickness is increased. Adjusting for this behavior has yielded a system which is now operating accurately and continuously.

3.3.2.6 Acoustic Sounder

This system has been operating reliably since a new X-Y multiplier chip was installed in the system's control unit. Early in 1978 the acoustic sounder's anechoic cuff was replaced with a newer improved version. This new cuff is hexagonal in shape, is ~6 ft high and uses a special sound absorbing material as a liner. A special canvas cover and fasteners were designed and fabricated locally to provide weather protection to the antenna assembly.

3.3.2.7 VR3700B Instrumentation Recorder Reconditioning and Upgrade

The Bell & Howell VR3700B recorder was given depot level maintenance by Bell & Howell factory personnel in the spring of 1978. Mechanical alignment, tracking, tape tension and extensive electronic adjustments and calibrations were performed. The system now has 13 FM reproduce amplifiers and one direct reproduce amplifier. The recording configuration now consists of two wide band Group II, two wide-band Group I and four intermediate band FM record amplifiers. There is also one direct record amplifier.

3.3.2.8 NOVA 2/10 - Star Sensor Interface

Several changes have been made to this equipment since its original installation to improve the control and communication functions between the 2/10 computer and Star Sensor systems. The CPU was relocated to a higher position in the rack. Previously, it had been located below the high-speed tape reader making it inconvenient to read and set. Additional physical protection for the switch register was also obtained by moving it to a higher position in the rack. When originally installed the computer system had only a main power breaker-switch located in the panel above the CPU. To provide better communication and control several other functions were added. A switch was added to provide remote power switching to the Star Sensor telescope package located in the atmospherics dome. This allows remote control of the scanning motor from the computer panel. Next to this switch is located a 3 1/2 in. panel meter and four toggle switches. The switches allow the meter to read the four Star Sensor signals. These are the same signals normally available for display at the telescope package. Two spring-loaded centeroff, toggle switches were also installed to allow remote control of the telescopes declination and polar axes. These switches, when used in conjuction with the "I" switch panel meter allow for accurate correction of telescope tracking error, remotely. Finally a two-position toggle switch was installed as a program control switch, which when activated, causes the software to perform the additional tasks of averaging and formatting the normal ?DSP data.

3.3.2.9 Voltage Control and Noise Suppression

In order to minimize the effects of voltage fluctuations on sensitive equipment, certain line conditioning devices have been installed. These include a Sola saturable core type transformer and a General Radio servo controlled autotransformer. The systems requiring this conditioned line voltage are the System 70 Datalogger, PDP-8I CPU and the DEC AD01-AN A/D Converter.

46

Sensors installed on the north tower (microthermal probes, wind speed, wind direction, dew point and ambient temperatures) are exposed to EMI from a nearby television repeater station. To eliminate spurious signal levels a systematic check of each instrument was made and appropriate bypass capacitors and ferrite chokes installed.

3.3.2.10 Routine Operations Procedures Manuals

Operational Procedures Manuals for the following systems have been written: (1) AMOS Microthermal Probe Systems and PDP-8I Data Processor, (2) AMOS Routine Meteorological and Data-logger Systems, (3) AMOS Star Sensor and NOVA 2/10 Data System, (4) AMOS Acoustic Sounder System, and (5) AMOS Seeing Monitor System.

3.4 EXPERIMENTAL DATA AND ANALYSIS

3.4.1 Microthermal and Acoustic Sounder Data

Microthermal measurements have been made on a number of occasions since the inception of the AMOS Atmospherics Measurements Program. The purpose of these operations has varied from basic testing and calibration of other systems to extensive data collecting efforts involving the simultaneous operation of a number of different instruments. In particular, data collecting runs of several hours in length on each of a number of nights, concentrated within a period of several weeks or more, were carried out on three occasions. Data was also collected at other times and is available, but these three sets appear to be typical and are of major interest because other types of data (acoustic sounder, angle-of-arrival, Star Sensor and/or Seeing Monitor) were also collected simultaneously.

These three data sets are summarized in Table 3. The first (August 1974) was collected and processed by RADC personnel and is discussed in Ref. 6. The other two were collected as part of this program and are discussed in Refs. 3 and 5, respectively. They were obtained with the triad of probes located, nominally, at 18.5 m above local ground level. The first set was collected with a number of probes which were located at various places in and around the domes.

The mean values and standard deviations to mean ratios given in the table were calculated on the basis of ensembles in which the average value for a specific run was considered as a single point in the ensemble. The three set total was weighed according to the number of nights included in each data set. The ranges given are the minimum and maximum single point values measured by any given probe within each data set.

The large relative standard deviation to mean ratio for the three set total is a result of the approximate factor of 2.5 difference between the 1974 data and the 1975/1977 data. This difference in the data may be due to the measurement technique used in the earlier data. Except for a single pair of probes located at 4 m above the ground, the data results from the measurement of temperature variances. Consequently, it was necessary to use a value for the outer scale of turbulence to convert these data to values of C_n^2. This parameter was estimated from the single available pair of probes. In contrast, the latter data were obtained from two triads of probes taken in pairs (1 m separation); therefore, it was not necessary to associate a numerical value with the outer scale of turbulence. Furthermore, the 1974 data were taken with probes whose detailed design was somewhat different than the probes used since 1975. Consequently, it is quite possible that the factor of 2.5 is mostly due to experimental error and relative calibration. This factor also impacts

48

TABLE 3

MICROTHERMAL DATA: c_n^2

	Mean $\times 10^{-15} \, m^{-2/3}$	(SD/M)	Range $\times 10^{-15} \, m^{-2/3}$
August 1974	16.0	0.70	2.2-100
November/ December 1975	5.6	0.65	0.5-17
July/August/ September 1977	6.7	0.62	0.4-39
Total	8.4	0.90	0.4-100

the maximum value seen in the complete set. Coupled with the
fact that the second highest value observed was the maximum of
the 1977 data, it may be appropriate to ignore this very high
value (100) for the purposes of system level studies. Subject
to the above comments, the three set values given in the table
are thought to be fairly representative of turbulence conditions
near the ground at AMOS.

After a lengthly period of instrument maintenance, recon-
ditioning and modification, acoustic sounder data was obtained
on a number of occasions during July, August and September 1977.
These operations were carried out simultaneously with micro-
thermal, Star Sensor and Seeing Monitor data collection activ-
ities.[5] These combined data formed the basis for the
comparative study discussed in Section 3.4.4.3. Because of
the time required to process sounder data, five of these sets
were selected for detailed analysis.

These data runs were from two to three hours in length. An
averaging time of ten minutes was used in the processing, corre-
sponding to the basic cycle time of the PDP-8 system; therefore,
twelve to eighteen reduced profiles were obtained for each set.
Six reduced ten minute average profiles obtained on 21 July are
shown in Figures 10 through 15. In these plots, the vertical
axis is altitude above the ground in meters. The horizontal axis
is C_n^2 in units of m-2/3. The profiles extend from 30 to 300 m
with a 15 m increment. In each of these plots, two profiles are
shown. The one denoted by x's is the turbulent profile, whereas
the one denoted by squares is a noise profile. This latter re-
sult was obtained by collecting data with the transmitter turned
off prior to each mission; therefore, the noise levels obtained
are more appropriate to the start of the run.

The numerical values of C_n^2 given in Figures 10 through
15 and Table 4 should be treated as un-normalized. The reason
for this is that the calibration constant used in the data re-
duction was derived from data obtained with the original instru-
ment by AFCRL personnel at Jackass Flats, Nevada during October
1974.[6] Unfortunately, the numerous modifications of the sys-
tem which have occurred since 1974 probably make this procedure
unreliable. Hence, a normalization constant derived from micro-
thermal data must be applied to the acoustic sounder results.
This procedure is discussed in Section 3.4.4.3.

These profiles show the typical behavior of acoustic sound-
er data; i.e., a strong inverse dependence of turbulent strength
on altitude. Noise becomes important in the vicinity of 100-150
m. Above 200 m, noise dominates leading to an increase in appar-
ent turbulence with altitude. Although the data generally de-
creases with altitude, five of the profiles show an increase from
the second to third level. While such fluctuations (at various
levels) occurred throughout the data with some regularity, no
particular significance is attached to this behavior.
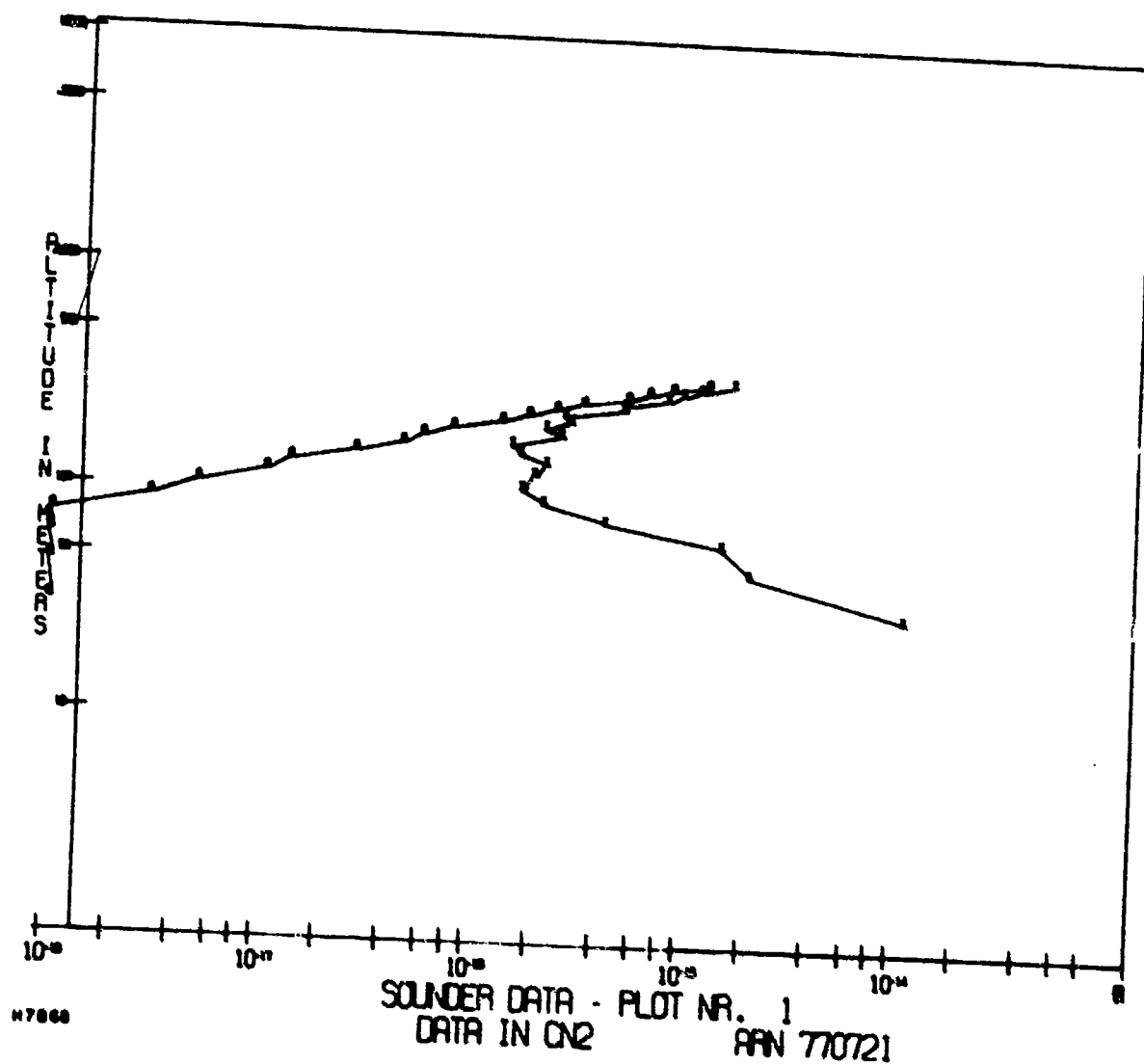
Figure 10   Un-Normalized Acoustic Sounder Data for 21 July 1977, Cycle #1, 10 Minute Averaging Time.   Turbulence data is indicated by x's whereas squares correspond to system noise.

Figure 11   Un-Normalized Acoustic Sounder Data for 21 July 1977,
Cycle #3, 10 Minute Averaging Time

Figure 12   Un-Normalized Acoustic Sounder Data for 21 July 1977, Cycle #5, 10 Minute Averaging Time

Figure 13   Un-Normalized Acoustic Sounder Data for 21 July 1977, Cycle #7, 10 Minute Averaging Time

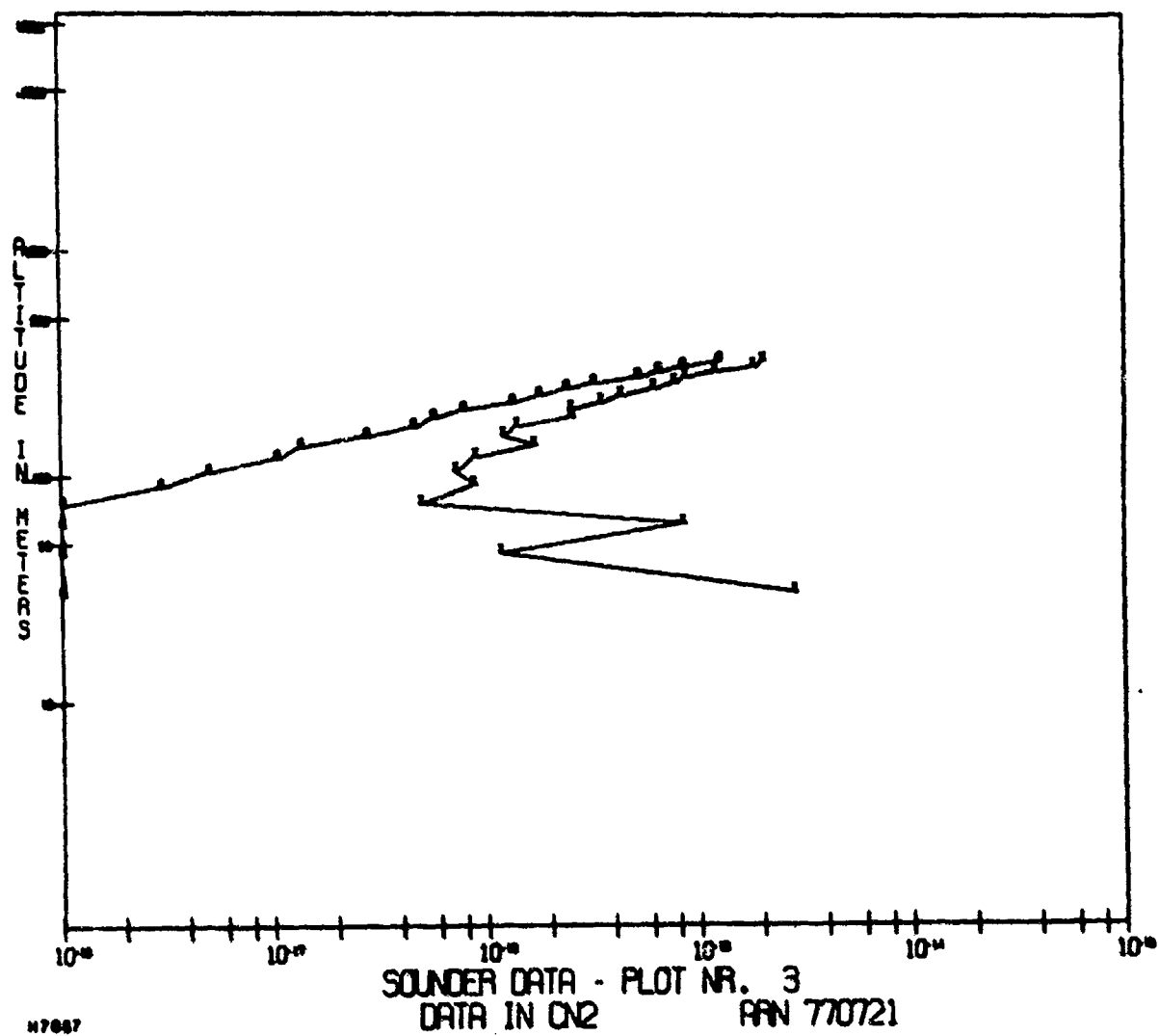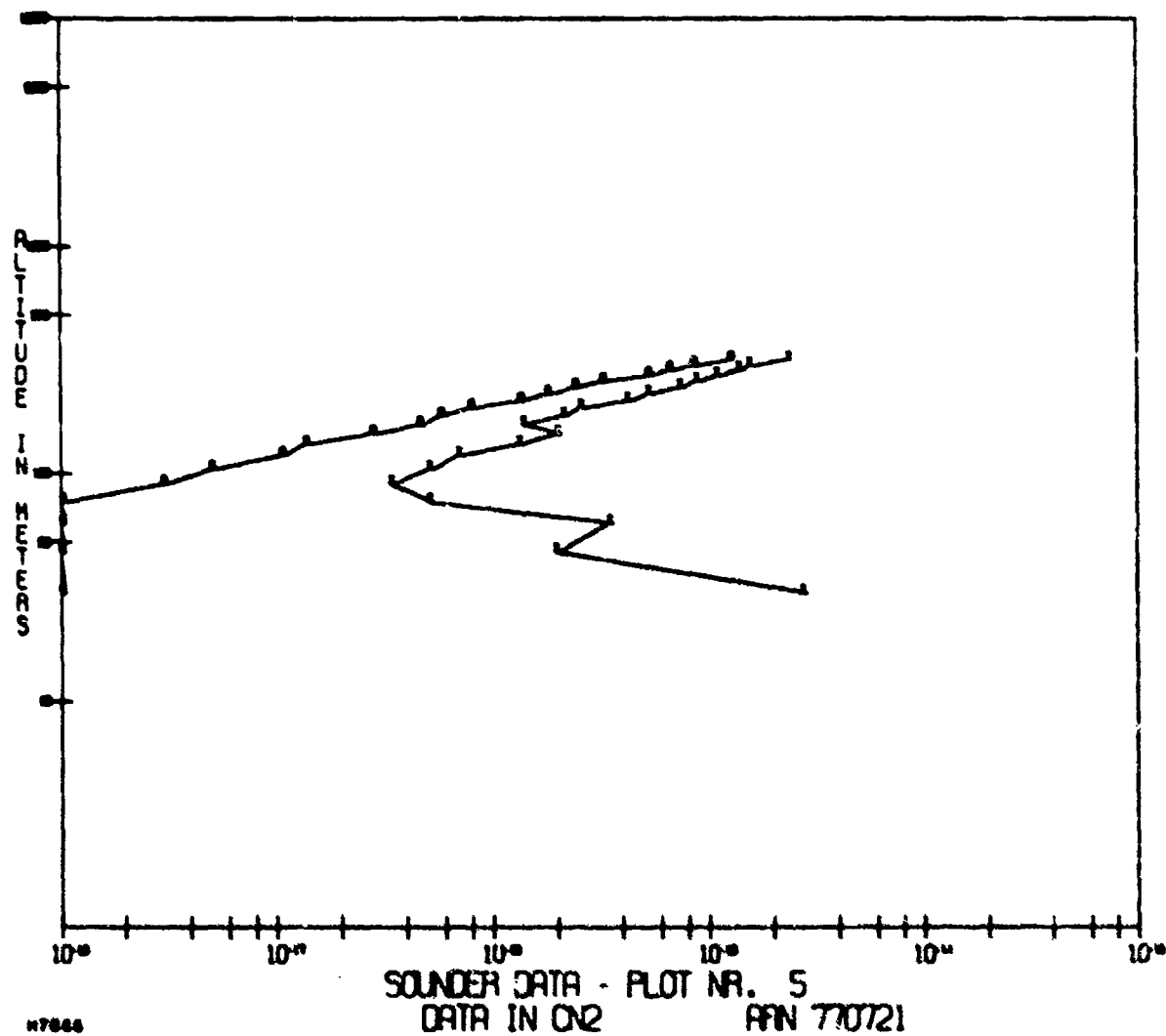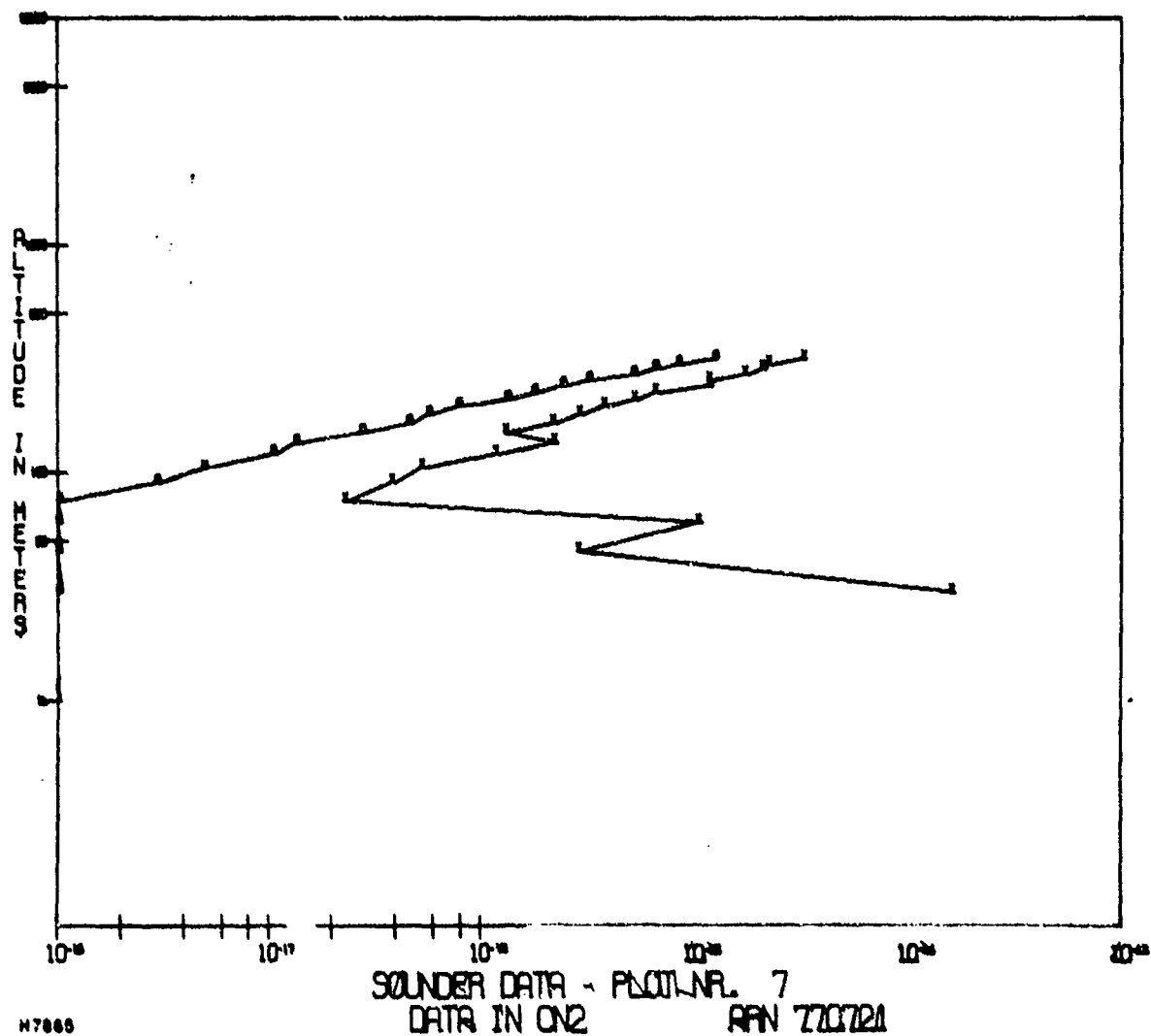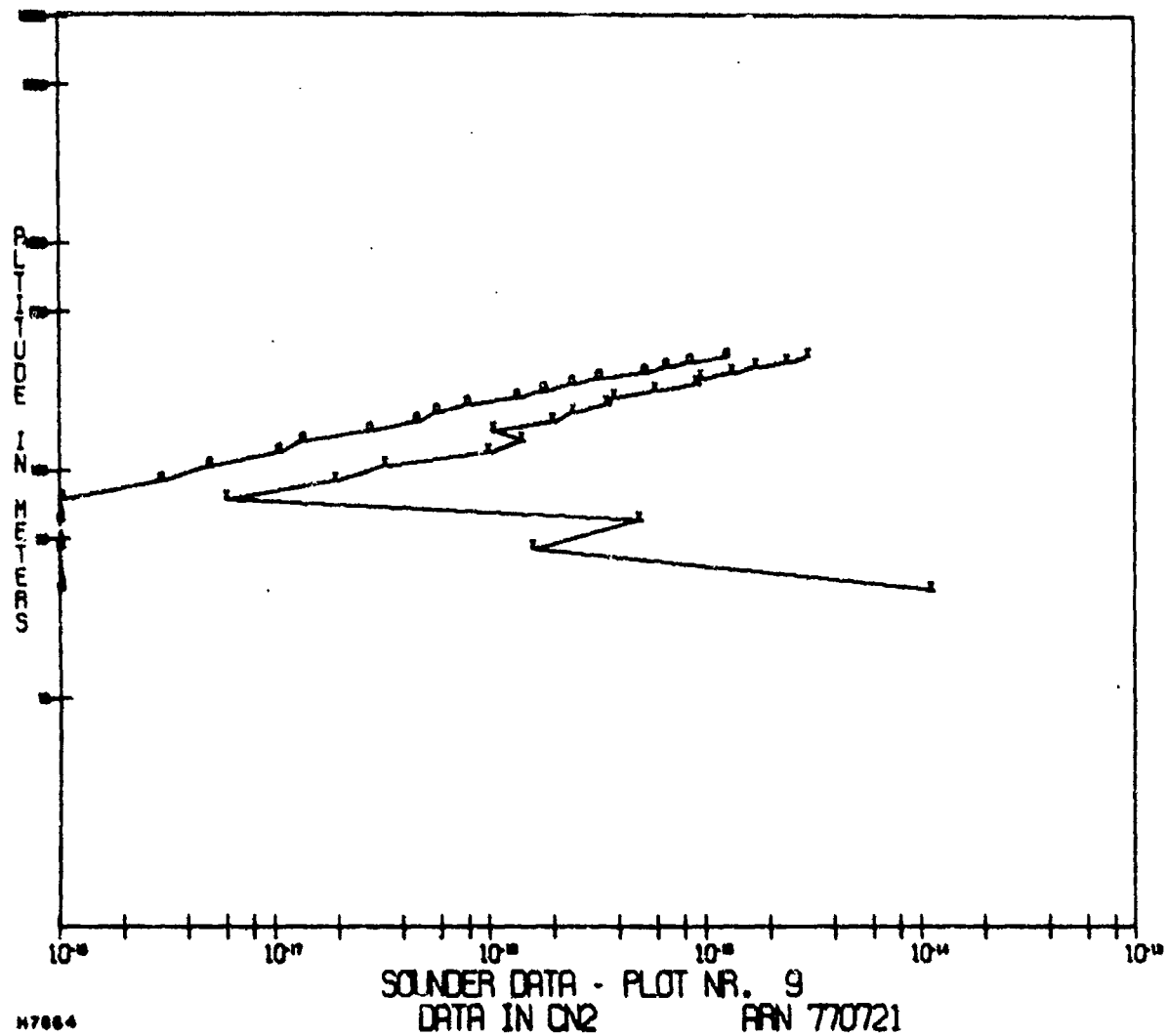Figure 14   Un-Normalized Acoustic Sounder Data for 21 July 1977,
Cycle #9, 10 Minute Averaging Time
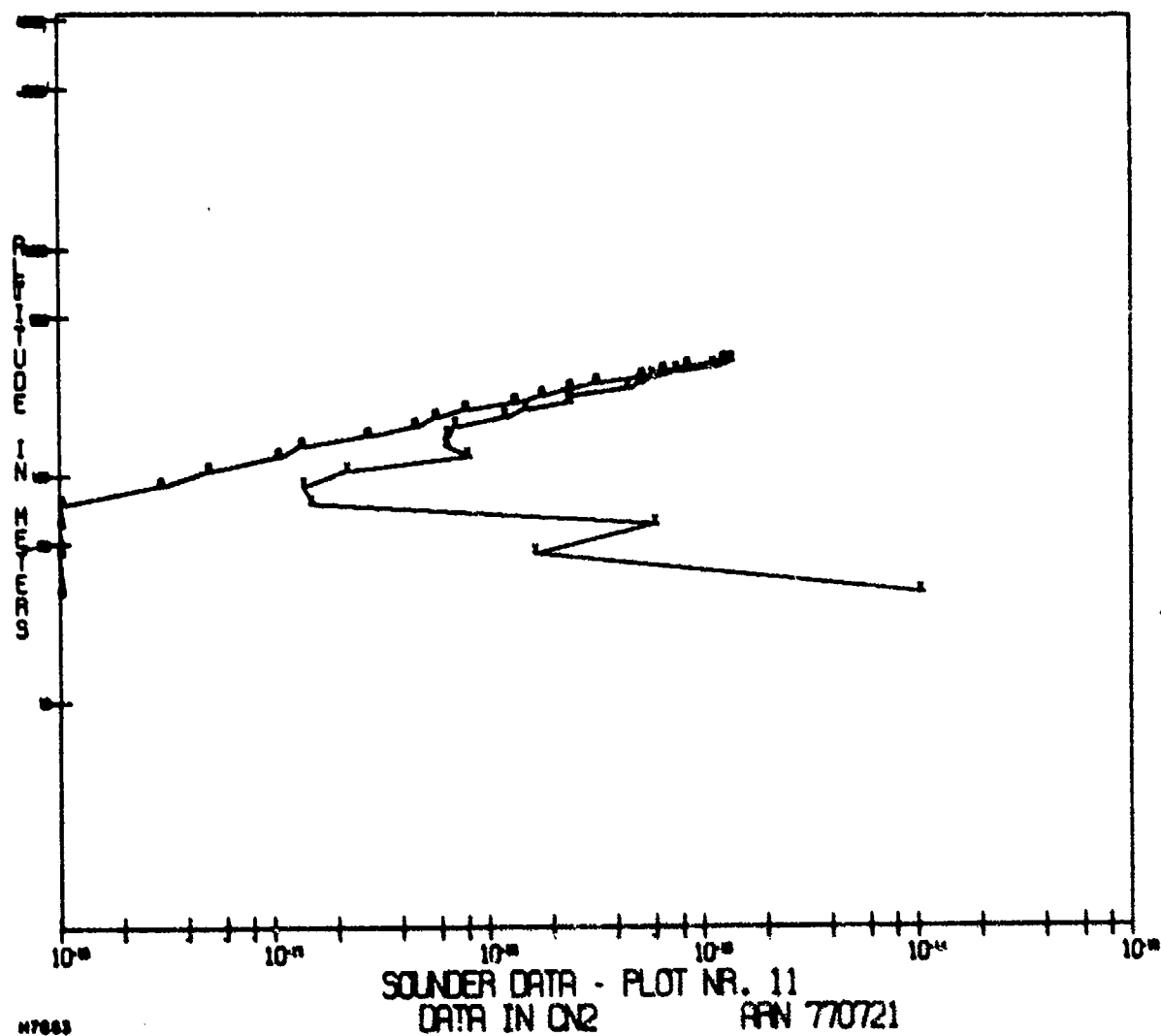
Figure 15   Un-Normalized Acoustic Sounder Data for 21 July 1977, Cycle #11, 10 Minute Averaging Time

TABLE 4

AVERAGE ACOUSTIC SOUNDER PROFILES (UN-NORMALIZED)

C_n^2 (x 10^{-15} m$^{-2/3}$)

Altitude (m)	21 July #1		21 July #2		22 July		26 July		2 August		3 August	
	Data	Noise	Data	Noise	Data	Noise	Data	Noise	Data	Noise	Data	Noise
30	11.9	0.001	10.8	-----	28.7	0.15	31.6	0.02	30.0	0.001	40.7	-----
45	0.35	0.005	0.30	-----	8.68	0.12	8.99	0.02	0.87	0.001	0.39	-----
60	0.75	0.013	0.65	-----	5.95	0.12	4.94	0.03	0.90	0.001	0.14	-----
75	0.095	0.004	0.068	0.001	4.03	0.15	2.58	0.05	0.53	0.005	0.003	0.001
90	0.099	.007	0.076	0.003	3.54	0.18	1.69	0.08	0.58	0.008	0.003	0.003
105	0.11	0.012	0.077	0.005	2.85	0.23	1.40	0.13	0.51	0.02	0.002	0.007
120	0.16	0.026	0.11	0.01	2.39	1.31	1.35	0.22	0.49	0.03		
135	0.23	0.043	0.17	0.013	2.24	0.38	1.49	0.50	0.49	0.05		
150	0.20	0.066	0.15	0.027	1.90	0.57	1.30	0.90	0.26	0.09		
165	0.22	0.11	0.16	0.046	1.60	0.59	1.52	1.35	0.23	0.16		
180	0.32	0.11	0.25	0.057	1.94	0.82						
195	0.36	0.15	0.21	0.078	2.00	1.03						
210	0.48	0.28	0.37	0.13	1.97	1.26						
225	0.38	0.33	0.47	0.18	1.78	1.60						
240	0.95	1.40	0.75	0.24	2.12	1.94						

The run averaged profiles for the five reduced data sets are given in Table 4. Only data up to that altitude at which noise starts to dominate are included. For 21 July, two independent reductions of the same raw data are shown. As can be seen, these two results differ by as much as 40%. The reason for this is that somewhat different sampling of the raw data occurred in the two reductions. Therefore, the differences should be taken as an indication of the statistical significance of the results and not suggestive of processing software problems. Graphical displays of these results are given in Section 3.4.4.3 where a comparison of the complete empirical profiles and directly measured optical parameters is discussed.

A final observation relative to the data is that the average slope with height is approximately (-2.4). A previous data set(6) had an average slope of (-1.4). Combining all available acoustic sounder data obtained from AMOS yields an average slope of approximately (-2). This is significantly stronger than the (-2/3) slope associated theoretically with a stable boundary layer at night. It is also stronger than the (-4/3) slope associated with convective unstable conditions during the day.

3.4.2 Seeing Monitor

3.4.2.1 General

Routine Seeing Monitor data was not collected during this period of the contract. The reason for this was the existence of a backlog of hardware upgrade and data analysis tasks which were of higher priority. Furthermore, an extensive data base relative to the correlation scale (r_o), taken with a 10 min averaging time, exist from previous work.[3,4,5] An assessment of this data indicated that additional routine data collection with only the Seeing Monitor would not add significantly to the characterization of atmospheric turbulence at AMOS. This conclusion should not be extended to all operations with this device as its output will continue to be important and valuable in support of missions such as classical photography and further studies of the detailed vertical structure of the atmosphere in conjunction with other instrumentation.

During July 1978 a special series of Seeing Monitor operations were carried out. These operations had two objectives: to investigate the angular dependence of atmospheric seeing and to obtain further information about short-term, non-stationarity effects. These experiments are discussed in detail in the next two sections.

3.4.2.2 Angular Dependence of Seeing

The conventional theory of propagation through turbulence defines[14] the correlation scale (for propagation from a star to the earth) as

$$r_o = [0.42 \ k^2 \int C_n{}^2 ds]^{-3/5} \tag{4}$$

where k is the wavenumber $(2\pi/\lambda; \lambda = \text{wavelength})$ and $C_n{}^2$ is the refractive index structure parameter. The integral, ds, is along the propagation path. The structure parameter is assumed to be a function of altitude only (h) and, thus, the correlation scale for zenith angle θ is given by

$$r_o(\theta) = [0.42 \ k^2 \int C_n{}^2(h) \ \frac{dh}{\cos \theta}]^{-3/5} = r_o(o) \ (\cos \theta)^{3/5} \tag{5}$$

where $r_o(o)$ is the value for zenith viewing. This result indicates a simple scaling with zenith and no dependence on azimuth. It is a direct result of assuming a model in which the turbulent structure is homogeneous and isotropic at a fixed altitude and varies slowly with altitude.

59

In order to experimentally investigate angular effects, the following procedure was developed. A data run was defined as a series of bright ($m \leq 4$) stars at various zenith angles in the range $70° > \theta_z \geq 0°$. A typical run included six to eight stars. The star closest to zenith was designated as a reference. All inputs to the PDP-8 (with mean and variance software) were eliminated except the two Seeing Monitor signals. This allowed 5,000 sample averages to be obtained in ~ 1 min followed by ~ 6 sec of printout. The Seeing Monitor was equipped with 600 Å spectral filters ($\lambda_0 \simeq 6200$ Å) in order to eliminate atmospheric dispersion at low elevation. Data was collected against the various stars in a cyclic, sequential fashion: 121314151617181, where the numerals 1 through 8 represent the stars in the series. Star 1 was the reference star. The repetitive return to the reference was done so that the effects of atmospheric non-stationarity could be assessed. In total, nineteen such data runs were carried out on seven nights during the period from 17 July 1978 to 11 August 1978. Typically, a single eight star run took ~ 30 min to complete. While the original intent was to include both zenith and azimuth angle runs, there were not a sufficient number of bright stars located appropriately to allow an isolation of these two variables; therefore, azimuth angle was ignored.

The first step in data processing was to convert the average output voltages of the SM to values of r_0 scaled to a wavelength of 0.5 μ using the standard reduction algorithm.[2] The resulting values were then scaled to zenith using Eq. (5). An example of one such run is shown in Table 5.

Because of the effects of temporal non-stationarity, it is difficult to assess the data by simply plotting the values of r_0 as a function of zenith angle; therefore, the results were processed as follows. The basic data cycle consists of an $[r_0(1);$ $r_0(2); r_0(3)]$ sequence where $r_0(1)$ and $r_0(3)$ correspond to the zenith scaled values of r_0 associated with the reference star and $r_0(2)$ is the zenith scaled value of r_0 associated with a star at a zenith angle different from the reference star. For this sequence, the following parameters were calculated.

$$\Delta = 2 \left[\frac{r_0(2)}{r_0(1) + r_0(3)} \right] \tag{6}$$

$$\varepsilon = 2 \frac{|r_0(1) - r_0(3)|}{[r_0(1) + r_0(3)]}$$

The parameter ε is a measure of temporal non-stationarity because it involves two measurements taken against a single star separated by no more than 3 min in time. If the atmosphere were

TABLE 5
ANGULAR DEPENDENCE OF SEEING
DATA SET 18 JULY 1978 - #1

| | | $r_0(\theta)$ (CM) | | $r_0(o)$ CM | |
STAR	ZENITH ANGLE	CH #1	CH #2	CH #1	CH #2
1	7	12.3	11.0	12.4	11.0
2	21	9.6	8.4	10.1	8.9
1	7	12.3	11.4	17.3	11.4
3	31	11.6	9.7	12.7	10.6
1	7	11.4	10.0	11.4	10.0
4	32	11.6	10.7	12.9	11.8
1	8	12.3	11.0	12.4	11.1
5	49	10.5	9.4	13.5	12.1
1	9	13.3	12.1	13.4	12.2
6	48	8.4	8.4	10.7	10.6
1	9	12.9	11.2	13.0	11.3
7	68	7.5	7.6	13.5	13.8
1	10	12.1	10.7	12.2	10.8
8	70	9.1	8.0	17.3	15.2
1	11	11.7	10.8	11.4	11.0

61

stationary, ε would be essentially zero except for noise and a very slight change in angle ($\lesssim 1°$). In contrast, Δ is sensitive to both non-stationarity and the breakdown of the theoretical angular scaling due to its dependence on stars at two different zenith angles. The validity of the theoretical model (Eq. (5)) can be judged by determining the statistics of Δ and ε.

While all nineteen data runs were processed in this fashion, seven were eliminated from further consideration because of temporal non-stationarity. This assessment was based on the run average value of ε. If this average exceeded 0.1, the run was eliminated. The reduced results for the remaining twelve runs are given in Figure 16 which is a plot of the parameter Δ as a function of zenith angle. Each open circle represents a single value of Δ. The mean value and standard deviation for the entire data set are 1.11 and 0.16, respectively. These values are indicated in the figure by the closed circle and vertical bar. The horizontal dashed lines represent the quantities $1 \pm <\varepsilon>$. The numerical value of $<\varepsilon>$ for the twelve data sets is 0.07.

The results shown in Figure 16 clearly indicate that the experimental data is not consistent with the theoretical zenith angle scaling law. Furthermore, the mean value and the higher frequency of large values of Δ for large zenith angles supports the conclusion that seeing does not degrade as rapidly with angle as predicted.

In view of the above conclusion, it is reasonable to try to develop a physical model which is consistent with the experimental results. Consideration of a number of individual runs indicated a significant amount of random dispersion of the data. This could be accounted for by a breakdown of the fundamental assumption of a homogeneous and isotropic turbulent field. Other previously reported data[2-5] also supports this thesis.

It is also possible to carry out a least squares fit of the data to an alternative function of angle provided there exists some physical rationale upon which to base such an analysis. One such possibility is suggested by the general topology of the site as well as by airborne microthermal data. The major portion of Maui (which is Haleakala) is roughly 50 (EW) by 40 (NS) km with a peak altitude of $\sim$ 3 km situated in an open ocean which extends for thousands of kilometers in the predominant northeast trade wind direction. Therefore, it is not unreasonable to argue that a region of relatively high turbulence may exist with an envelope which more or less follows the contour of the mountain. If this were the case, then viewing a star away from zenith would not add additional integrated turbulence associated with this region because optical path lengths would be roughly constant. However,

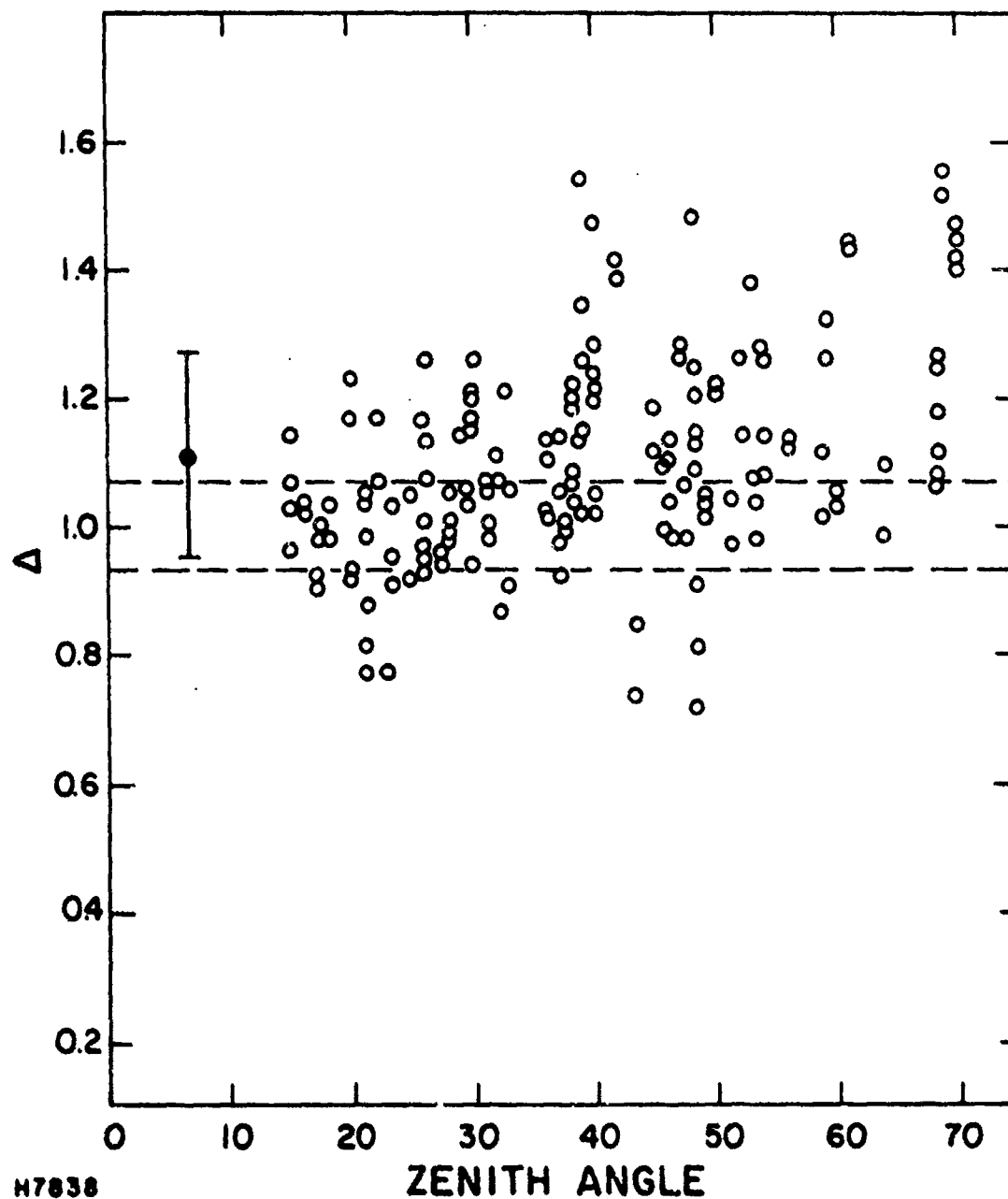Figure 16   Seeing Monitor Angular Data. Each data point is a
single measurement of Δ. The solid circle and bar
indicate the mean (1.11) and (+) one standard devi-
ation (0.16) of the data. The dashed lines represent
$1 \pm <\varepsilon>$, where $<\varepsilon> = 0.07$.

63

higher altitude turbulence would be uneffected by the existence of the island and, therefore, should follow the scaling of Eq. (5). This line of reasoning leads to the result that

$$
r_o \sim \left[\int_{low\ alt} c_n{}^2 (s)\, ds + \int_{high\ alt} c_n{}^2 (s)\ ds \right]^{-3/5} = \left[A + B/\cos\ \theta \right]^{-3/5}
$$

(8)

where A and B are independent of angle.

Several of the data runs have been fit with this model. The results are shown in Figures 17, 18 and 19. Also shown in the figures are fits to Eq. (5). While not entirely successful, it does appear that the data is fit somewhat better by Eq. (8).

The coefficients of fit (A and B of Eq. (8)) are given in Table 6. It is interesting to note that the best fit occurs for data set 21 July #3 which has the largest value of r_o and a (34-66)% split between "low" and "high" altitude turbulence whereas the poorest fit occurs for data set 18 July #1, which has the smallest value of r_o and a (66-34)% split between "low" and "high" altitude turbulence. This suggests that the breakdown of the assumption of a homogeneous and isotropic turbulent field should be associated with low altitude effects.

In summary, the measurements discussed here indicate that the theoretically predicted zenith angle scaling does not adequately describe the experimental situation at AMOS. However, the data can be fit with reasonable success with a physically motivated model which includes both an angle independent and dependent term. Furthermore, there is some evidence to support the conclusion that non-homogeneity, non-isotropy and non-stationarity should be associated with low altitude effects.

3.4.2.3 Short-Term Statistics

Seeing Monitor data taken with short averaging times was also collected during the period from 17 July 1978 to 11 August 1978. The procedure used was to acquire a bright star (m $\leq$ 3) near zenith and collect many cycles of averaged data over periods of $\sim$ 20 to 30 min in length. In order to allow short averaging times, all inputs to the PDP-8 data processing system were eliminated except the two Seeing Monitor signals. Two different sample sizes were used: 5,000 and 1,000. The former resulted in a 1 min averaging time, whereas the latter yielded a 12 sec averaging time. The data output time for both was $\sim$ 6 sec per cycle. The resulting average voltages were converted to values of r_o at a wavelength of 5000 Å. The data was collected with 600 Å bandwidth filters centered at 6200 Å. In total, thirteen such data runs were collected on seven nights.
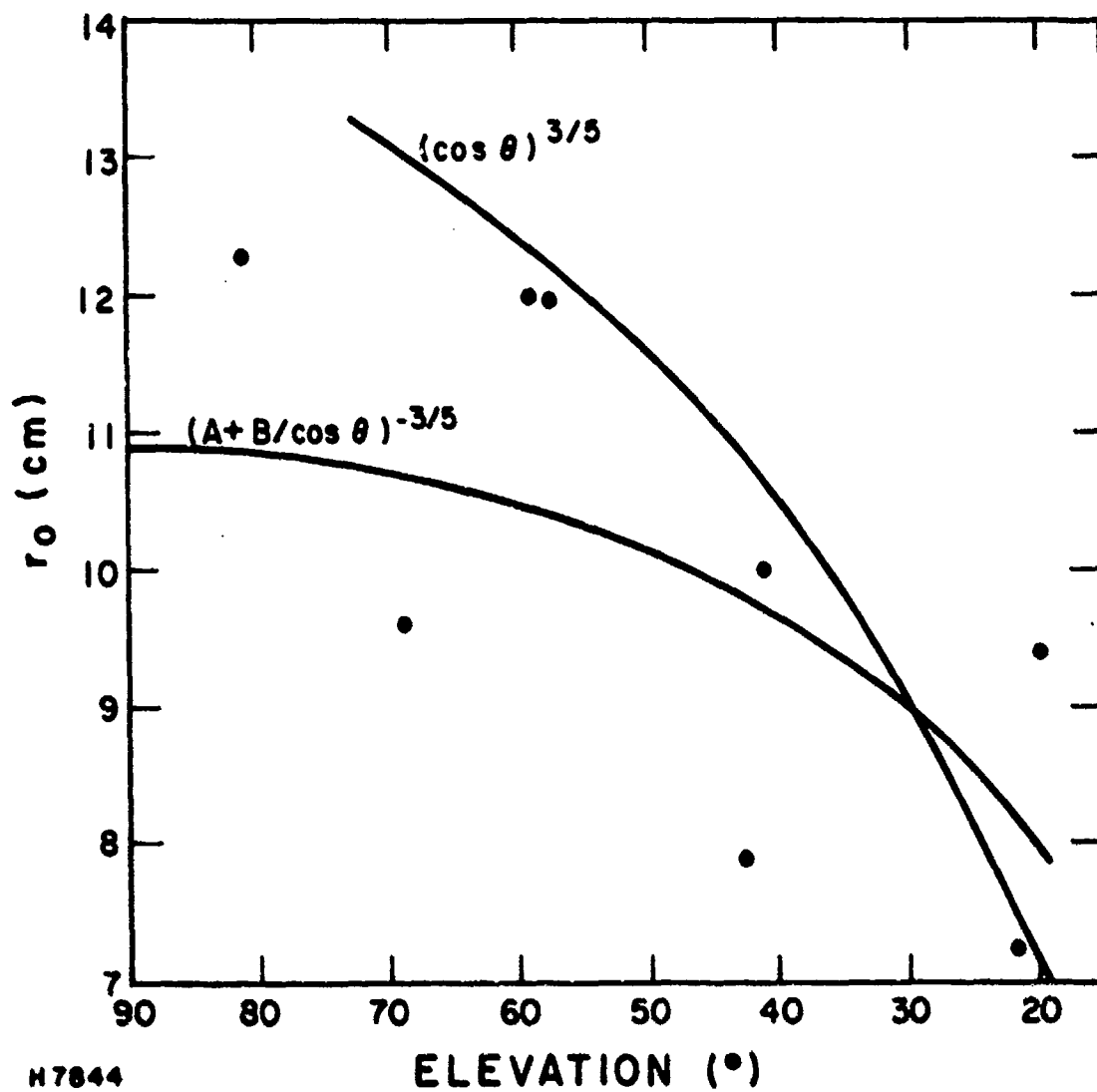
Figure 17   Seeing Monitor Angular Data, 18 July 1978, Run #4.
The solid lines are least square fits to the indi-
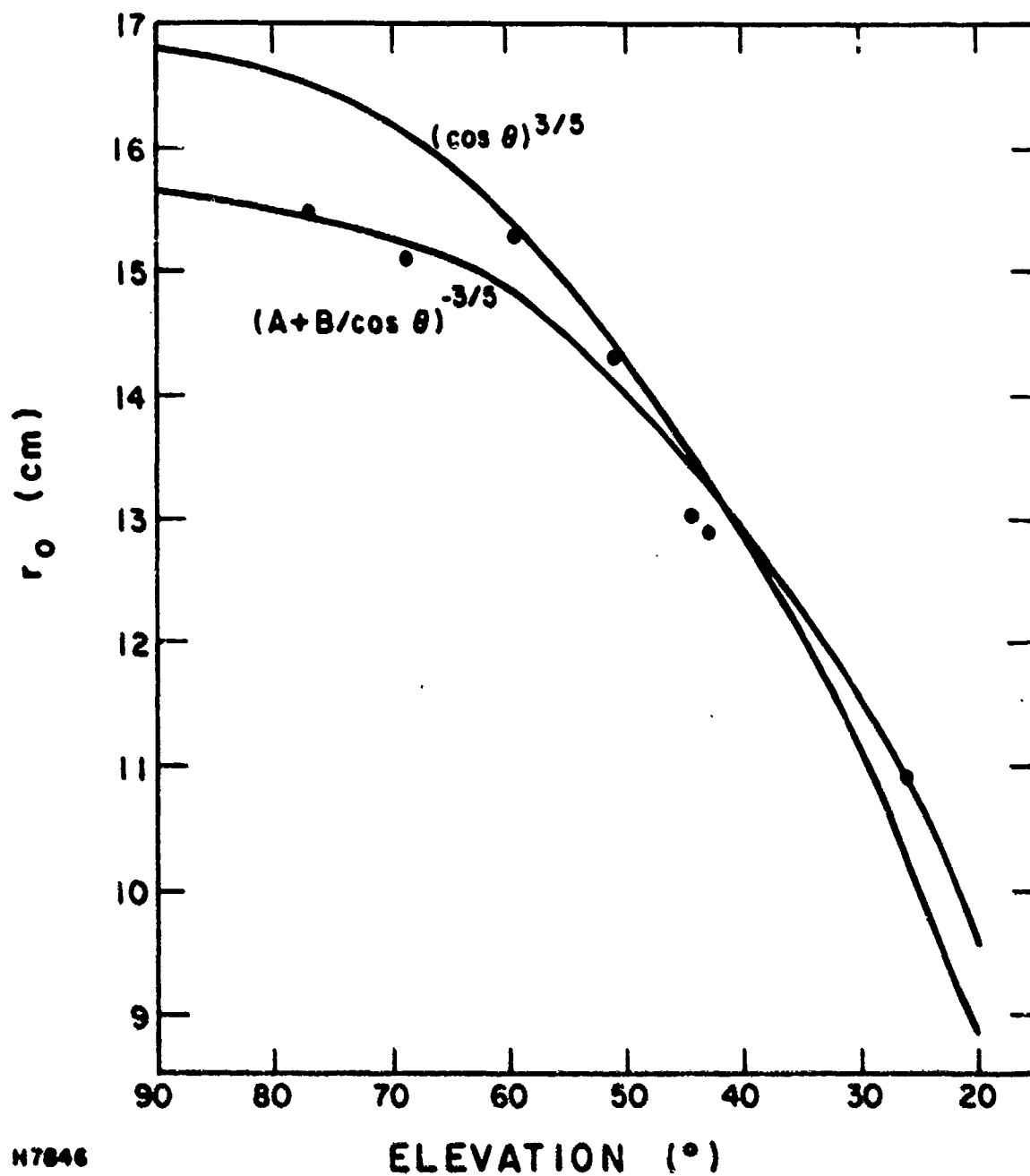cated functions.

Figure 18 Seeing Monitor Angular Data, 21 July 1978, Run #3. The solid lines are least square fits to the indicated functions.
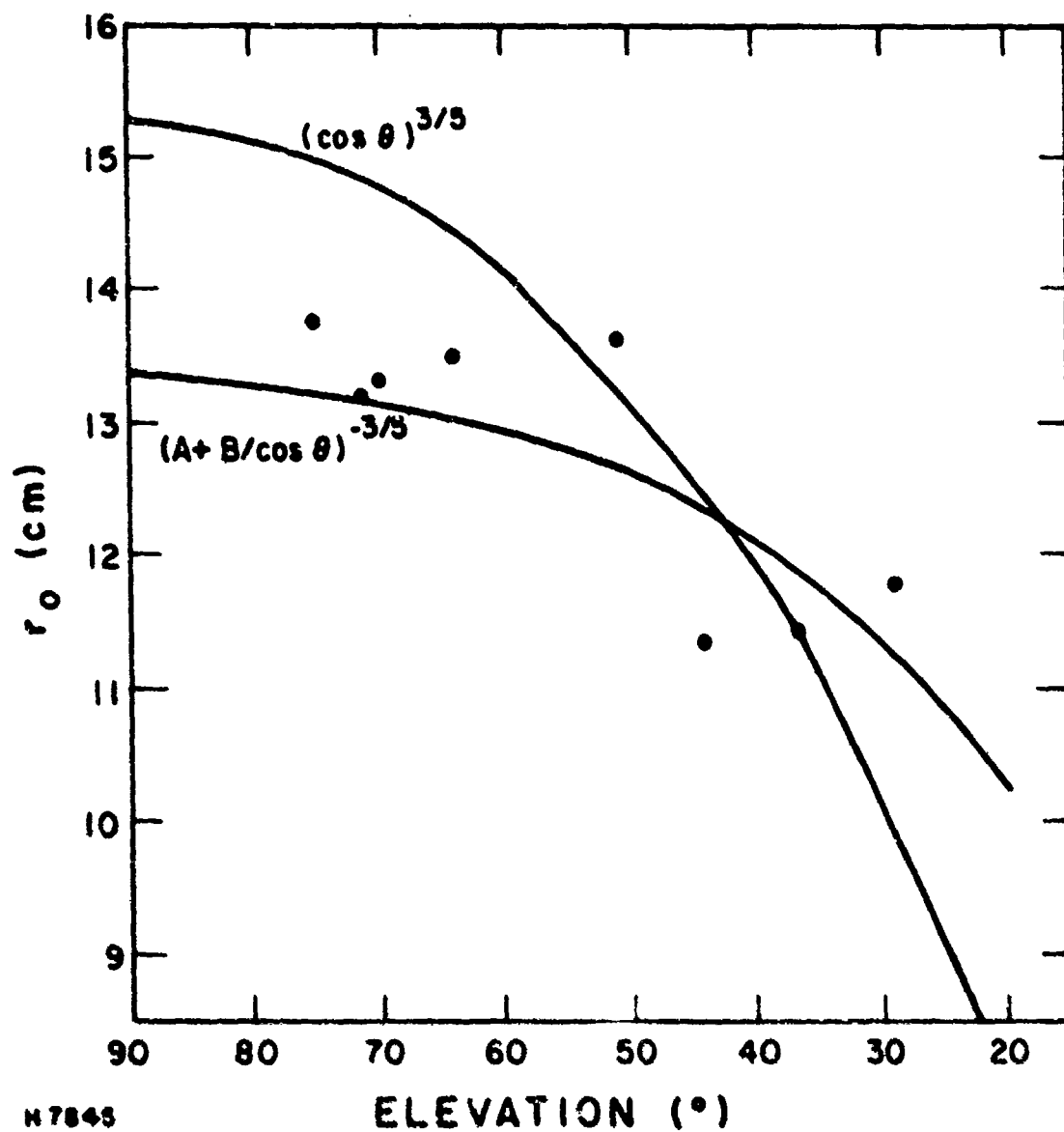
Figure 19   Seeing Monitor Angular Data, 11 August 1978, Run #2.
The solid lines are least square fits to the indi-
cated functions.

TABLE 6
NUMERICAL FIT TO ANGULAR DATA

DATA SET	$r_0(o)$ CM	$\int C_n^2 \, ds \times 10^{-13} \, m^{+1/3}$		
		TOTAL	Θ INDEPENDENT	Θ DEPENDENT
18 JULY #1	10.8	6.16	4.04	2.12
21 JULY #3	15.7	3.30	1.12	2.18
11 AUG #2	13.3	4.35	3.09	1.26

The results obtained from these measurements are displayed in Figures 20 through 32. The vertical axis is the value of r_o, whereas the horizontal axis is the cycle number (time). The value of r_o from channel one, channel 2 (orthogonal to Ch 1) and the two channel average, are denoted by a box, triangle, and x, respectively. These symbols are used for every other point, the intermediate values are indicated by breaks in the lines. Run averages ($\langle R \rangle$) and standard deviations (sigma) for both channels and the two channel average are also given in the Figures. $\langle \text{Delta} \rangle$ and sigma Δ are the mean and standard deviation of the difference in the two channels, respectively. Also given are the sample size corresponding to an averaging time of 1 min (N = 5,000) or 12 sec (N = 1,000).

A variety of behavior is seen in the data varying from the rather smooth and relative constant values of r_o of Figure 24 to the rapid and apparently random fluctuations of Figure 26. In general, channel two yields a lower value of r_o than channel one. This behavior has been observed consistently in the past leading to the conclusion that a dc offset is inherent in the instrumental calibration. Hence, final results have always been reported in terms of the two channel average. However, there are several cases where the channels cross over for a portion of the run (Figure 27 and 29) or reverse the relative magnitude for most of the run (Figure 30). Such behavior can obviously be associated with non-isotropy although it is likely that an instrumental bias also is present in the data.

It is also clear that higher point to point fluctuation exist in the 12 sec averaged data than in the 1 min average data. While this might be due to temporal non-stationarity, it is not entirely clear that it is not just due to the smaller sample size of the former data.

A rather dramatic effect observed in several runs is a large change in r_o which lasts for one or several cycles. Examples of this effect occur at the 22nd cycle of Figure 32 and the 18th cycle of Figure 29. These large, intermittent changes cannot be associated with the statistics of a stationary ensemble. A number of AMOS observers, while viewing a stellar image under high magnification, have seen occasional sudden changes in size and structure which are undoubtedly the same effect seen in this data. Furthermore, intermittencies in atmospheric turbulence data have been reported elsewhere.[33]

In summary, the short time average data reported here shows a variety of behavior including probable non-isotropy, temporal non-stationarity and intermittency on time scales of seconds to minutes. Such effects are not unique to AMOS, and reinforce the conclusion that propagation through atmospheric
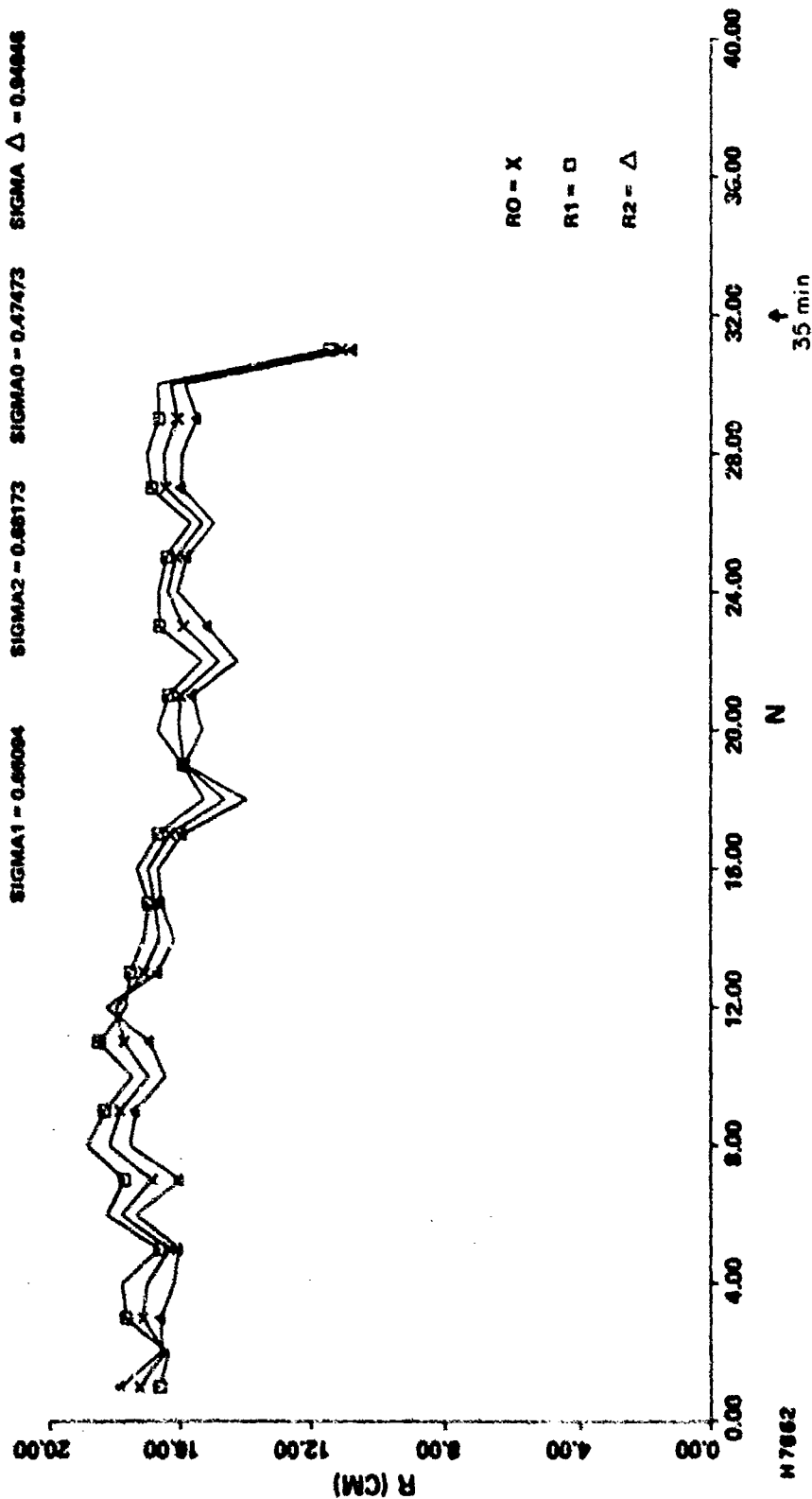
Figure 20   Seeing Monitor Short Term Statistics, 17 July 1978,
            Run #2 N = 5000.
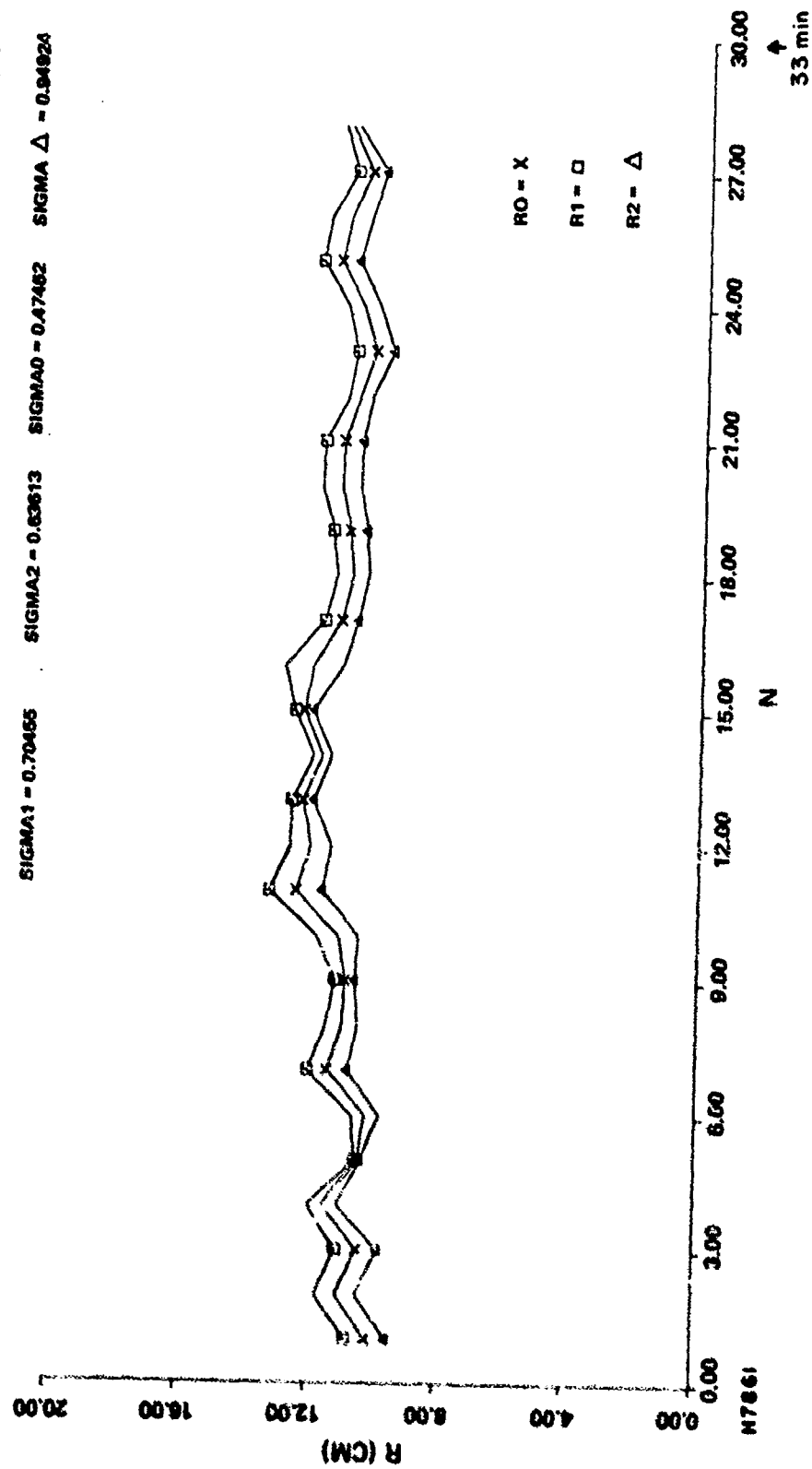
Figure 21   Seeing Monitor Short Term Statistics, 18 July 1978,
             Run #2 N = 5000

71
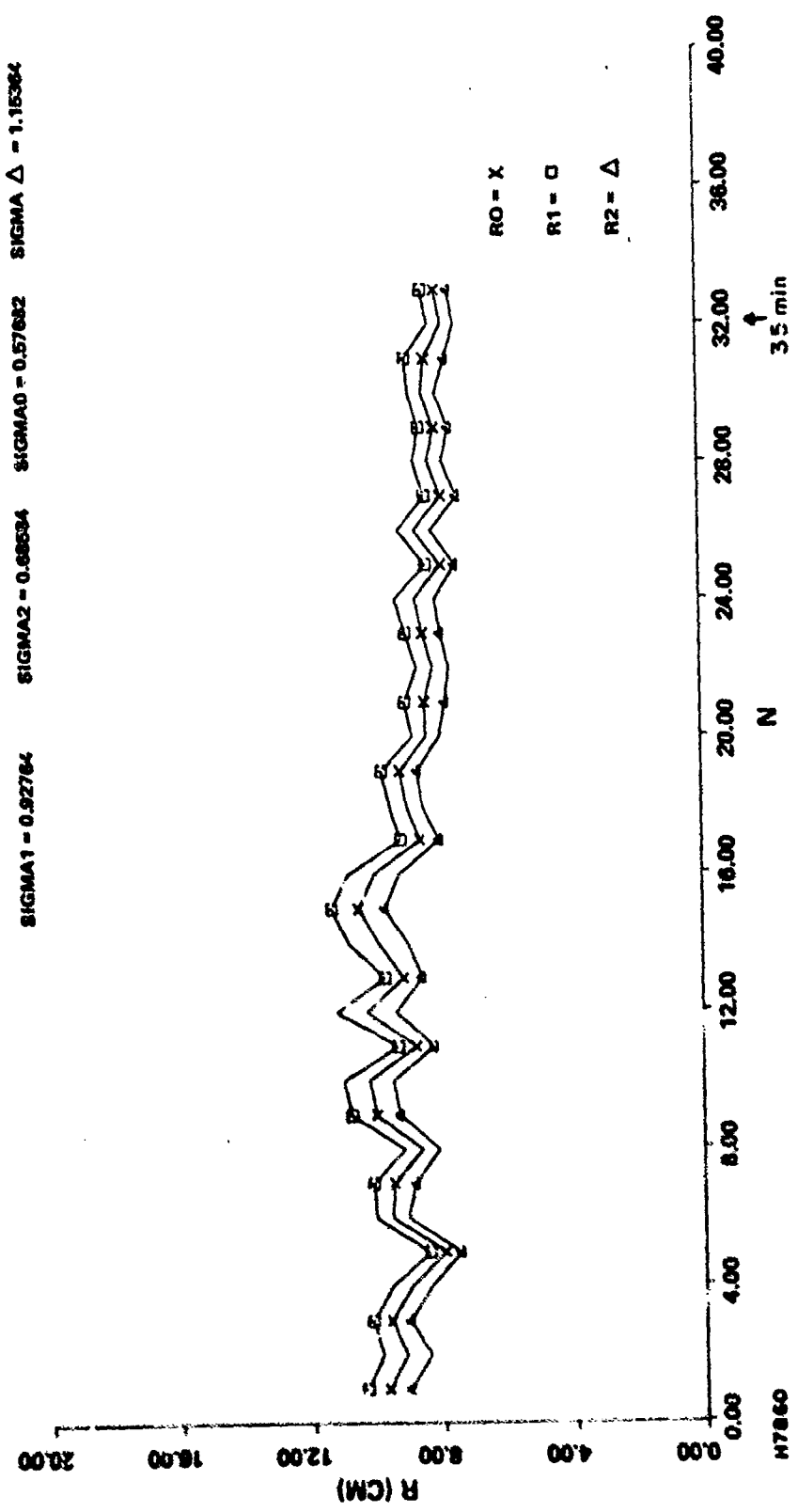
Figure 22   Seeing Monitor Short Term Statistics, 18 July 1978,
            Run #4 N = 5000

72
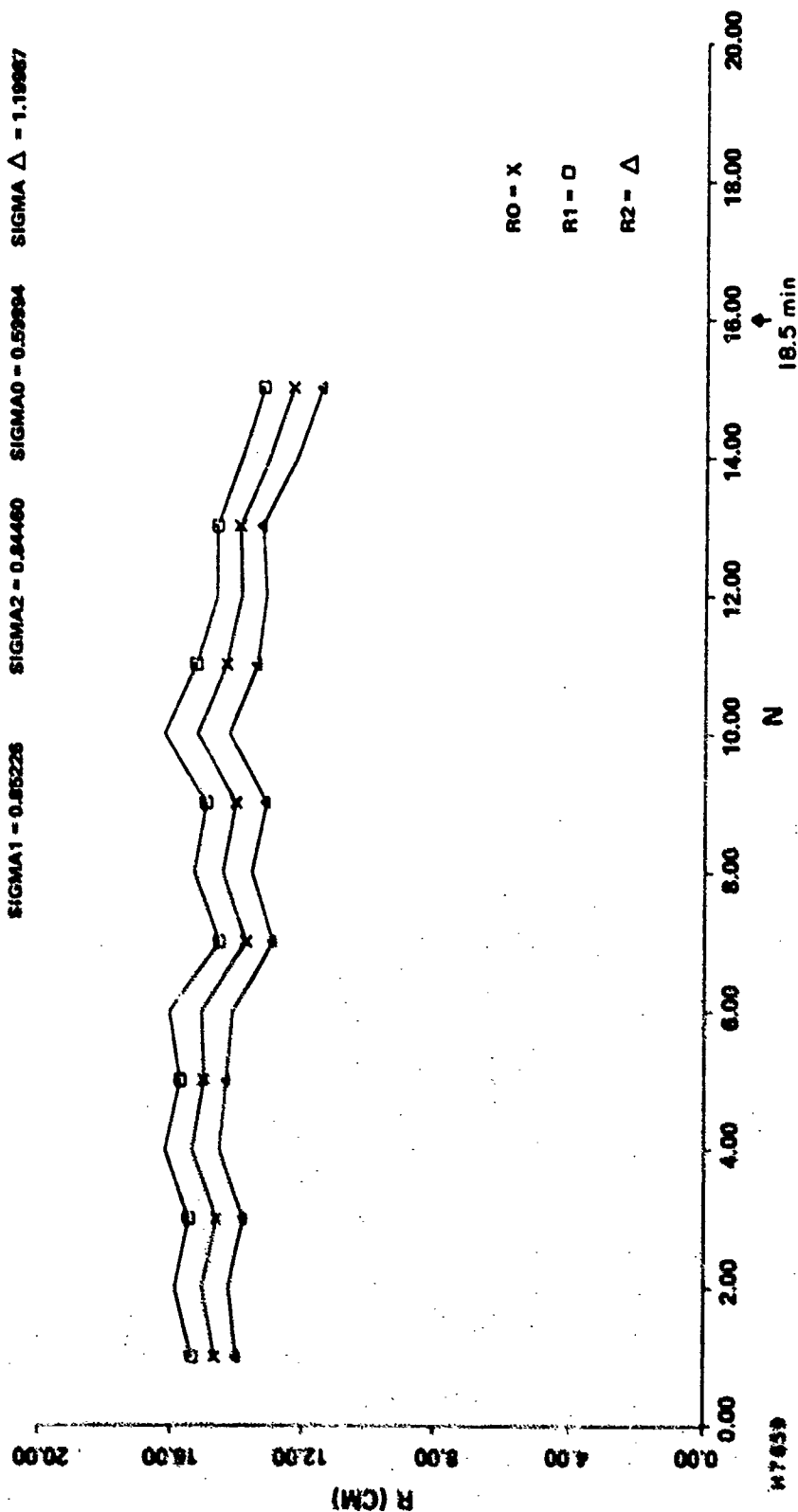
Figure 23   Seeing Monitor Short Term Statistics, 21 July 1978,
Run #2 N = 5000
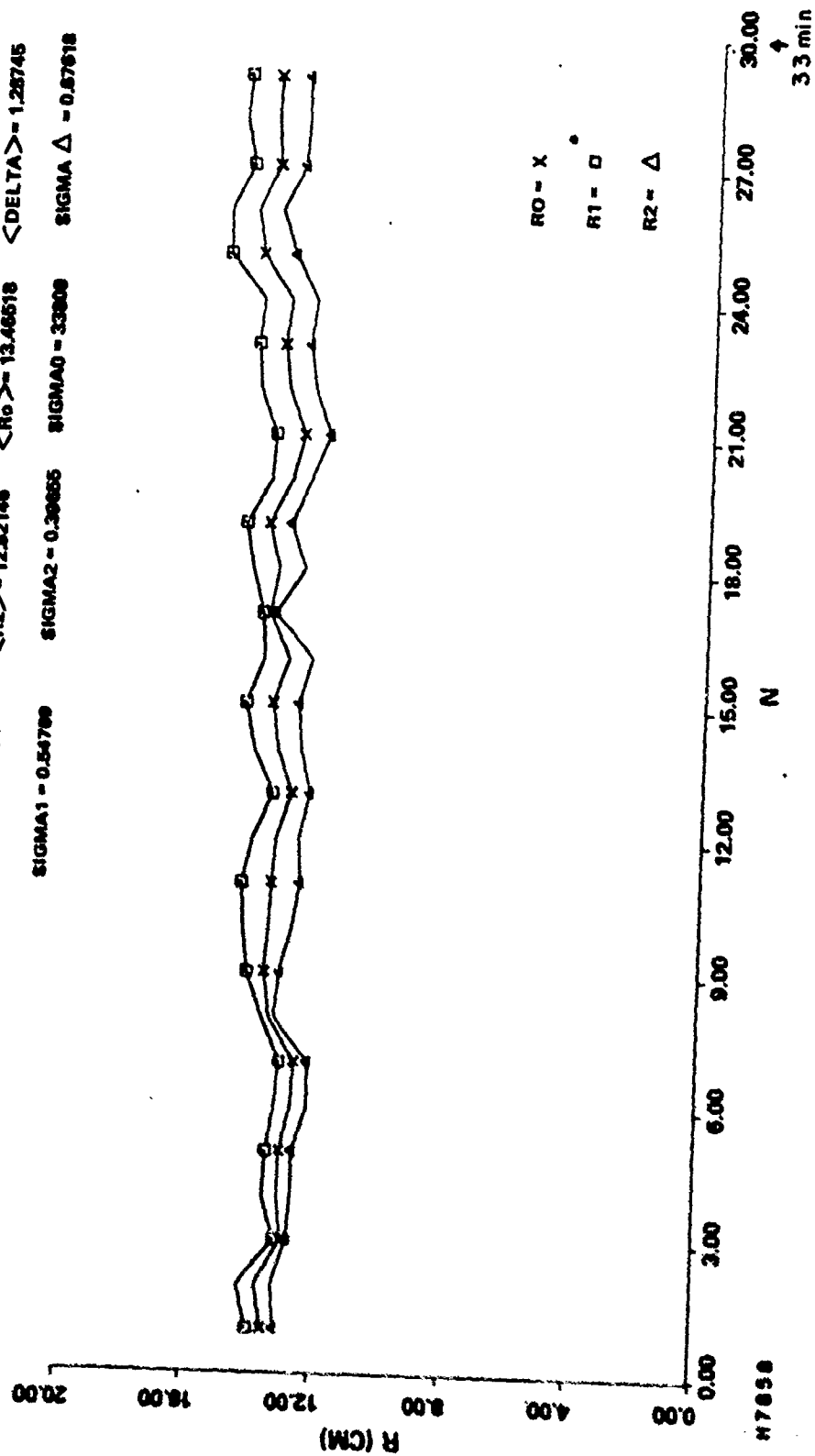
Figure 24   Seeing Monitor Short Term Statistics, 21 July 1978, Run #4 N = 5000

74
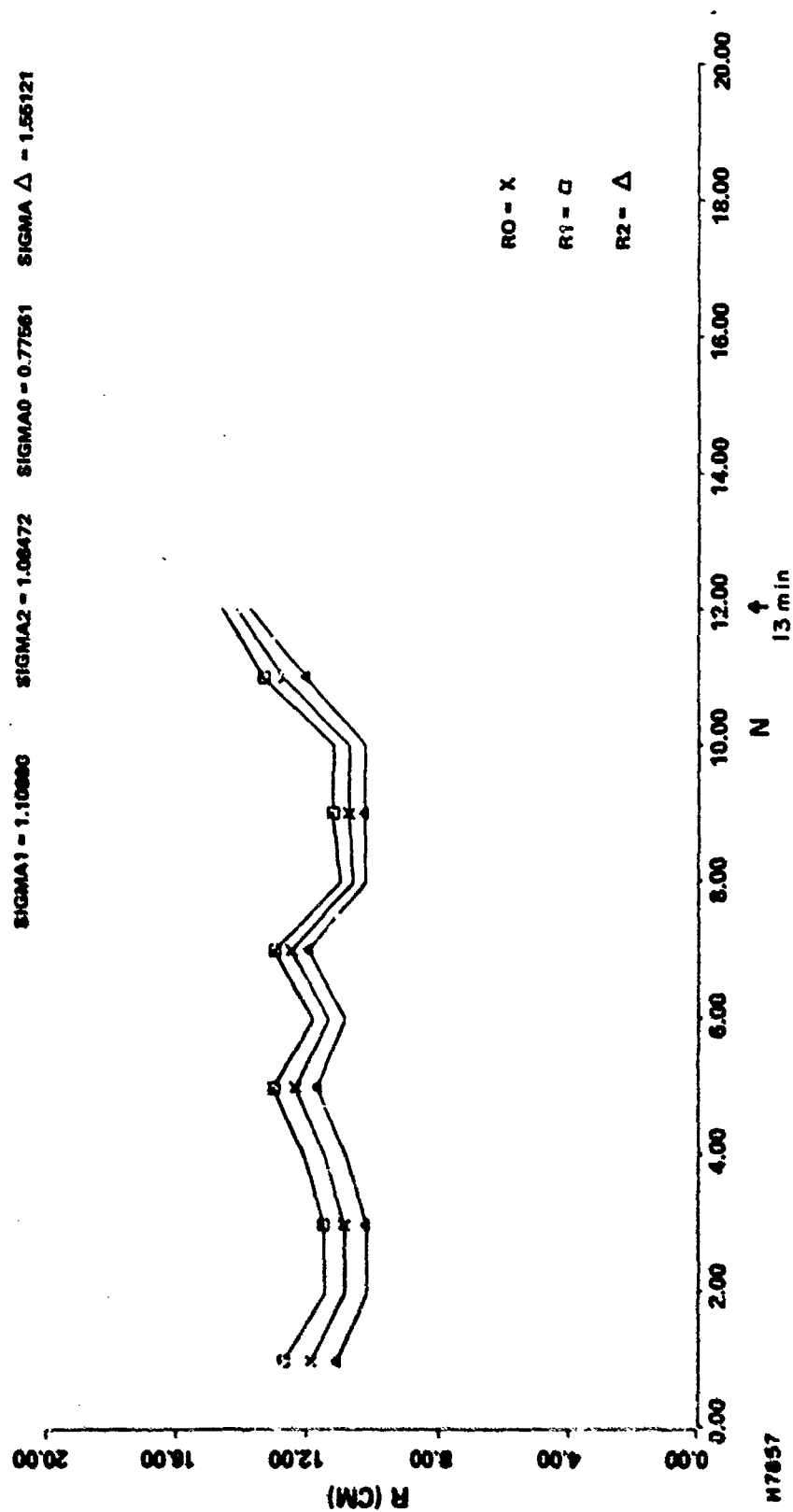
Figure 25   Seeing Monitor Short Term Statistics, 24 July 1978,
Run #3 N = 5000
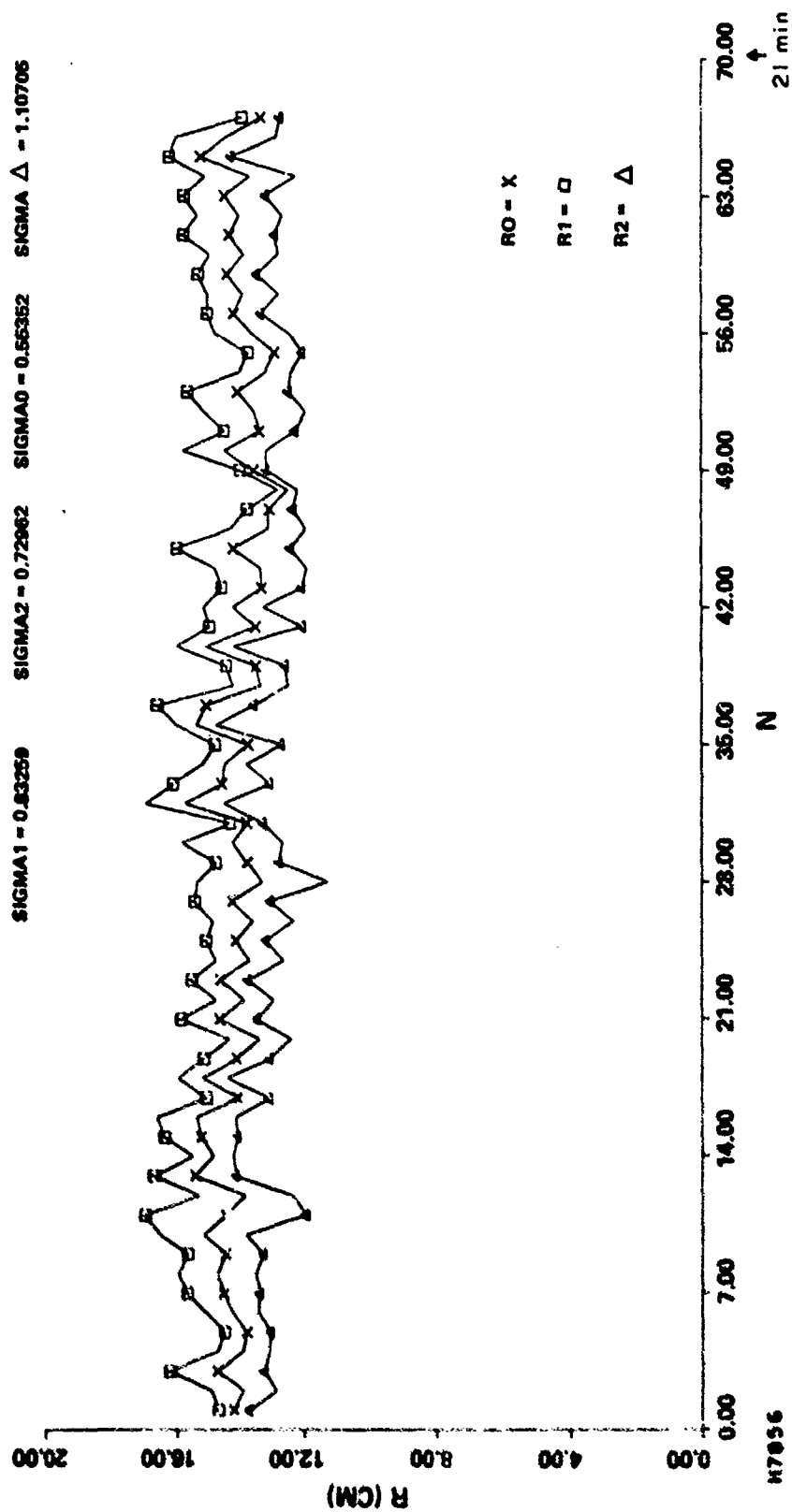
Figure 26. Seeing Monitor Short Term Statistics, 24 July 1978, Run #5 N = 1000
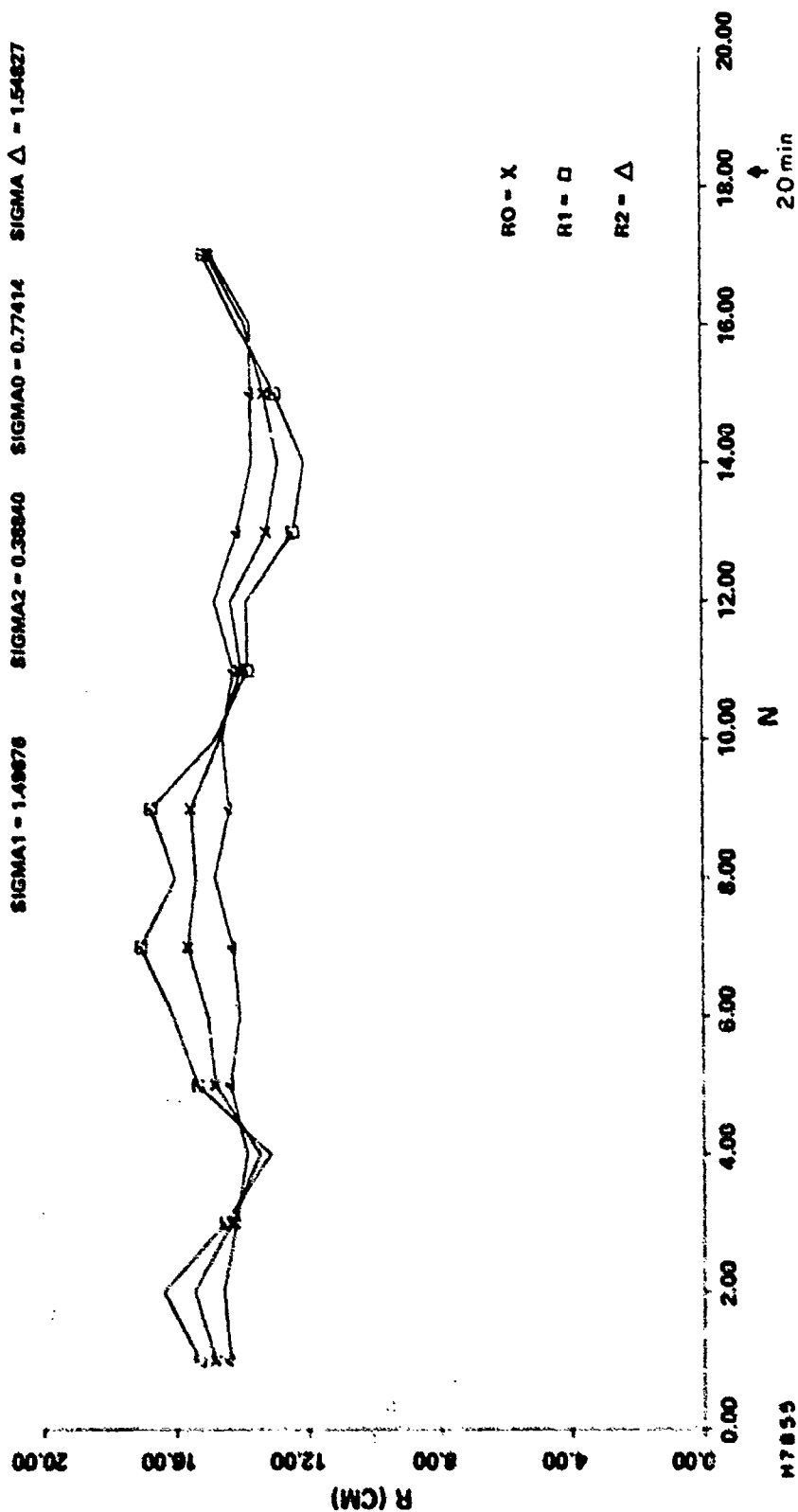
Figure 27   Seeing Monitor Short Term Statistics, 9 August 1978,
             Run #2 N = 5000
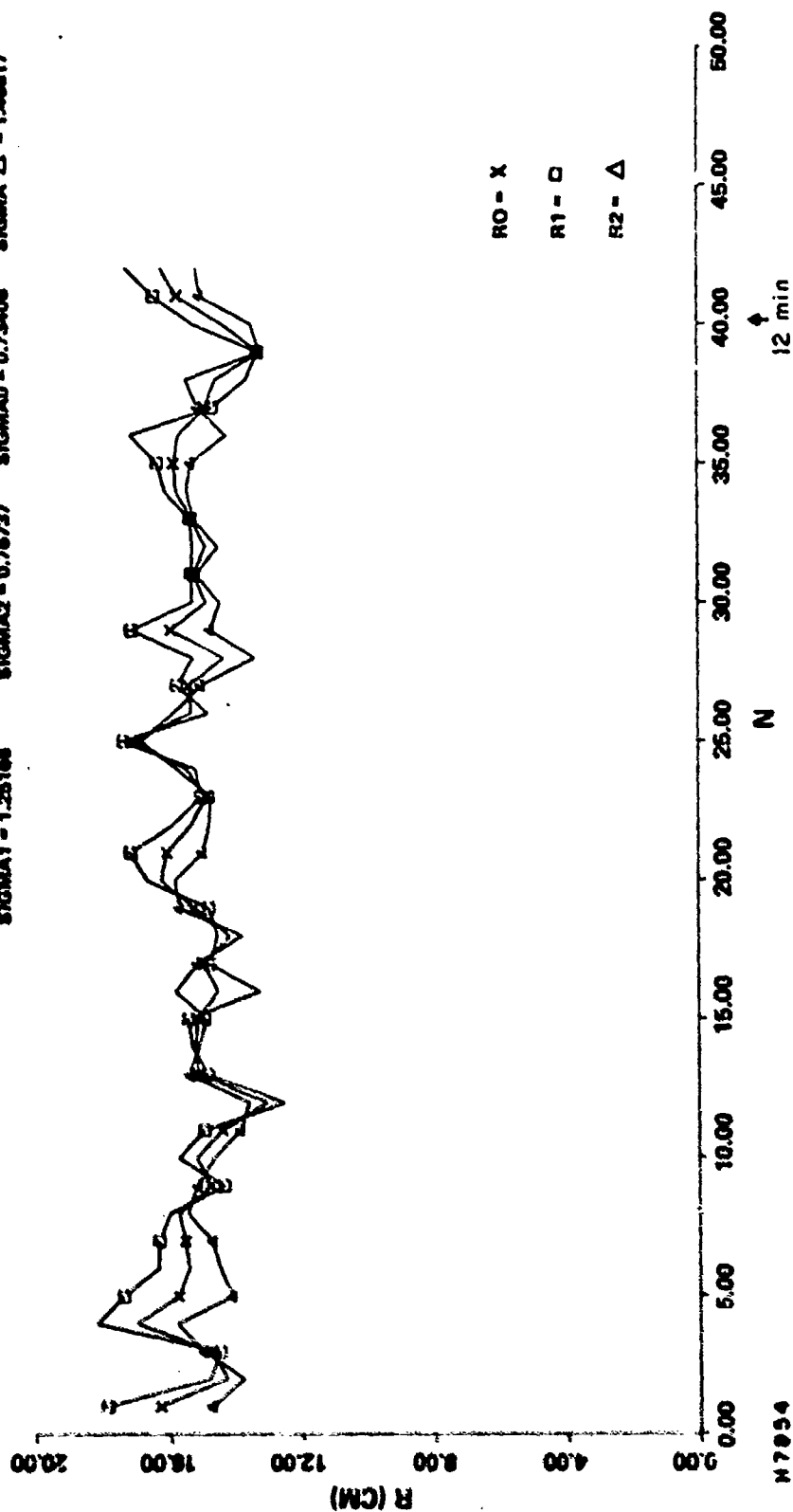
Figure 28   Seeing Monitor Short Term Statistics, 9 August 1978,
            Run #3 N = 1000

78
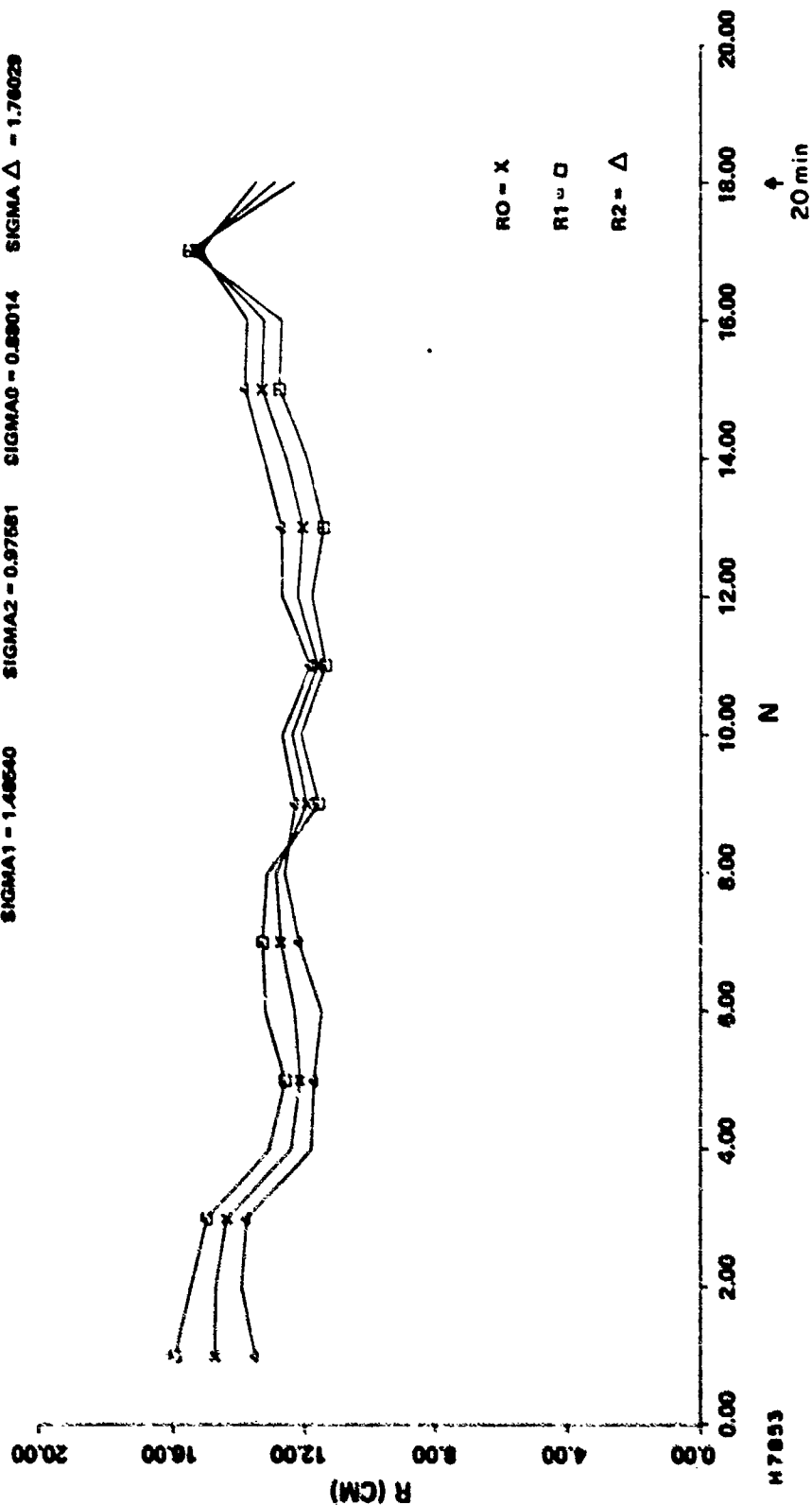
Figure 29   Seeing Monitor Short Term Statistics, 10 August 1978,
            Run #5A N = 5000
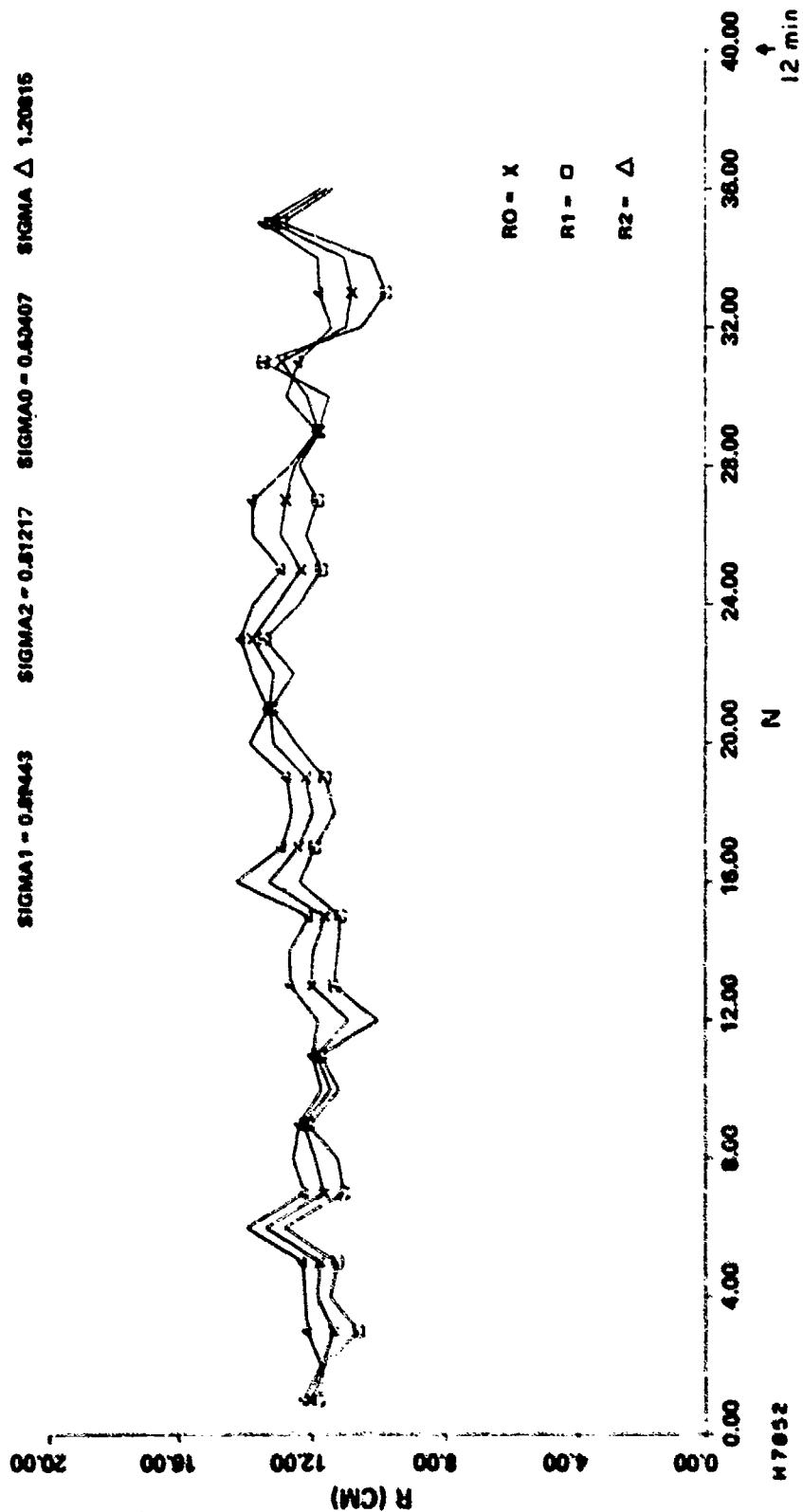
Figure 30   Seeing Monitor Short Term Statistics, 10 August 1978,
Run #5B N = 1000
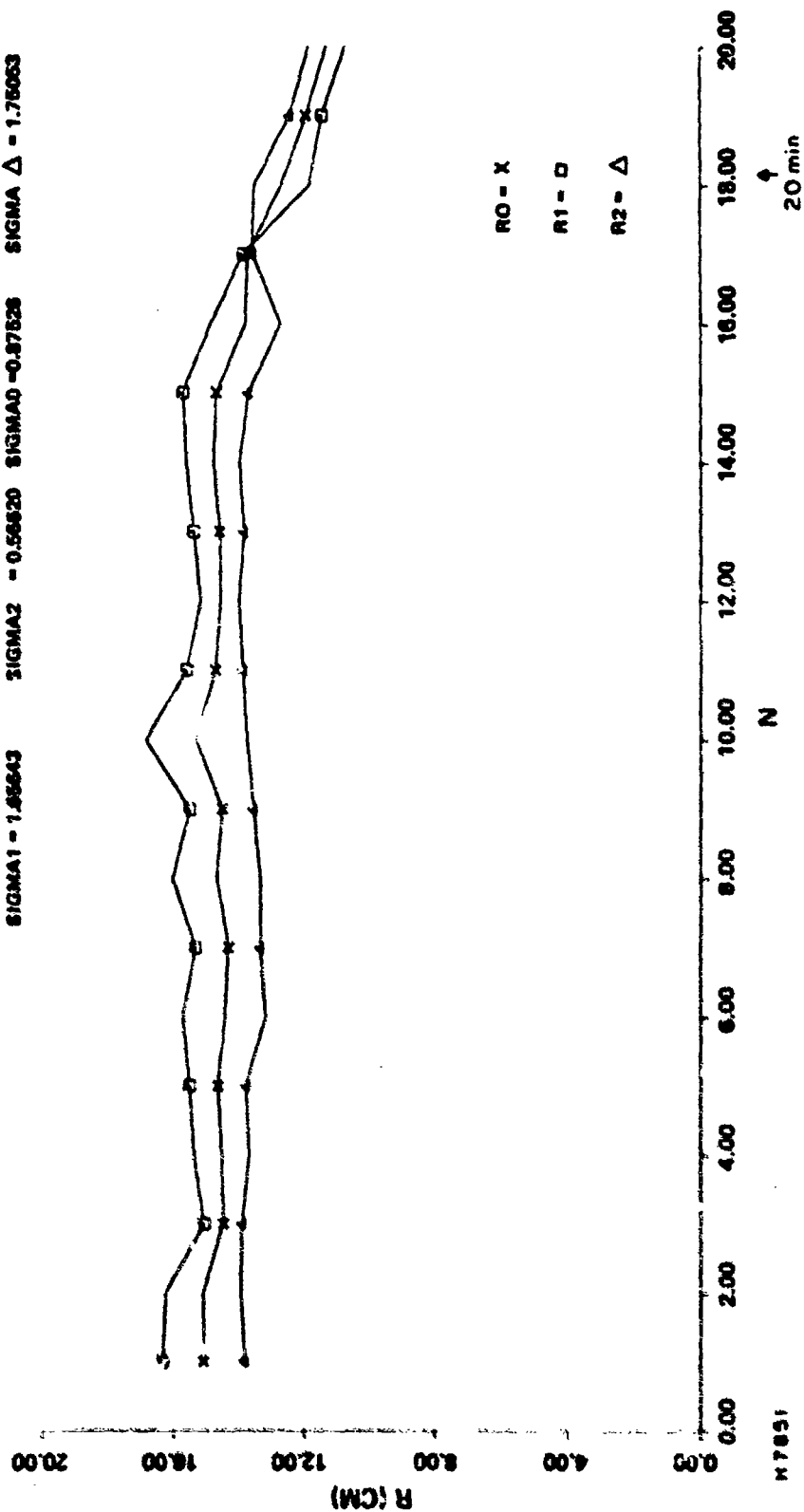
Figure 31   Seeing Monitor Short Term Statistics, 11 August 1978,
Run #5A N = 5000
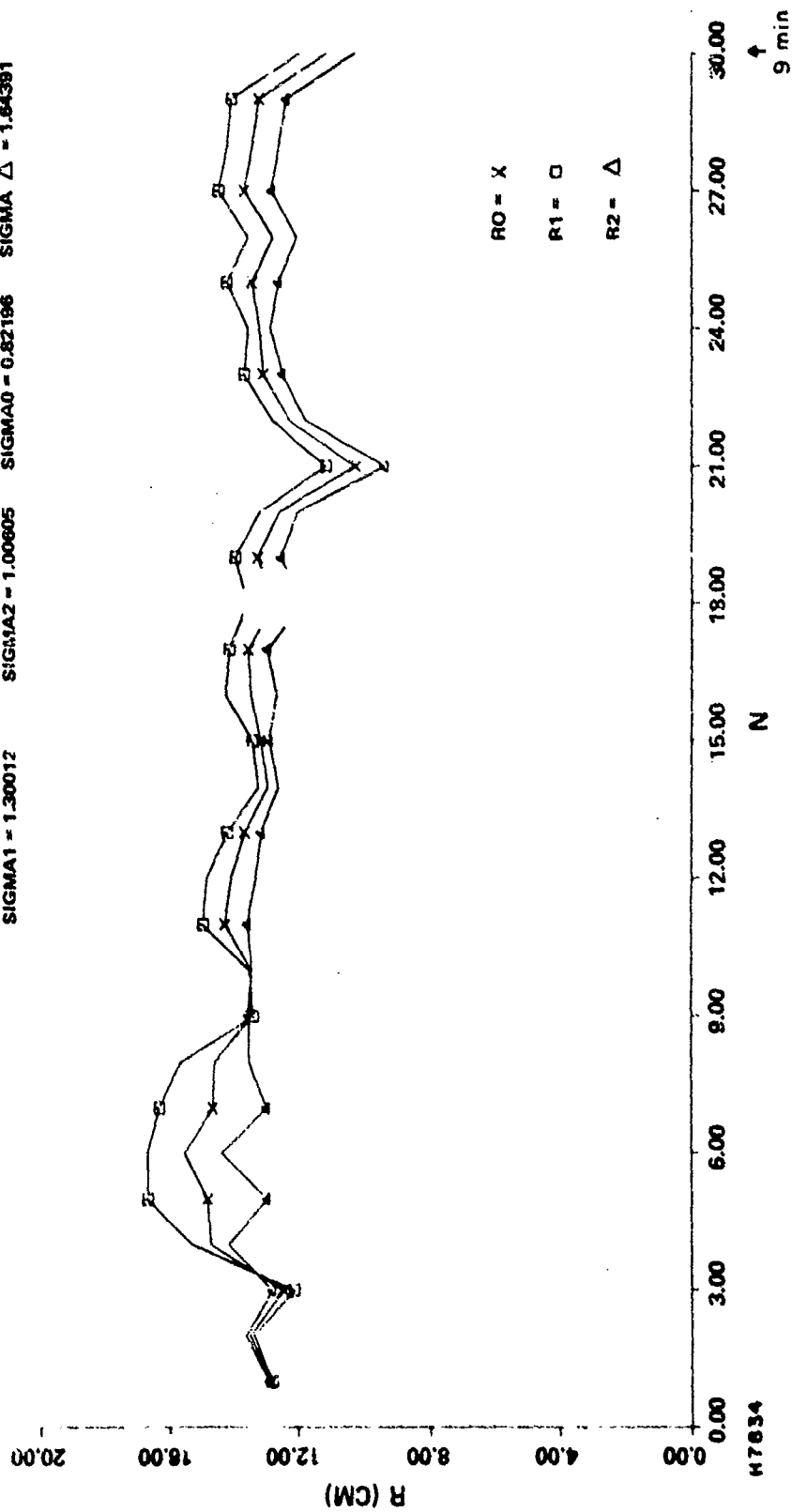
Figure 32   Seeing Monitor Short Term Statistics, 11 August 1978,
Run #5B N = 1000 .

turbulence is a complex problem to characterize experimentally. The detailed application of a theory and "average" properties of the atmosphere to an optical system operating in this environment should be approached with care and some caution.

3.4.3 Star Sensor

3.4.3.1 General

A variety of activities related to the NOAA Star Sensor were carried out during the period of this report. Most important of these were the reprocessing of the Model I data and the noise characterization measurements for Model II. Some additional routine data collection operations were carried out but primarily with the objective of validating system performance. The data tended to confirm previously reported results[5] and, hence, are not specifically reported here, although they are included in the average data discussed in Section 3.4.3.3.

3.4.3.2 Model I Reprocessed Data

As was discussed in a previous report,[5] a comparison of average upper altitude turbulence profiles obtained with the two models of the Star Sensor indicated a major disagreement in results, particularly in the 2.5 km to 5.0 km range (above the site). In order to firmly establish that this was not due to unusual statistics, additional data were collected with the Model II instrument which resulted in the strengthening of the previous conclusion.

Subsequently, several discussions were held with NOAA personnel who agreed to re-analyze the operation of both instruments. As a result of this analysis, it was discovered that an assumption made in the Model I data reduction algorithm was not obeyed by the physical implementation.[38] Therefore, the values of index of refraction structure parameter (C_n^2) obtained and previously reported were incorrect. Fortunately, because of the linear nature of the processing algorithms, it was possible to develop new, correct profiles from the old, incorrect profiles; however, the corrected profiles have only four altitude levels in contrast to the seven levels of the original data. Furthermore, the numerical values of the aperture-averaged log-amplitude variance predicted by the profiles is maintained. Therefore, the previously reported comparison between the profile derived and directly measured values for this parameter remain valid. The relationship between the new and old values of C_n^2 is as follows:

$$C_n^2(j) = \sum_i A_{ji} \, C_n^2(i); \quad i = 1\ldots7; \quad j = 1\ldots4 \qquad (9)$$

---

38. R. Lawrence, NOAA Environmental Research Lab, private communication.

where $C_n^2(i)$ are the old values and $C_n^2(j)$ are the new values. Numerical values for the coefficients, A_{ji}, are given in Table 7. The peak (central) height and half maximum width of the four weighing functions associated with the new profile are given in Table 8.

The reprocessed individual profiles are given in Table 9. Included in the table are the day, month, year, and start time for each profile, the four values of C_n^2 and the unweighted integral.

$$IN = \int_{> 700 \text{ m}} C_n^2(s) \ ds \qquad (10)$$

The data set denoted "A" corresponds to the reprocessing of the data tabulated in report RADC-TR-70-70,[3] whereas that denoted "B" corresponds to the data tabulated in report RADC-TR-77-232.[4]

Nightly and monthly average profiles are given in Tables 10 and 11, respectively. The same information is included as noted above. In addition, the total number of 20-min profiles in the various averages is noted.

Statistical parameters of the entire Model I data set are given in Table 12. The ensemble includes 160, 20-min profiles collected on 35 nights over a 15 month period. These results are presented graphically in Figure 33 which shows the average, average plus one sigma, maximum and minimum value profiles as a function of altitude. The latter two profiles were generated by combining the ensemble maximum and minimum values at each altitude into a single profile; therefore, they do not represent an actual physical situation observed on a specific occasion. The width of the weighing functions has not been indicated. The values are plotted against the nominal central height of each layer. As can be seen, the profiles tend to flatten in the vicinity of those altitudes associated with a meteorological tropopause but do not show a tropopause bump. However, the conclusion that a bump does not occur in reality is not warranted because of the broad nature of the weighing functions.

The histogram and cumulative probability distribution for the entire four level ensemble of empirical C_n^2 values are given in Figures 34 and 35. In order to present all of the data on a single plot, the values at each altitude were normalized by dividing by the average value of C_n^2 at that altitude. The natural logarithm of the normalized data was then used to generate the CPD. The reason for this was to allow a direct comparison of the

85

TABLE 7

NUMERICAL COEFFICIENTS FOR CORRECTED MODEL I STAR SENSOR PROFILES

NEW j= \ OLD i=	1	2	3	4	5	6	7
1	9.6	0.0	0.0	10	0.0	0.0	18
2	0.0	0.0	4.4	0.0	0.0	3.1	2.3
3	0.0	0.0	0.0	0.0	2.2	0.0	1.8
4	0.0	0.0	0.0	0.11	0.0	0.0	1.1

TABLE 8

CENTRAL HEIGHT AND WIDTH OF MODEL I STAR SENSOR
WEIGHING FUNCTION

$c_n^2(j)$ j =	CENTRAL HEIGHT (KM)	HALF-MAXIMUM WIDTH (KM)
1	1.5	1.65
2	3.1	2.40
3	6.75	6.31
4	12.75	13.27

TABLE 9

MODEL I STAR SENSOR PROFILES

SET	DAY	MONTH	YEAR	TIME (HST)	$C(I)$ $(\times 10^{-18} \text{ m}^{-2/3})$	$C(II)$ $(\times 10^{-18} \text{ m}^{-2/3})$	$C(III)$ $(\times 10^{-18} \text{ m}^{-2/3})$	$C(IV)$ $(\times 10^{-18} \text{ m}^{-2/3})$	IN $(\times 10^{-15} \text{ m}^{1/3})$

TABLE 9

MODEL I STAR SENSOR PROFILES (Continued)

TABLE 9

MODEL I STAR SENSOR PROFILES (Continued)

TABLE 10

MODEL I STAR SENSOR NIGHTLY AVERAGED PROFILES

NIGHTLY AVERAGES				NUMBER OF	C(I) AVERAGE	C(II) AVERAGE	C(III) AVERAGE	C(IV) AVERAGE	IH AVERAGE
SET	DAY	MONTH	YEAR	PROFILES	$(\times 10^{-18}\ m^{-2/3})$	$(\times 10^{-18}\ m^{-2/3})$	$(\times 10^{-18}\ m^{-2/3})$	$(\times 10^{-18}\ m^{-2/3})$	$(\times 10^{-15}\ m^{1/3})$

TABLE 11

MODEL I STAR SENSOR MONTHLY AVERAGED PROFILES

MONTHLY AVERAGES SET	NUMBER OF PROFILES	MONTH	C(I) AVERAGE ($\times 10^{-18}$ m$^{-2/3}$)	C(II) AVERAGE ($\times 10^{-18}$ m$^{-2/3}$)	C(III) AVERAGE ($\times 10^{-18}$ m$^{-2/3}$)	C(IV) AVERAGE ($\times 10^{-18}$ m$^{-2/3}$)	IN AVERAGE ($\times 10^{-18}$ m$^{1/3}$)
A	37	NOVEMBER 76	2.36803E+02	1.81256E+01	4.96776E+00	1.88870E+00	4.88020E+02
A	12	DECEMBER 76	2.34776E+02	3.99652E+01	2.12437E+01	3.14939E+00	6.59137E+02
A	21	APRIL 76	2.41901E+02	3.35326E+01	1.15644E+01	2.12677E+00	5.80069E+02
A	23	MAY 76	1.74923E+02	2.73359E+01	6.09061E+00	2.37509E+00	4.89508E+02
A	10	JUNE 76	2.08088E+02	4.15095E+01	1.09181E+01	2.36433E+00	6.75765E+02
A	15	JULY 76	1.92954E+02	4.52895E+01	1.65536E+01	1.95776E+00	5.57521E+02
B	6	SEPT 76	1.57322E+02	2.00347E+01	1.30704E+01	1.03184E+00	3.54844E+02
B	13	OCTOBER 76	4.12653E+02	5.16061E+01	5.54004E+00	2.26417E+00	9.32151E+02
B		DECEMBER 76	1.39960E+02	9.38043E+01	3.56373E+01	3.88667E+00	8.31312E+02
B	10	JANUARY 77	1.92690E+02	5.63827E+01	1.66414E+01	3.79178E+00	6.07860E+02

TABLE 12

STATISTICAL PARAMETERS OF AVERAGE MODEL I PROFILE

NOMINAL ALTITUDE ABOVE SITE (KM)	C_n^2 ($\times 10^{-18} m^{-2/3}$)		
	MEAN	STANDARD DEVIATION	SD/M
1.5	240	189	0.79
3.1	35.3	34.3	0.97
6.75	11.3	10.1	0.89
12.75	1.96	1.72	0.88

INTEGRAL: MEAN   = $5.78 \times 10^{-13} m^{1/3}$

STANDARD DEVIATION = $3.76 \times 10^{-13} m^{1/3}$

(SD/M)   =   0.65

H7850
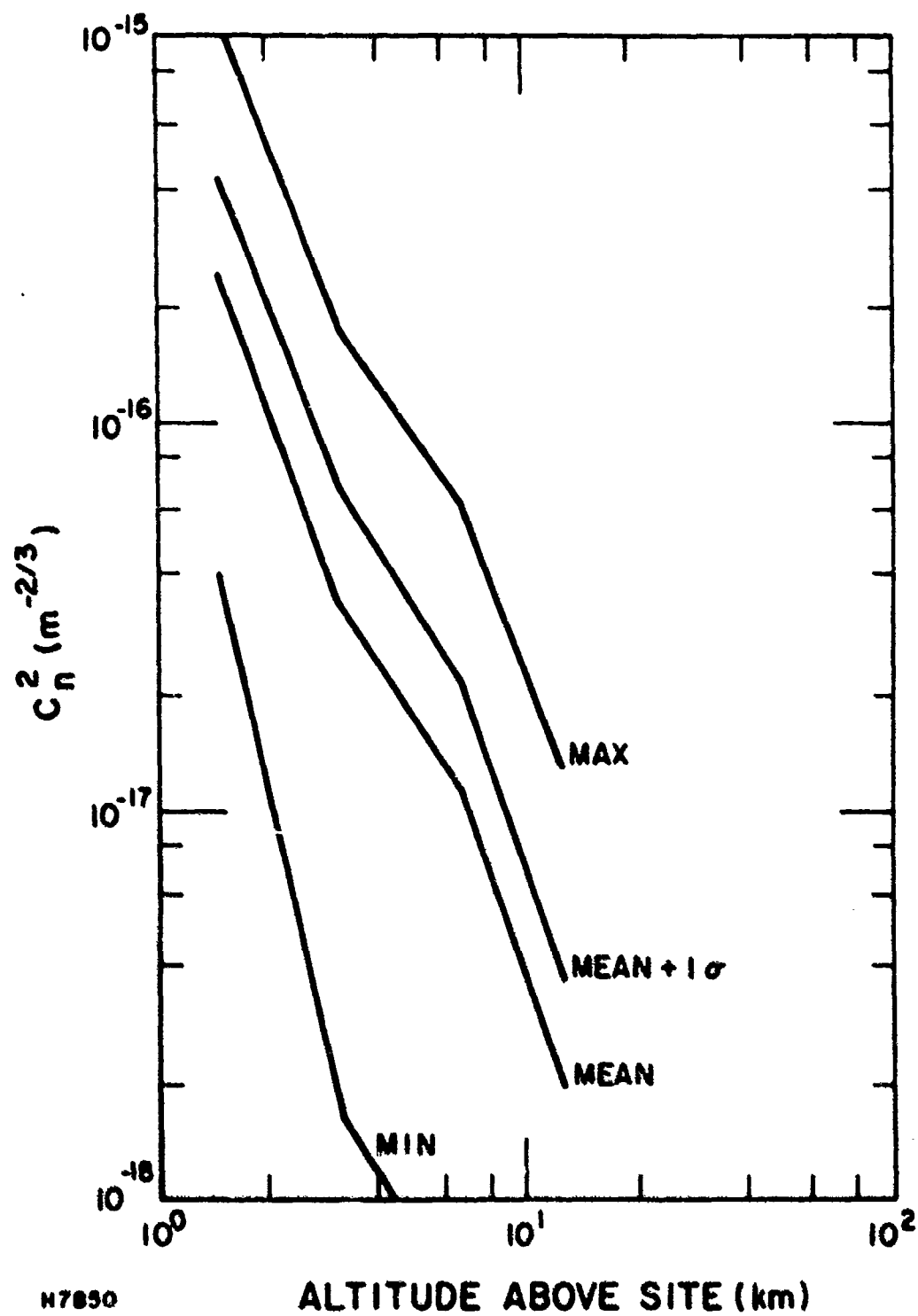
Figure 33   Statistical Properties of Model I Star Sensor Profile

94
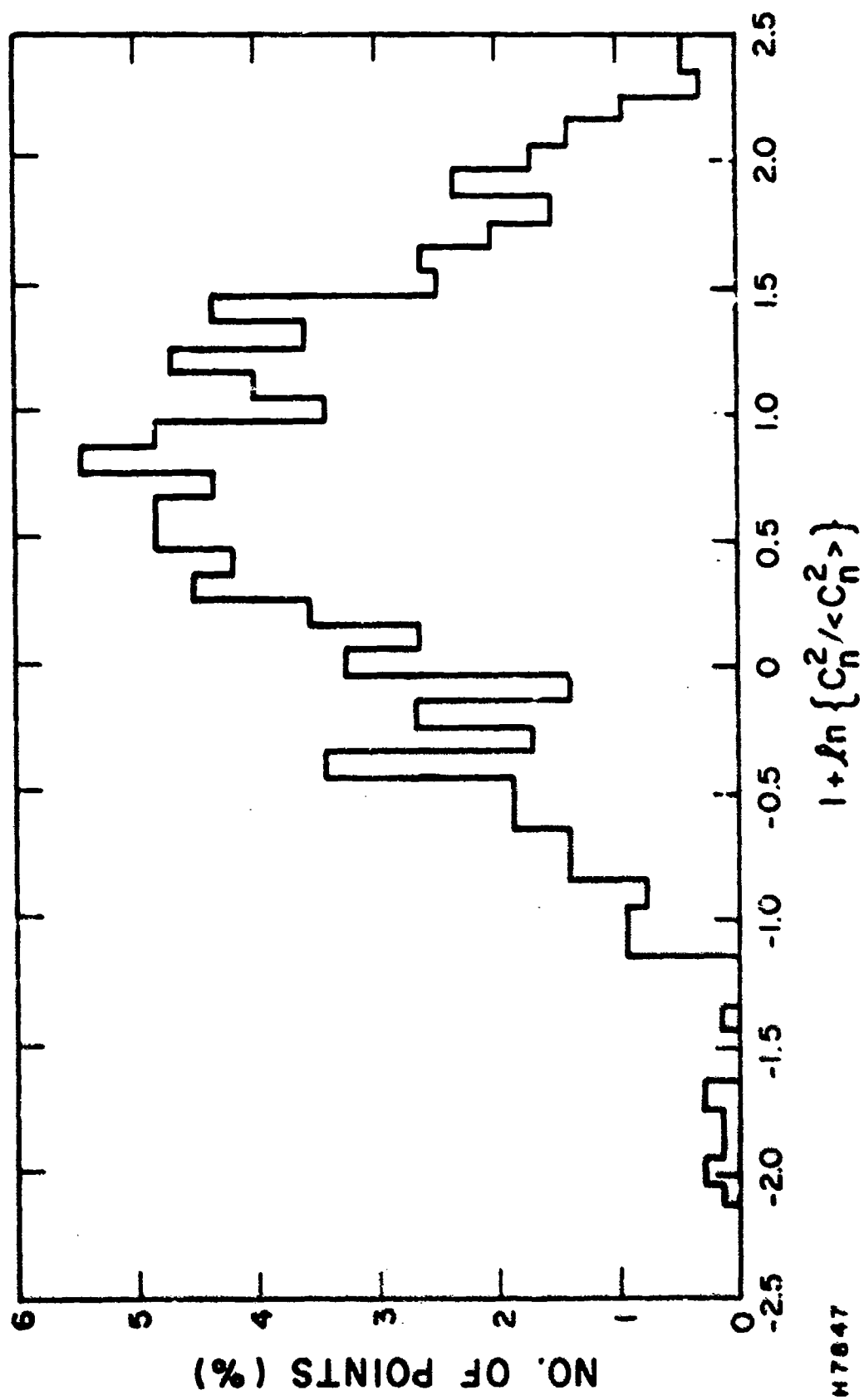
Figure 34 Normalized Model I Star Sensor Data – Histogram

H7847

95
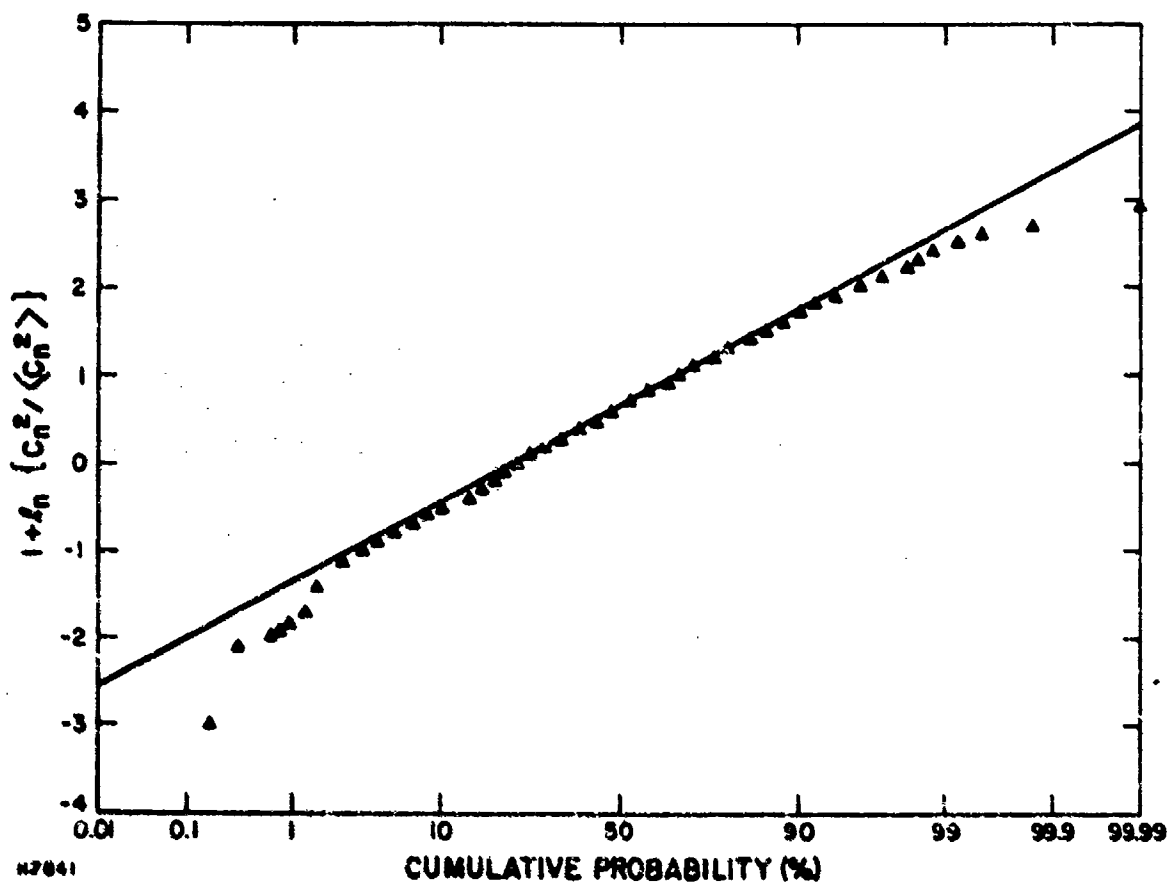
Figure 35   Normalized Model I Star Sensor Data - Cumulative
            Probability Function. The straight line is for
            Gaussian statistics with the empirical mean and
            variance.

data with the Hufnagel model[33] in which

$$C_n^2(h,t) = A(h,w) \ e^{r(h,t)} \tag{11}$$

where $r(h,t)$ is assumed to be a gaussian random variable with
zero mean and variance of two, and $A(h,w)$ is a deterministic
function of altitude (h) and average wind speed (w) but not time.
Hence,

$$\langle C_n^2 \rangle = A(h,w)e^1 \tag{12}$$

and

$$r(h,t) = 1 + \ln \left\{ C_n^2 / \langle C_n^2 \rangle \right\} \tag{13}$$

The solid line in Figure 35 represents a gaussian distri-
bution (log-gaussian for C_n^2) with the empirical mean and
variance of 0.655 and 0.756, respectively. The nonzero mean is
probably due to the finite and nonzero threshold of the Star
Sensor which would bias the mean to positive values. The vari-
ance of $r(h,t)$ assumes, of course, point averaging in time and
space. Hufnagel's model includes the altitude and time covari-
ance function which has two characteristic time scales (5 and
80 min) and two characteristic altitude scales (100 and 2,000 m).
The instrument bases its estimate of C_n^2 on data collected over
a 20-min time period. The weighing functions used in the pro-
cessing are of variable width. However, all are considerably
wider than 100 m; hence, an empirical variance of less than 2
is to be expected.

In summary, the reprocessed Model I Star Sensor data shows
higher levels of turbulence, particularly at lower altitudes
than did the original data. The statistics of the data are
essentially unchanged except for numerical values and still
compare favorably with the Hufnagel model.

3.4.3.3 Average Star Sensor Profile

The combined Model I and II Star Sensor results represents
a data base collected on fifty different occasions over a period
of several years. The Model I data includes 160, twenty min, four
level profiles whereas the Model II data includes 544, three min,
seven-level profiles. The Model II results are given in Table
13. The average profiles are given in Figure 36. The horizon-
tal lines represent the half-maximum widths of the weighing
functions associated with each of the eleven levels, whereas the

TABLE 13

AVERAGE MODEL II PROFILE

Level	C_n^2 ($\times\ 10^{-18}\ m^{-2/3}$)	Nominal Altitude Above Site (km)	Half-Width of Weighing Function (km)
1	150.0	2.2	1.4
2	31.1	3.4	1.7
3	9.34	5.2	2.0
4	2.29	7.3	2.0
5	2.18	9.4	3.2
6	1.57	14.0	4.5
7	1.31	18.5	4.0

$$\int_{>1500\ m} C_n^2\ ds = 3.05 \times 10^{-13}\ m^{1/3}$$

98
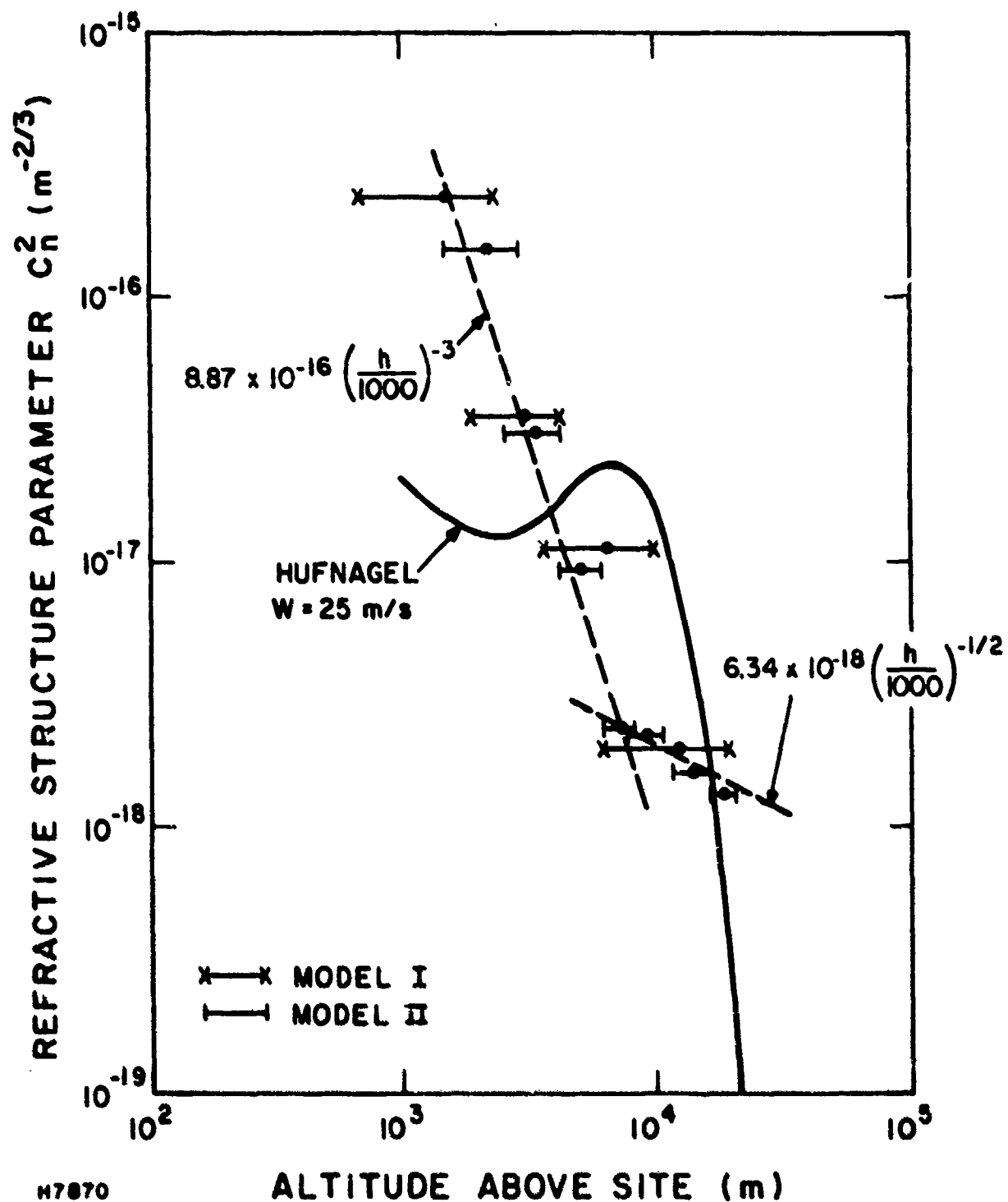
Figure 36   Models I and II Star Sensor Data. The solid line is
the best fit to the average Hufnagel wind correlated
model. The dashed lines are the best fit to the
power laws indicated.

solid circles indicate the nominal central altitude of each
level. As can be seen, the agreement between the two instru-
ments is quite good. Numerical values of integrated turbulence
associated with the two profiles are:

$$\text{MODEL I:} \int_{>700 \text{ m}} C_n^2 ds = 5.78 \times 10^{-13} \text{ m}^{1/3}$$

$$\text{MODEL II:} \int_{>1500 \text{ m}} C_n^2 ds = 3.05 \times 10^{-13} \text{ m}^{1/2}$$

(14)

eliminating that amount of turbulence estimated to lie below
1500 m reduces the Model I value to ~ 3.8×10^{-13} m$^{1/3}$.

Also plotted in the figure is the best fit Hufnagel aver-
age wind correlated model. The value of W selected (25 m/s) is
close to the average quoted by Hufnagel (27 m/s); however, the
data bears little resemblance to the model. The only feature
that can be associated with the model is that the empirical re-
sults undergo a dramatic change in slope in the vicinity of the
tropopause bump. It should be noted that somewhat different
quantities are being compared. Whereas the model is a mathe-
matical expression with infinitesimal altitude resolution, the
data has very rough resolution. Therefore, any conclusion drawn
from the comparison should be approached with caution. The
dashed lines are the best fit inverse cubic and inverse square
root to the data in the range from 1,000 m to 7,000 m and from
7,000 m to 20,000 m, respectively. As can be seen, the data is
fit quite well by this simple model.

A comparison between the AMOS results and several other
reported experiments is given in Figure 37. The White Sands
data[37] was taken with an instrument identical in design to the
Model II Star Sensor, whereas the Barletti data was taken with
balloon-borne microthermal probes in Europe.[36] All data has
been referred to altitude above mean sea level. The AMOS data
appears to have a much stronger dependence on altitude, being
higher at lower altitudes and lower at higher altitudes than the
other two results. Only the balloon data shows the possible
existence of a significant enhancement of turbulence in the vi-
cinity of the tropopause.

3.4.3.4 Noise Characterization Data

To provide a direct estimate of the Model II Star Sensor
noise characteristics, a series of measurements similar to those
carried out with Model I were implemented.[3] Briefly, the

100
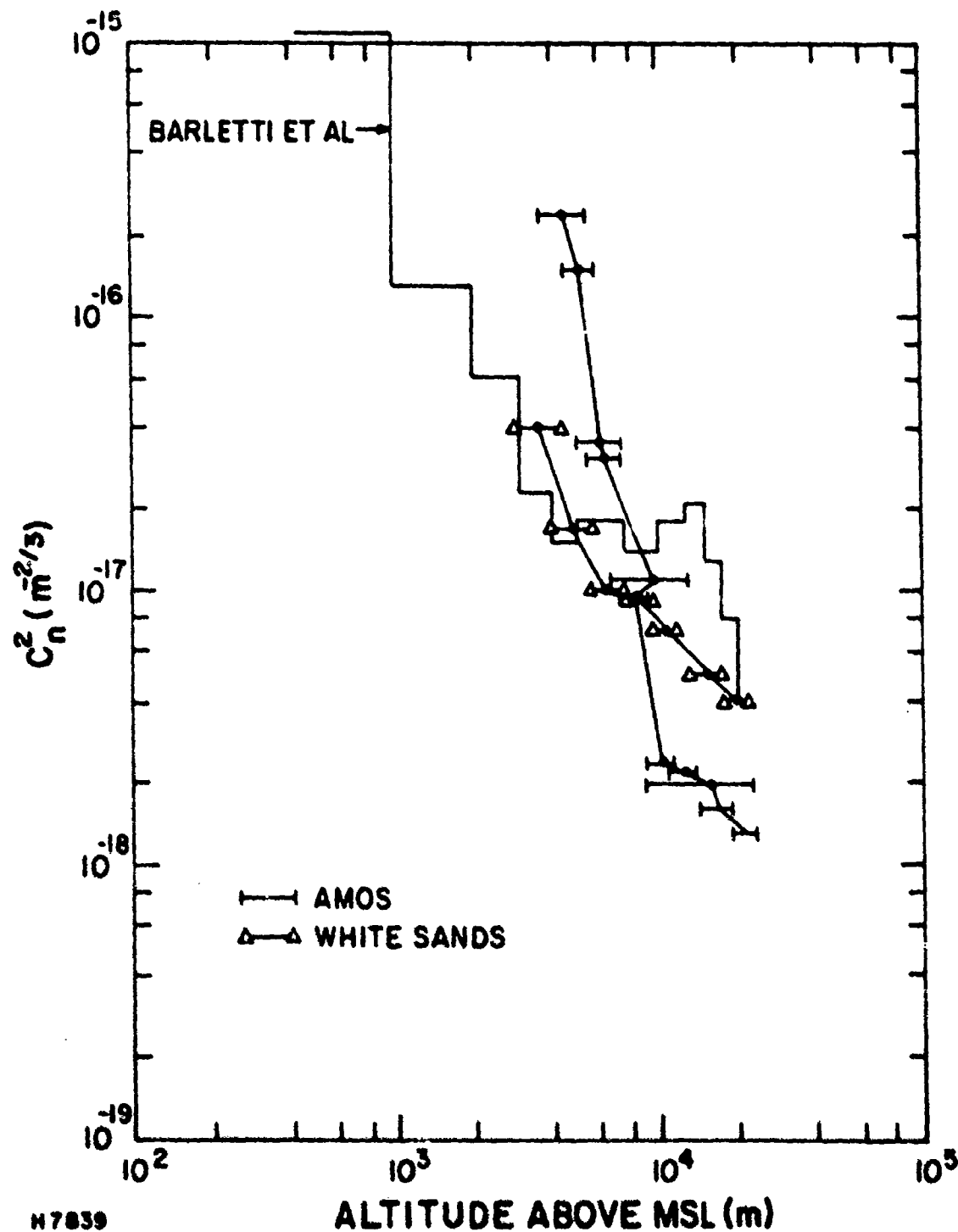
Figure 37   High Altitude Turbulent Profiles: AMOS, White Sands and Barlelli et al. Data

procedure was as follows. A low-voltage light bulb was connected to a regulated dc power supply and located such that it illuminated a portion of the diffuse, white interior surfaces of the dome. The Star Sensor telescope was pointed at the illuminated dome, the tracking motor was turned off and the mount locked in position. The instrument was operated with photomultiplier voltages and outputs typical of the range of conditions seen during stellar operations. All other lights were turned off and all personnel were excluded from the dome during periods of data collection. Data was collected on several occasions with the spatial-frequency scanning motor both on and off.

The results of one such set of measurements are shown in Figures 38 and 39. D(3) is a scaled value of the total average output of the two photomultipliers, whereas D(1) and D(2) are scaled values of the total log-amplitude standard deviation (σ_1) and the spatially filtered log-amplitude standard deviation, respectively. The filled circles and x's are motor off and on data, respectively. The numerical values indicate the applied photomultiplier voltage. The straight lines in the figures are the least squares fit to the model.

$$D^2(i) = A_j \left[D(3) \right]^{-1} + C_i; \quad i = 1, 2. \qquad (15)$$

The inverse proportionality to D(3) is consistent with an instrumental noise dominated by photoelectron fluctuations. The constant term is assumed to be a contribution due to fluctuations in the light source. This term was only significant for the lowest applied photomultiplier voltage (800 V) and the highest light levels (D(3) $\simeq$ 2000).

The empirically derived values of A as a function of applied PM voltage are shown in Figure 40. The straight lines are least squares fit to the model

$$A_i = B_i \, e^{b_i v} \qquad (16)$$

The coefficients of fit are B = (567, 1275) and b = (9.80 x 10^{-3}, 9.84 x 10^{-3}) for D(1) and D(2), respectively. When all of the appropriate scaling factors are taken into account, these results indicate that the Model II Star Sensor has somewhat lower noise than the Model I device. In most cases, the contribution of noise to the aperture-averaged log-amplitude variance is less than 10^{-4}.
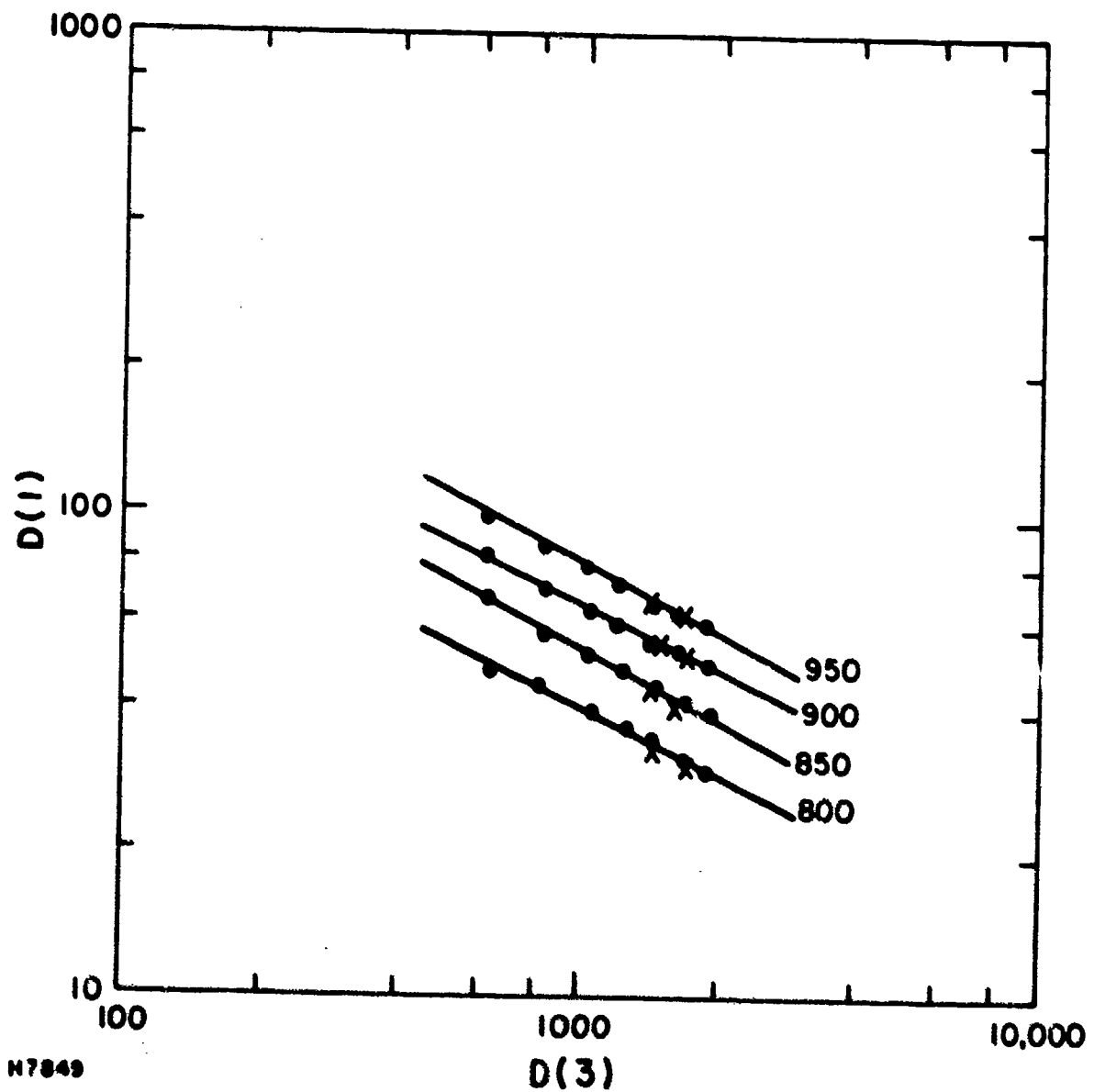
Figure 38   Sensor Noise: Total Log-Amplitude Variance, D(1) vs Average PM Output, D(3). The straight lines are inverse square root fits to the data for the indicated applied PM voltage.
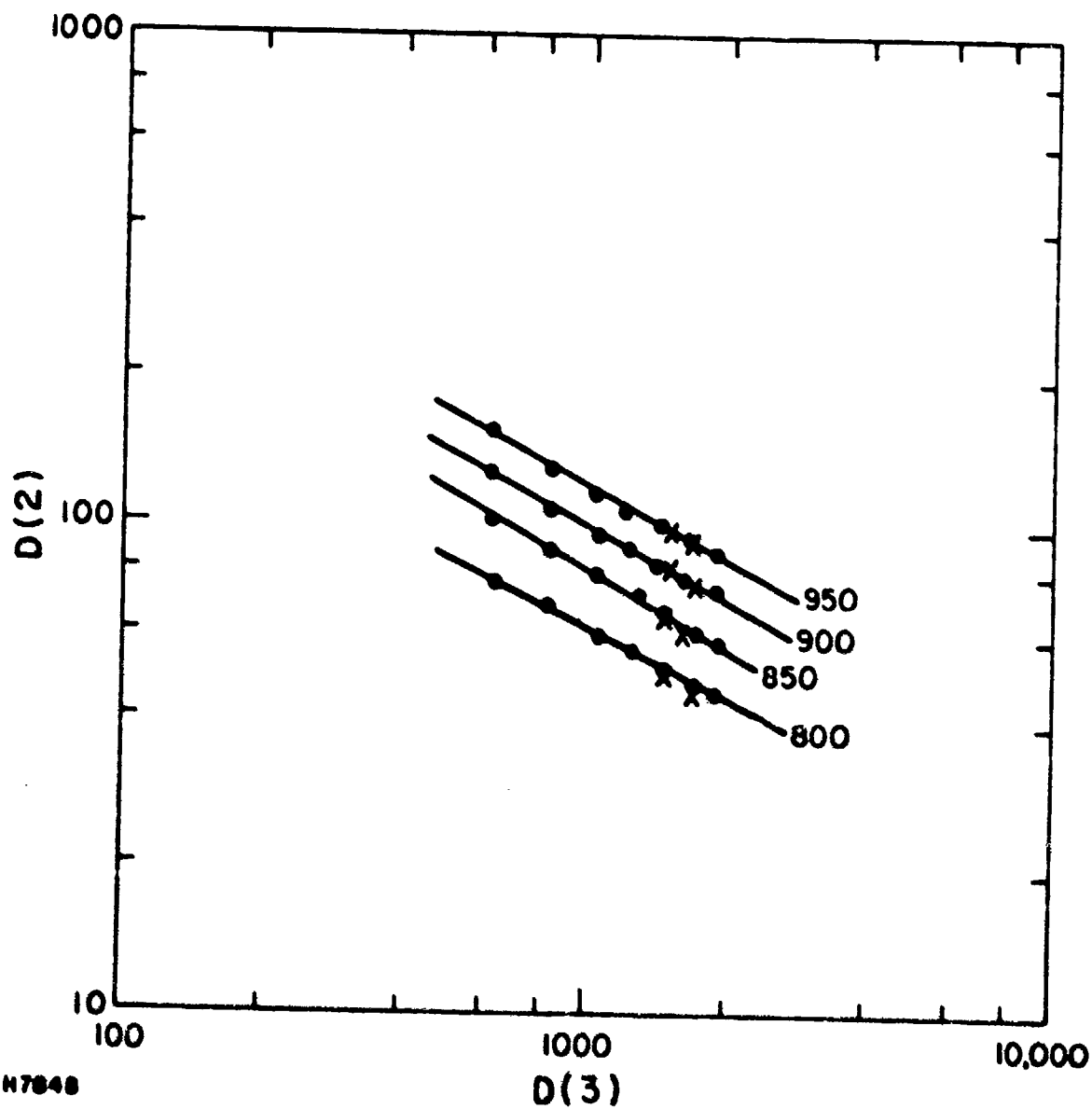
Figure 39 Star Sensor Noise: Filtered Log-Amplitude Variance, D(2) vs Average PM Output, D(3). The straight lines are inverse square root fits to the data for the indicated applied PM voltage.
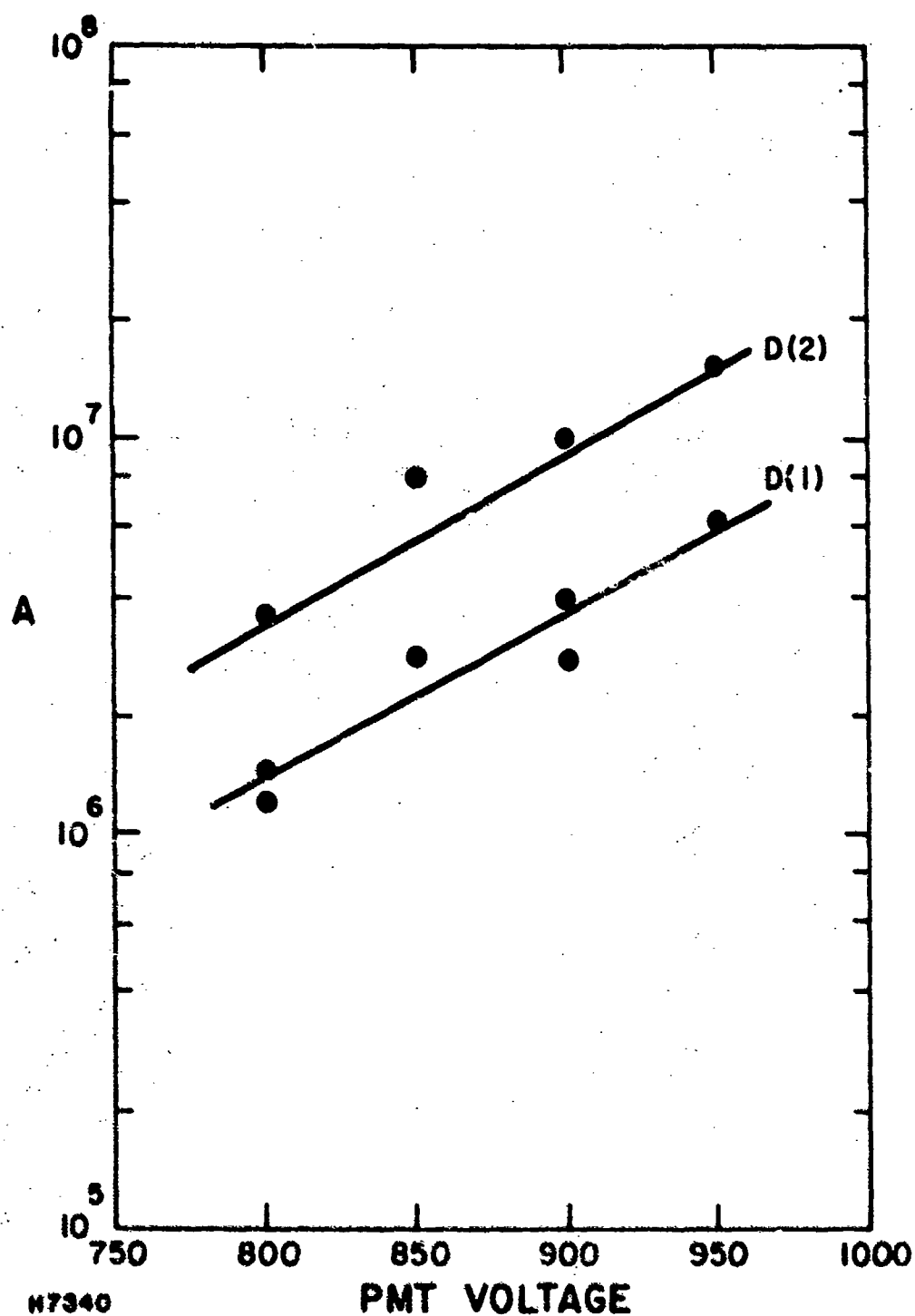
Figure 40   Star Sensor Noise vs Applied PM Voltage. The straight
lines are the best fits to an exponential model for
the total log-amplitude variance, D(1) and the filtered
log-amplitude variance, D(2).

105

A detailed comparison of the empirical model given above with the actual values of noise measured yields a maximum difference of $\pm 20\%$. The root sum square difference is closer to 10%. In contrast, a typical measured value (i.e., using the recommended calibration procedure) varies by $\sim 5\%$ (root sum square) from other values for a fixed configuration (star and voltage). Hence, only a small loss in accuracy would result if the calibration procedure[39] were to be replaced by the model. The result of implementing this procedure would be a considerable savings in set up time with only the requirement that the applied photomultiplier voltage be provided to the computer.

In addition to the above measurements, a number of "noise profiles" were _enerated. This was accomplished by allowing the instrument to collect a full cycle of data against the dc light source resulting in a full, seven level profile. While the illumination seen by the device was probably not spatially stationary it was, for the most part, temporally stationary. Therefore, variations from profile to profile should indicate the sensitivity of the data processing algorithms to noise and, hence, yield an estimate of the significance of changes in the profile from one cycle to the next. For the best noise compensation values, the profile to profile fluctuations were found to be of order 10^{-18}, 10^{-18}, 10^{-19}, 10^{-19}, 10^{-20}, 10^{-20} and 10^{-20} for the seven levels (lowest to highest), respectively. Maximum values were about a factor of 5 to 10 higher. Therefore, a somewhat conservative estimate for the required change in output to be associated with a real, physical change in turbulence conditions, would be 10^{-17}, 10^{-17}, 10^{-18}, 10^{-18}, 10^{-19}, 10^{-19} and 10^{-19}. These values are roughly 10% of the measured values of C_n^2 at each level for typical data.

39. G.R. Ochs, Ting-i Wang and P. Merron, NOAA Technical Memorandum ERL WPL-25 (April 1977).

3.4.4 Data Comparisons

3.4.4.1 General

In this section consideration is given to the comparison of optical parameters derived from empirically derived turbulence profiles with direct optical measurements. The parameter of greatest interest is the atmospheric correlation scale, r_0, as measured by the Seeing Monitor. The log-amplitude variance (σ_1^2) is not considered extensively because it primarily depends on high altitude turbulence which is measured by the Star Sensor. Previous studies[3] of the profile derived and directly measured σ_1^2 as well as comparisons of Star Sensor measurements with independent photometer data have shown good correlation. Therefore, we concentrate on the total integrated turbulence associated with propagation vertically through the atmosphere. This quantity, in turn, is related to r_0.

Three comparisons are carried out. Data taken with the ground level microthermal probes, airborne microthermal probes, Star Sensor and Seeing Monitor during November 1975 was subjected to a comparative study previously.[3] Unfortunately, this was done before the error in the Model I Star Sensor processing algorithms was discovered. Therefore, this analysis has been repeated.

During July and August 1977, a concentrated series of measurements were carried out with the ground level microthermal probes, acoustic sounder, Model II Star Sensor and Seeing Monitor. Five data sets were selected for the detailed analysis which is discussed in the third part of this section.

A considerable data base relative to both the turbulent profile and direct optical measurements now exists. In the final part of this section, this data base is used to develop an average AMOS turbulent profile which should be useful in system level studies. While the main emphasis is placed on average properties, some discussion of the statistics of the site is also included.

3.4.4.2 Reprocessed November 1975 Data

Three nights of data taken on 17, 18 and 21 November 1975 have previously been analyzed in a comparative manner.[3] These data sets were made up of ground level values of C_n^2 obtained from microthermal probes, high altitude values of C_n^2 from the Model I Star Sensor, values of C_n^2 at intermediate altitudes

obtained from an airborne microthermal probe flown by personnel from NOAA, direct measurements of the log-amplitude variance ($\sigma_1{}^2$) and the atmospheric correlation scale (r_0) obtained from the Star Sensor and Seeing Monitor, respectively. The results of this analysis yielded a profile derived value of r_0 which was considerably larger than the direct measurement.

Subsequent to the completion of the analysis, the error in the Model I Star Sensor data processing algorithms was discovered. Therefore, the analysis has been repeated using the corrected four level high altitude profile. The results are given in Table 14. The source of the various entries in the table are as follows. The experimental values of r_0 (range and average) are the direct measurements as derived from Seeing Monitor data. The profile values are obtained from an integration of the empirical profile based on ground level and airborne microthermal probes and the corrected Star Sensor data. The theory values were calculated by Yura[26] using the Hufnagel wind correlated model[33] and a low altitude turbulence profile based on the work of Bufton[40] and Koprov and Tsuang.[41] The only input to this model is the average winds aloft (W) derived from U.S. Weather Bureau meteorological data taken at stations in the Hawaiian Islands. The empirical values for this parameter are 21.3 m/s, 20.5 m/s and 30.8 m/s for 17, 18 and 21 November, respectively. Values of total integrated turbulence were obtained by inverting the standard theoretical results (Eq. (4)).

The most obvious conclusion which can be drawn from these results is that the agreement is not particularly good. The ratio of the profile to Seeing Monitor values of r_0 is ~ 1.53, 0.93 and 0.84 for 17, 18 and 21 November 1975, respectively. Only the results of 18 November are within the estimated statistical significance (~10%) of the Seeing Monitor data. While for some experiments, agreement within a factor of 1.5 is useful and has predictive capability this is not, unfortunately, the case here. The reason is that the entire Seeing Monitor data base has a range for r_0 from 0.37 to 1.80 of the mean value (9.8 cm). Hence, empirical profiles which have a prediction precision to within a multiplicative factor of 1.5 are of little utility in differentiating between conditions.

The source of the conflict between the various results is unknown. Most likely, it is due to inadequate and/or incomplete coverage of the entire optical path as well as nonstationary

40. J.L. Bufton, App. Opt. 12, 1785 (1973).

41. V.M. Koprov and L.R. Tsuang, Atmos. and Oceanic Phys. 22, 1142 (1966).

TABLE 14

REPROCESSED NOVEMBER 1975 DATA

Date	r_o (cm) @ 5000Å				$\int c_n^2\, ds$ (10^{-13} m$^{1/3}$)			
	Experimental		Prof.	Theory	Experimental		Prof.	Theory
	Range	Avg.			Range	Avg.		
17 Nov.	6.8 - 9.8	7.7	11.8	12.75	7.2 - 13.3	10.8	5.5	4.7
18 Nov.	9.7 - 13.2	11.3	10.5	13.0	4.4 - 7.4	5.7	6.5	4.5
21 Nov.	6.6 - 12.4	8.6	7.2	11.0	4.9 - 14.0	9.0	12.1	5.0

effects. While the SM and SS used the same star as a source, the airborne data, particularly at lower altitudes, was not taken directly over the observatory, but over a region on a lower portion of the mountain; therefore, the data obtained may not be representative of conditions at the observatory.

It has also been a consistent observation that atmospheric turbulence at AMOS is nonstationary both spatially and temporally. At times this effect can be large. Therefore, it is possible that unless the identical spatial and temporal optical propagation paths are used for both the profile and direct observations, the two results, while both correct, may be substantially different.

In summary, the effect of the reprocessed Model I Star Sensor data on the November 1975 comparative profile/Seeing Monitor data is to improve somewhat the consistency of the results; however, there is still a major discrepancy in the numerical values. The origin of the discrepancy is unknown, although a possible cause may be inadequate and/or inappropriate coverage of all important altitudes in the profile coupled with atmospheric nonstationarity effects.

3.4.4.3 Summer 1977 Data

During the period 21 July through 23 September 1977, atmospheric data collection operations were carried out on eighteen nights. Instrumentation used during this period included the routine meteorological sensors, microthermal probes, aco..tic sounder, Model II Star Sensor and Seeing Monitor. The reduced microthermal, Star Sensor and Seeing Monitor data were reported previously.[5] Some of the acoustic sounder data collected during this time period and subsequently reduced is given in Section 3.4.1 of this report.

Based on a careful survey of the general properties of these data, five nights of data were selected for a detailed comparative analysis. This selection was based on the existence of complete data sets from all sensors, weather conditions and subjective judgments relative to the quality of the data. Because of the time and resources required to obtain acoustic sounder results, only the data from these five nights were processed.

The reduced profile data are given in Figures 41 through 45. These results represent the average of all data of each type obtained on the indicated date. The microthermal data is denoted by solid triangles and corresponds to an altitude of 18.5 m above the local ground. Un-normalized acoustic sounder data is denoted by circles. Prior to each acoustic sounder data run, noise characterization data was collected with this instrument. This data was subsequently used to generate a noise profile. The solid circles

110

Figure 41   Average Profile for 21 July 1977. ▲ = microthermal
data; ● = Acoustic Sounder data; ○ = Acoustic Sounder
data with noise subtracted; ⊢——⊣ = Star Sensor data.
Acoustic Sounder data "n-normalized.

111

Figure 42   Average Profile for 22 July 1977. ▲ = microthermal data; ● = Acoustic Sounder data; O = Acoustic Sounder data with noise subtracted; ├──┤ = Star Sensor data. Acoustic Sounder data un-normalized.

Figure 43   Average Profile for 26 July 1977. ▲ = microthermal
data; ● = Acoustic Sounder data; O = Acoustic Sounder
data with noise subtracted; ├──┤ = Star Sensor data.
Acoustic Sounder data un-normalized.

113

Figure 44   Average Profile for 2 August 1977. **▲** = microthermal
data; **●** = Acoustic Sounder data; **O** = Acoustic Sounder
data with noise subtracted; |——| = Star Sensor data.
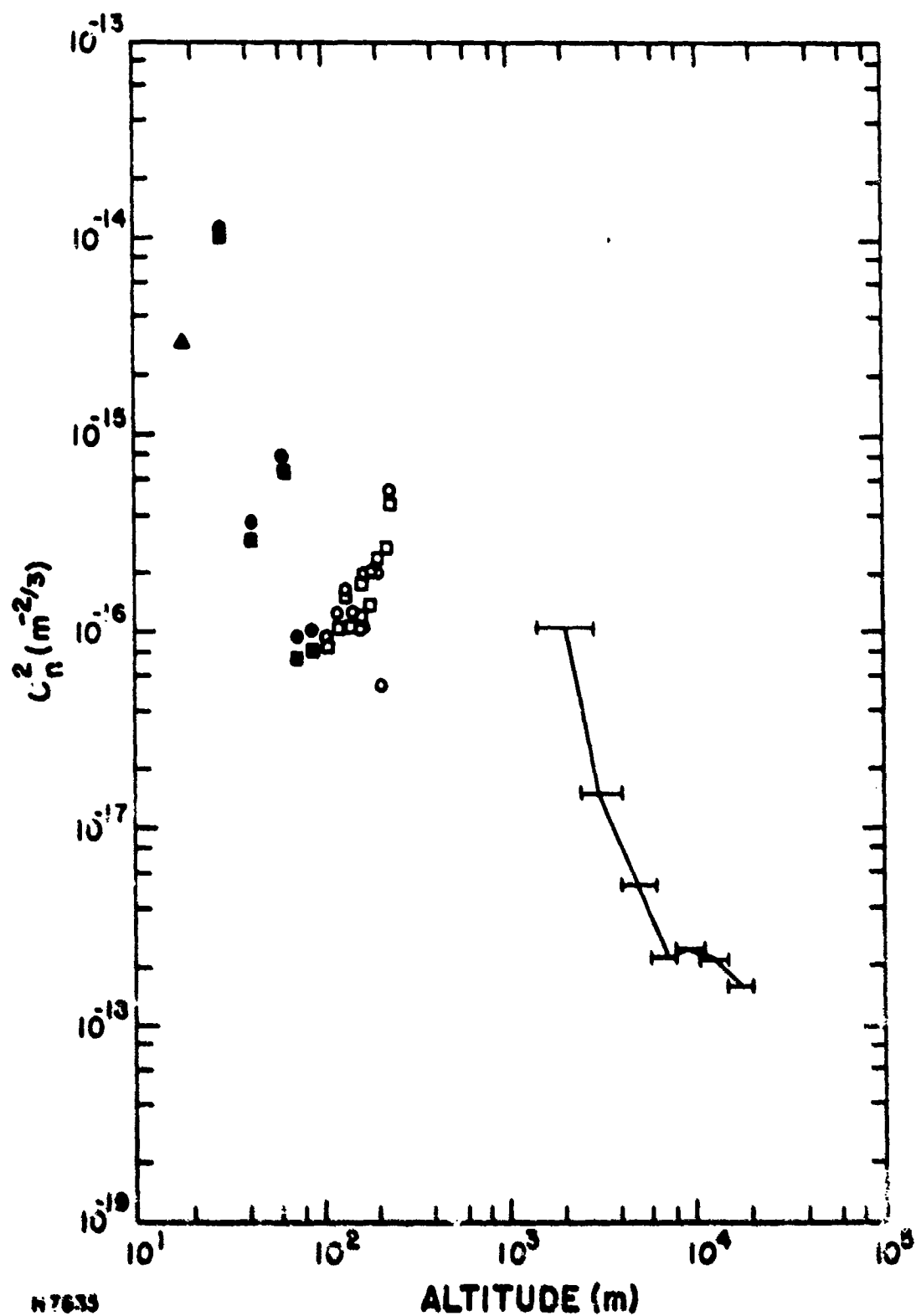Acoustic Sounder data un-normalized.

114
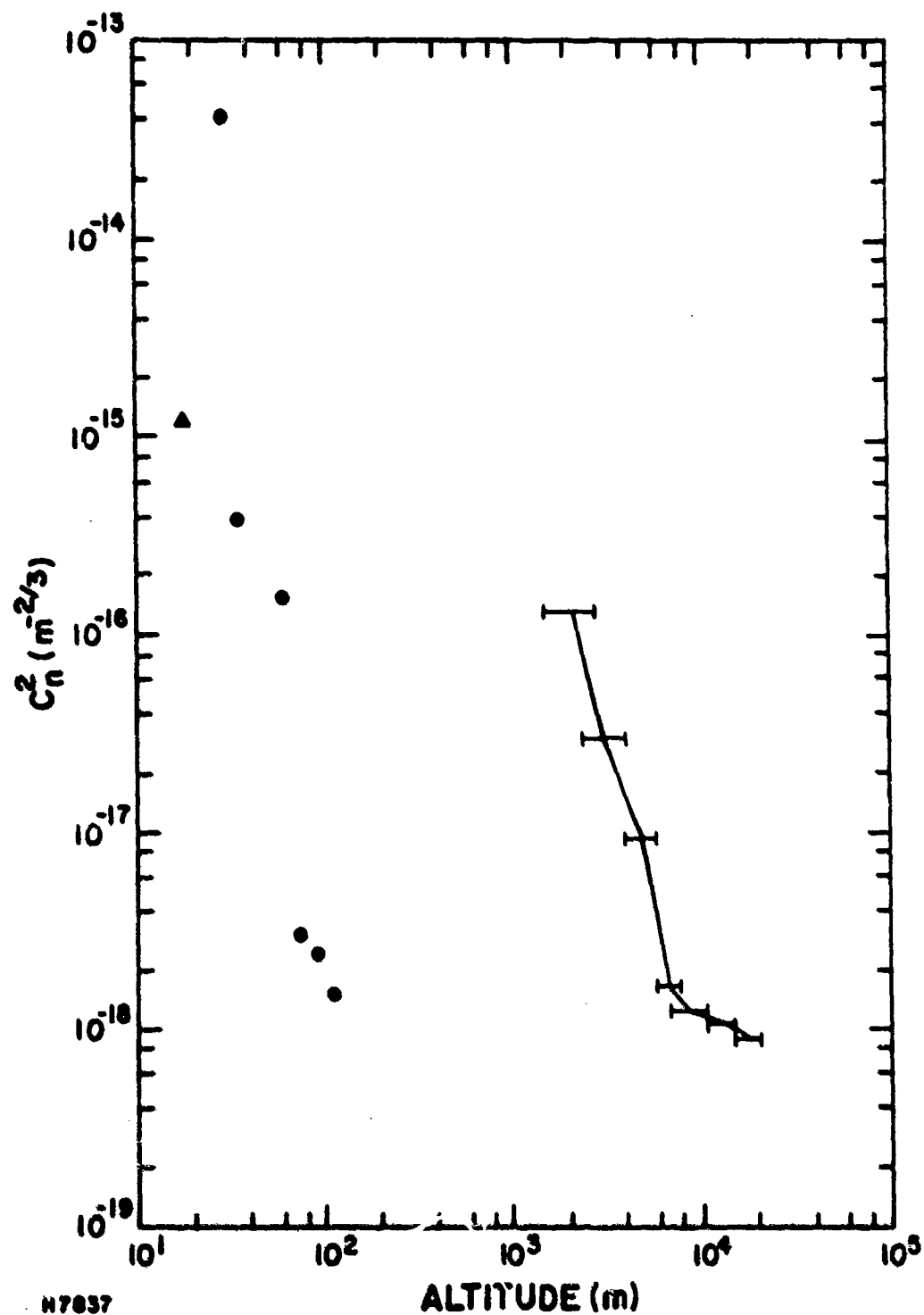
Figure 45   Average Profile for ? August 1977.   ▲ = microthermal
data; ● = Acoustic Sounder data; O = Acoustic Sounder
data with noise subtracted; ├──┤ = Star Sensor data.
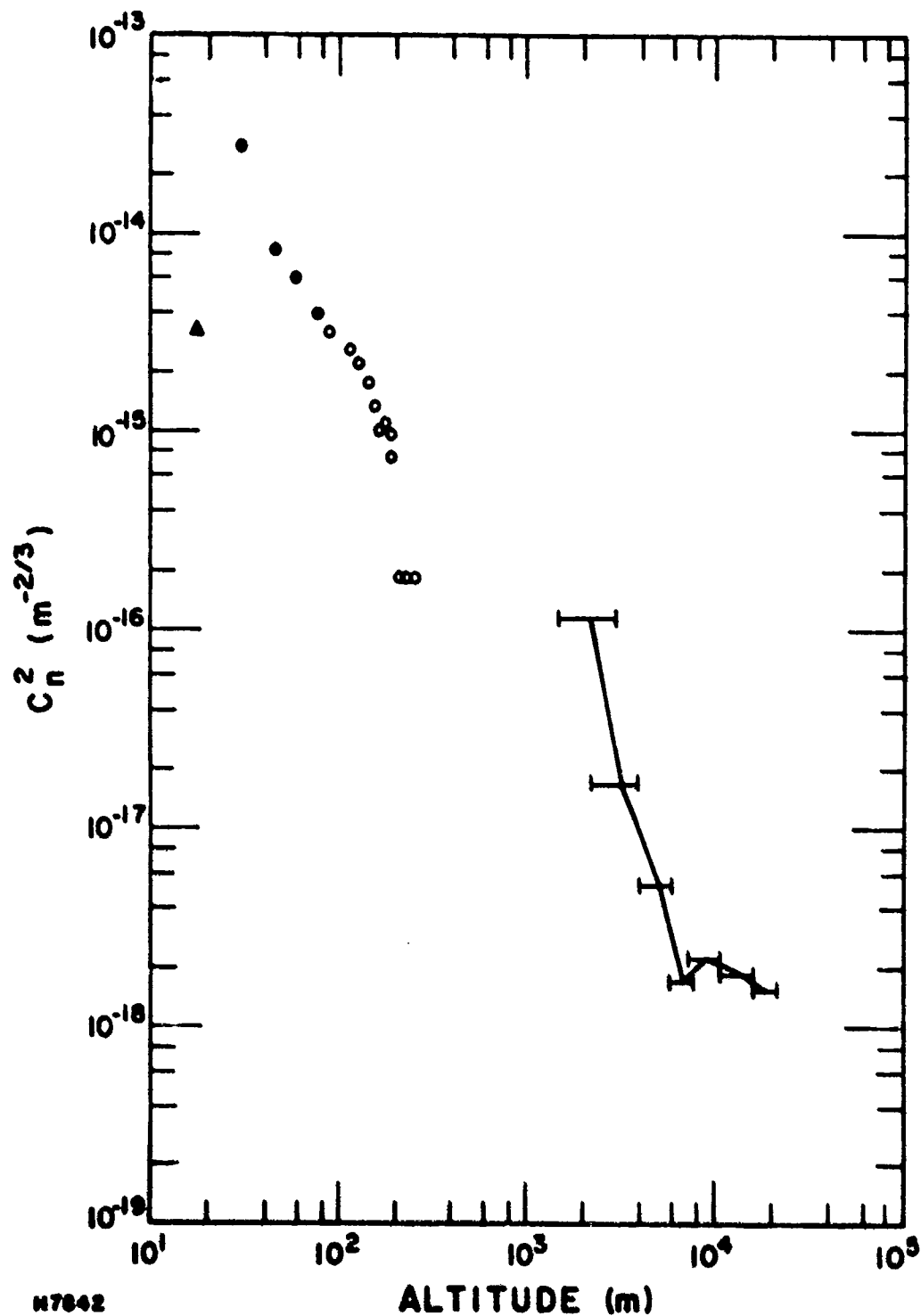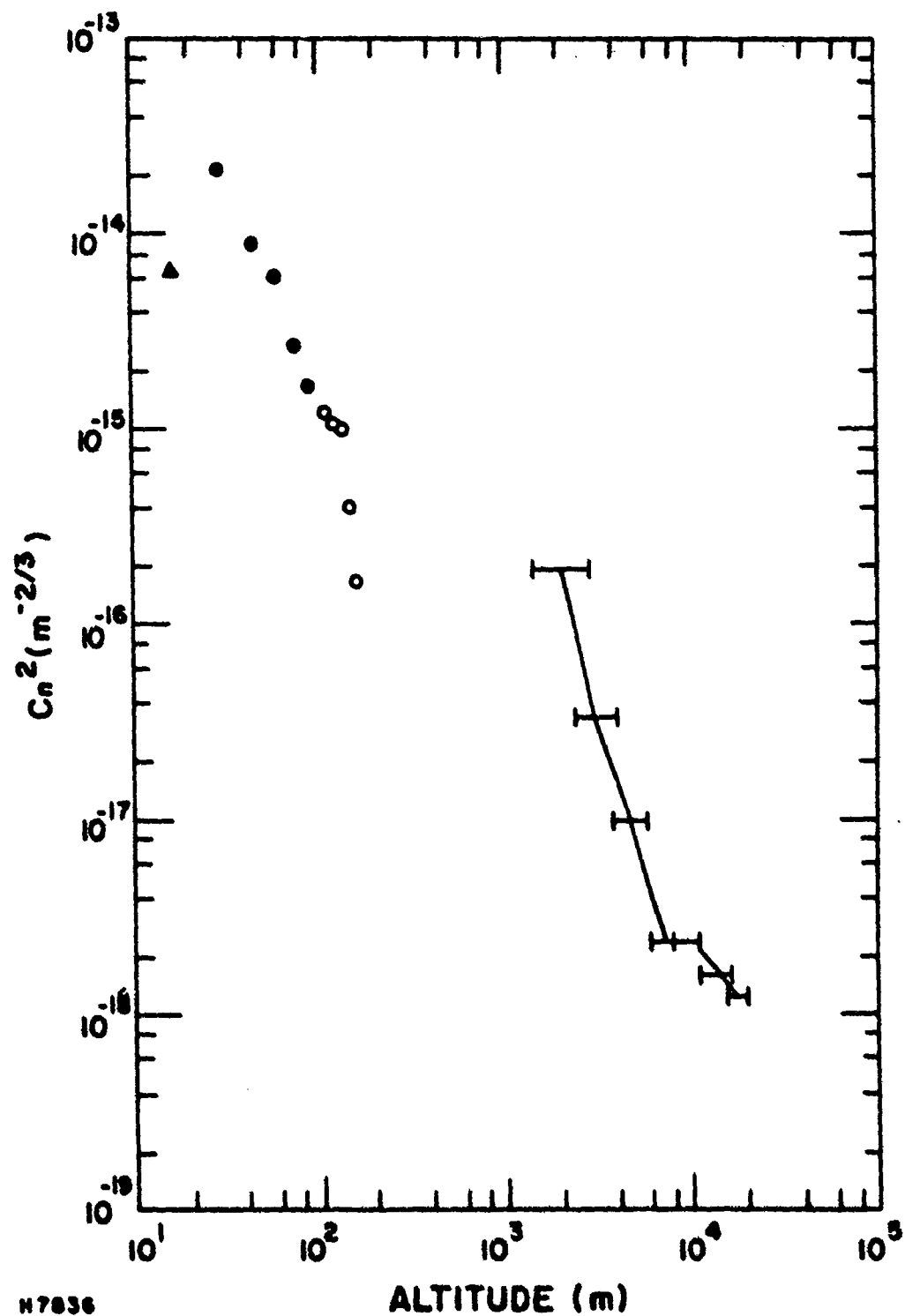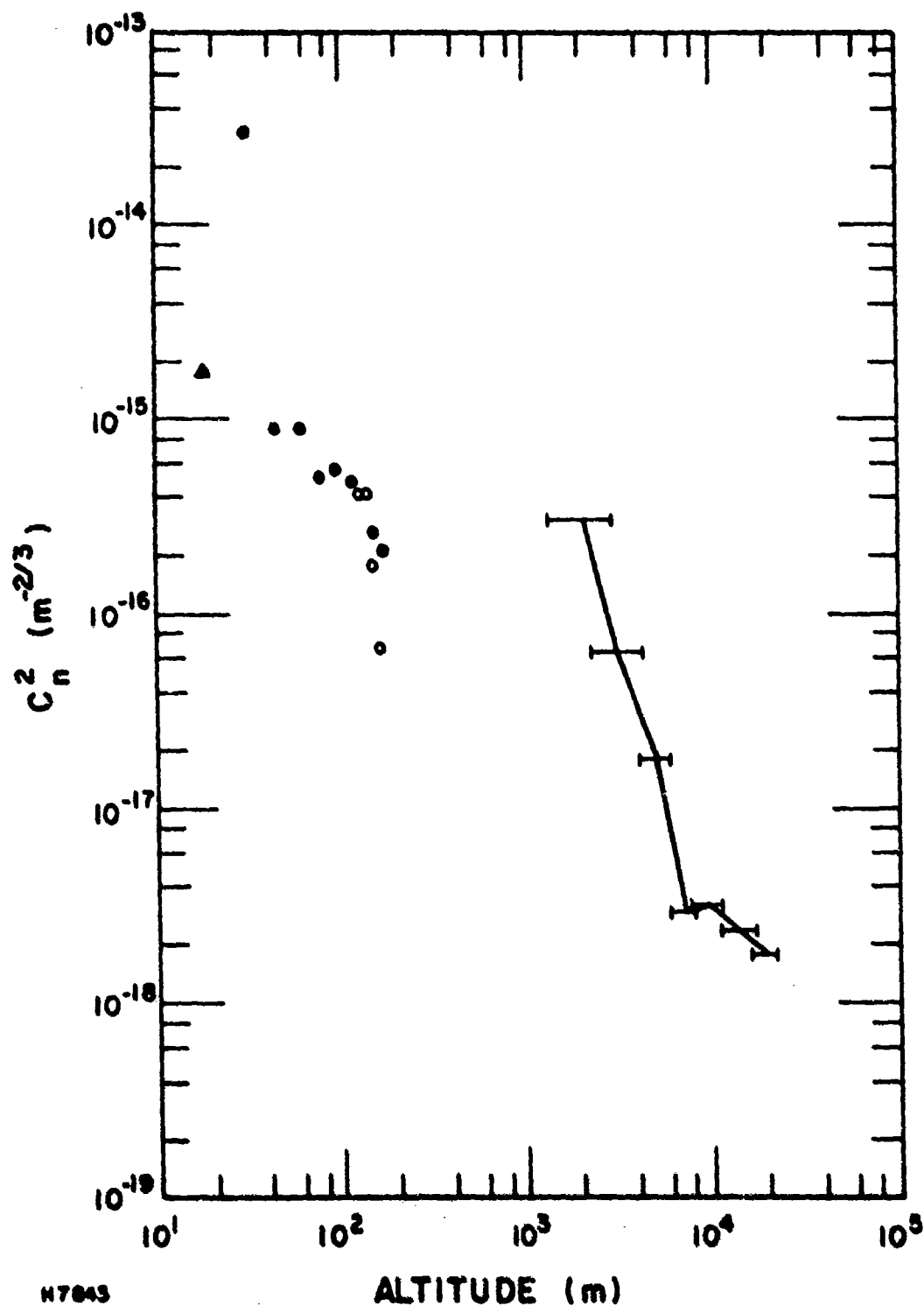Acoustic Sounder data un-normalized.

115

denote the uncorrected results whereas the open circles denote the results with the estimates of noise subtracted from the output data. For heights under ~ 100 m, the estimated contribution due to noise was not significant. The acoustic sounder, in principle, provides an estimate of C_n^2 every 15 m from 30 m to 300 m. However, above 150 to 200 m the results were so completely dominated by noise they were not included in this analysis. A second set of acoustic sounder data (squares) is shown for 21 July. These results were obtained from a second and independent reduction of the same raw data. The reason for the differences in the two results is discussed in Section 3.4.1. The average Star Sensor data is denoted by the seven bars connected by straight lines at altitudes above 1,000 m. The length of the bars indicate the width of the weighing functions associated with the reduction algorithms.

In order to compare these data with the Seeing Monitor results, the empirical profiles given in the figures were integrated to obtain estimates of the total amount of turbulence associated with each instrument. These results are given in Table 15. To generate the microthermal value, a 10 m "slab" of atmosphere was associated with the data obtained at the 18.5 m height. The acoustic sounder values correspond to a piece-wise linear fit to the data points up to about (100-150) m depending on the noise characteristics of the specific data set. The Star Sensor values were obtained using the algorithm[5] provided by NOAA which is based on the half-maximum weights of the weighing functions.

$$\int_{>1.2 \text{ km}} C_n^2 \, ds = 10^3 \left\{ \begin{array}{l} 1.4 \, C_n^2(1) + 1.7 \, C_n^2(2) + 2.0 \, C_n^2(3) \\ \\ + 2.0 \, C_n^2(4) + 3.2 \, C_n^2(5) \\ \\ + 4.5 \, Cn^2(6) + 4.0 \, C_n^2(7) \end{array} \right\} m^{1/3} \quad (17)$$

Also included in the table are the range and average values of integrated turbulence associated with the Seeing Monitor as determined by Eq. (4) (at $\lambda = 5000$ Å). The final column (Δ) shows the difference between the average Seeing Monitor results and the sum of the microthermal, unnormalized acoustic sounder and Star Sensor results. As can be seen, in four of the five cases the amount of turbulence associated with the empirical profile exceeds the average total as determined by the Seeing Monitor. In two of these four cases, the profile value also exceeds the maximum Seeing Monitor result. It is also important to note that this occurs even though no contribution for the altitude range from ~ 200 m to 1,200 m has been included.

116

TABLE 15

INTEGRATED TURBULENCE LEVELS
NIGHTLY AVERAGED DATA

Date	Micro-Thermal	Acoustic Sounder	Star Sensor	Seeing Monitor		Δ
				Range	Average	
21 July	0.3	2.0	2.1	6.9- 8.2	7.4	3.0
22 July	0.3	8.1	2.3	7.8-11.6	9.0	-1.7
26 July	0.7	7.8	3.7	6.7- 9.7	8.2	-4.0
2 Aug.	0.3	5.0	6.3	6.4- 8.3	7.1	-4.5
3 Aug.	0.1	6.2	2.8	5.8- 9.5	7.2	-1.9

All values are in units of $10^{-13} \, m^{1/3}$

The acoustic sounder results are based on unnormalized data.

117

The probable cause of the disagreement between the pro-
file and Seeing Monitor data is that the absolute calibration of
the acoustic sounder has changed due to instrument modifications
(see Section 3.4.1). This is supported by the fact that in all cases
considered (Figures 41 through 45), the lowest acoustic sounder data
point is significantly higher than the microthermal result even
though it corresponds to a higher altitude. The expectation is
that C_n^2 should decrease with altitude. Therefore, the integrated
turbulence associated with this device was reduced by a multiplica-
tive factor, α.

$$\left(\int_{AS} C_n^2 \, ds\right)_N = \alpha \left(\int_{AS} C_n^2 \, ds\right)_{UN}$$

where the value on the right hand side is the value given in
Table 15 and α was selected by least squares fitting of the lowest
acoustic sounder value to the microthermal result. The numerical
value selected in this manner is exactly an order of magnitude
$(\alpha = 0.1)$.

Table 16 is similar to Table 15 except it is based on the
normalized acoustic sounder values of integrated turbulence. In all
cases except for 2 August, the profiling instrumentation indicates
a lower value of integrated turbulence than the Seeing Monitor.
The value of Δ is just equal to that constant value of C_n^2 $(x\ 10^{-16})$
which would have to be associated with the unmeasured region ($\sim$ 200
to 1,200 m) to bring the data into exact agreement. Such values are
quite consistent with data shown here as well as with the limited
airborne microthermal data discussed elsewhere.(3) The zero value
of Δ for 2 August is a problem, but based on the range of Seeing
Monitor results for this occasion (Table 15) it is not entirely
inconsistent. Furthermore, it could be argued that the lowest
acoustic sounder point should be less than the microthermal re-
sult in view of the 12.5 m height difference between the two
measurements. This would result in an increase in the value of
Δ for all cases.

In summary, the five nightly averaged data sets analyzed
here indicate that when the acoustic sounder data is normalized
to the microthermal data, the resulting profile is consistent
with the Seeing Monitor results. Furthermore, the amount of in-
tegrated turbulence which must be associated with the unmeasured
region ($\sim$ 200 m to 1,200 m) is certainly reasonable based on
limited data relative to this region and the general levels seen
above and below this region.

118

TABLE 16

MODIFIED INTEGRATED TURBULENCE
LEVELS NIGHTLY AVERAGED DATA

Date	Micro-thermal	Normalized Acoustic Sounder	Star Sensor	Seeing Monitor	Δ
21 July	0.3	0.2	2.1	7.4	4.8
22 July	0.3	0.8	2.3	9.0	5.6
26 July	0.7	0.8	3.7	8.2	3.0
2 Aug.	0.3	0.5	6.3	7.1	0.0
3 Aug.	0.1	0.6	2.8	7.2	3.7

All values are in units of $10^{-13} \, m^{1/3}$

Finally, the results indicate that only (7-18) % of the
total integrated turbulence is associated with altitudes below
200 m, whereas (26-89) % is associated with altitudes above
1.2 km. This leads to the conclusion that a substantial and
variable amount of integrated turbulence is to be found at in-
termediate altitudes (200 - 1,200 m). Hence, without direct
measurements of the strength of turbulence in this region, it
is unlikely that the empirical profiles will agree with Seeing
Monitor data with reasonable precision and regularity.

3.4.4.4 Average Turbulent Profile

A considerable data base now exists covering both high
and low level turbulence structure as well as direct optical
parameters. Based on this data it is possible to construct
an average profile for AMOS. This profile is based on the
following data and properties.

At high altitudes, the Star Sensor data summarized in
Figure 36 indicates two different characteristic regimes. At
altitudes from $\sim$ 1,500 m to 7,000 m the data is well matched
by an inverse cubic, whereas above 7,000 m the data follows
an inverse square root law. Obviously, this latter dependence
cannot be extended to arbitrarily high altitudes because integral
properties of the profile will not converge. Therefore, a high
altitude cutoff is required. This was done by requiring the
model and data to have the same numerical value of integrated
turbulence above 7 km. This model is a rather arbitrary choice.
For example, an exponential dependence would work equally well.
However, because nothing is known experimentally about the ex-
tremely high altitudes (except that C_n^2 must be very small), the
inverse square root coupled with a cutoff is somewhat more con-
venient for carrying out the various calculations of interest.

The microthermal data taken at the 18.5 m height above local
ground has an average value of $\sim$ 8.4 x 10^{-15} m$^{-2/3}$ (Table 3). As
discussed in Section 3.4.1, the acoustic sounder data has an
average slope of h-2.

At intermediate altitudes (200 - 1,500 m), very little data
exists. Three nights of results[3] taken with an airborne micro-
thermal probe indicates values for C_n^2 of order 10^{-16} m$^{-2/3}$; how-
ver, there is considerable scatter in the data. Therefore, lacking
further information, a constant value which is consistent with the
acoustic sounder, Star Sensor and limited airborne microthermal
data will be assumed.

The resulting average profile is:

$$
C_n{}^2(h) = \begin{cases}
8.4 \times 10^{-15}\ (h/18.5)^{-2} & ;\ 18.5\ m \le h \le 110m \\[1ex]
2.5 \times 10^{-16} & ;\ 110\ m \le h \le 1500\ m \\[1ex]
8.87 \times 10^{-16}\ (h/1000)^{-3} & ;\ 1500\ m \le h \le 7000\ m \\[1ex]
6.34 \times 10^{-18}\ (h/1000)^{-1/2}; & 7000\ m \le h \le 20500\ m \\[1ex]
0 & ;\ 20500\ m \le h
\end{cases} \ m^{-2/3}
$$

$$\tag{19}$$

where h is the altitude above the site in meters which is $\sim$ 3 km above mean sea level. This profile is shown graphically in Figure 46.

Integral properties of this profile are given in Tables 17 and 18. The optical parameters associated with these integral properties are also included. The definition of these parameters is as follows:

$$
r_o = [0.42\ (2\pi/\lambda)^2 \int C_n{}^2(h)\ dh]^{-3/5} \tag{20}
$$

$$
\sigma_1{}^2(pt) = 0.56\ (2\pi/\lambda)^{7/6} \int C_n{}^2(h)\ h^{5/6}\ dh \tag{21}
$$

$$
\sigma_1{}^2(36\ cm) = 0.019\ \sigma_1{}^2(pt) \tag{22}
$$

$$
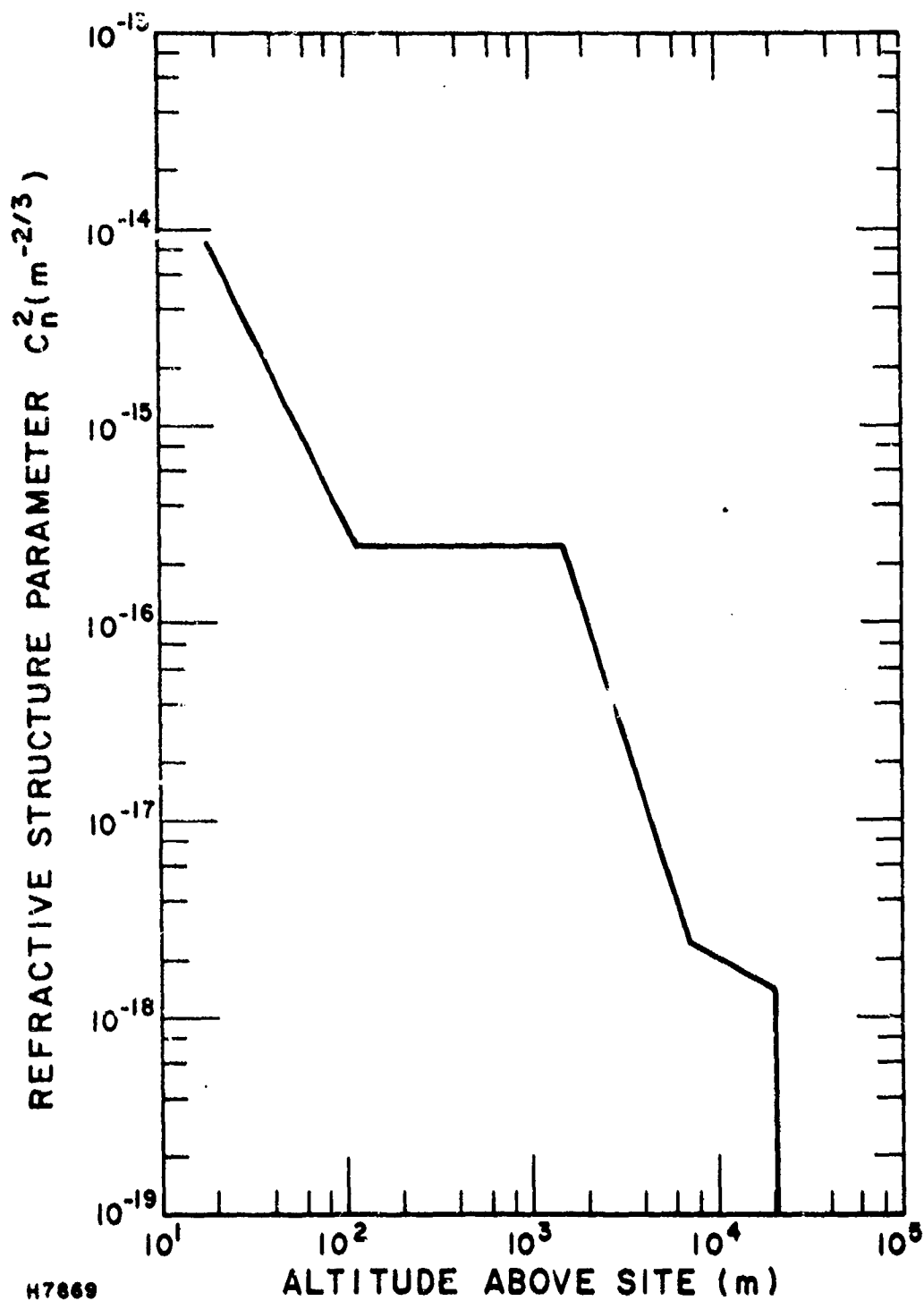\theta_c = [0.42\ (2\pi/\lambda)^2 \int C_n{}^2(h)\ h^{5/3}\ dh]^{-3/5} \tag{23}
$$

121

Figure 46   Average AMOS Turbulent Profile.   Based on microthermal, Acoustic Sounder and Star Sensor data.

For the calculations of Tables 17 and 18, a wavelength (λ) of 0.5 μ was assumed. r_0 is the atmospheric correlation scale for propagation from a star to the ground,[14] whereas σ_1^2(pt) is the log-amplitude variance (scintillation) associated with a point detector on the ground viewing a stellar point object.[9] σ_1^2 (36 cm) is the log-amplitude variance appropriate to a detector with a 36 cm entrance aperture. Hence, it is this value that is appropriate for the Star Sensor. The aperture averaging factor, 0.019, was calculated from theory by Yura.[26] The final parameter, θ_c, is just the ratio of the atmospheric correlation scale (r_0) to altitude (h) for propagation from a point source on the gound to an observation plane above the atmosphere[27] (> 25 km in this case). As such, this parameter controls the resolution for downward looking optical systems and also characterizes the scale of nonisoplanatic effects for many systems. While the details of the latter effect are technique dependent, θ_c (or some scaled version) often appears as an asymptotic limit. For example, Shapiro[28] defines a critical angle, θ_p, associated with reciprocity tracking while Fried[29] defines an angle, θ_0, associated with realtime atmospheric compensation. Both of these angles are just scaled versions of θ_c given by

$$\theta_p \text{ (Shapiro)} = (3.44)^{-3/5} \theta_c = 4.06 \text{ arcsec} \tag{24}$$

$$\theta_0 \text{ (Fried)} = (6.88)^{-3/5} \theta_c = 2.68 \text{ arcsec} \tag{25}$$

Experimentally, data relative to all three of these parameters have been obtained at AMOS. The extensive Seeing Monitor data has an average r_0 value of 9.8 cm at 0.5 μ, whereas Star Sensor data has an average log-amplitude (aperture averaged) variance of 5.8×10^{-4}. Hence, the average profile of Figure 46 agrees quite well with direct measurements. A limited amount of data relative to nonisoplanatism effects in Speckle Interferometry have been obtained at AMOS.[24,35] Theory[25] predicts that the fringe modulation of a binary star transform (measured quantity) should drop to ~ 10% of its isoplanatic value at an angular separation of $\theta_c/2$). The experimental results indicate a significant effect on the scale of a few arcseconds. Therefore, the average profile is also consistent with these, somewhat limited, experimental results.

It is also of interest to generate numerical profiles associated with the range seen in the data. Only the Star Sensor and ground level microthermal probes have produced sufficient data to make such an estimate meaningful. Results for the Model I Star

TABLE 17

AVERAGE PROFILE - INTEGRAL PROPERTIES

$\int c_n^2$ (h) dh: $\qquad$ 6.9×10^{-13} $m^{1/3}$

r_o $\qquad$ 10 cm

$\int c_n^2$ (h) $h^{5/6}$ dh: $\qquad$ 2.8×10^{-10} $m^{7/6}$

σ_1^2 (pt) $\qquad$ 0.030

σ_1^2 (36 cm) $\qquad$ 5.7×10^{-4}

$\int c_n^2$ (h) $h^{5/3}$ dh: $\qquad$ 3.1×10^{-7} m^2

θ_c $\qquad$ 8.5 arcsec

TABLE 18

**INTEGRATED TURBULENCE IN
VARIOUS ALTITUDE REGIONS**

Altitude (m)	$\int c_n^2\, dh\ (m^{1/3})$		$\int c_n^2\, h^{5/6}\, dh\ (m^{7/6})$		$\int c_n^2\, h^{5/3}\, dh\ (m^2)$	
	Value	%	Value	%	Value	%
185-110	1.29×10^{-13}	19	2.73×10^{-12}	1	6.88×10^{-11}	<1
110-1500	3.48×10^{-13}	51	8.99×10^{-11}	32	2.76×10^{-8}	9
1500-7000	1.88×10^{-13}	27	1.25×10^{-10}	44	9.34×10^{-8}	31
7000-25000	0.24×10^{-13}	3	6.42×10^{-11}	23	1.84×10^{-7}	60
Total	6.89×10^{-13}	100	2.82×10^{-10}	100	3.05×10^{-7}	100

Sensor are given in Table 12, whereas the ground level data ranges from 4 x 10-16 m-2/3 to 10^{-13} m-2/3 (Table 3). Because of the unavailability of sufficient data in the important intermediate range of altitude, it seems advisable to simply scale the entire profile of Figure 46 up or down by a single numerical value to obtain the desired results. Also of use in establishing these estimates are the r_o (Seeing Monitor) and σ_1^2 (Star Sensor) data. Consideration of these various results yields the numerical scaling factors, integral properties and optical parameters given in Table 19. Also included are the direct measurements of r_o and σ_1^2 (36 cm). It should be emphasized that these scaling factors are rather subjective in nature and are mainly included to demonstrate that a consistent, quasi-empirical profile appropriate to AMOS can be defined.

TABLE 19

VARIATIONS OF AMOS PROFILES

Quantity	Maximum Scaling	Data	Minimum Scaling	Data	Mean + One Std. Deviation Scaling	Data
Factor	5.1	-	0.32	-	1.7	-
$\int C_n^2 \, dh \ (\times 19^{-13} \ m^{1/3})$	35.1	-	2.20	-	11.7	-
r_o (cm)	3.8	3.6	20.0	17.8	7.3	7.6
$\int C_n^2 \, h^{5/6} (\times 10^{-10} m^{7/6})$	14.4	-	0.90	-	4.79	-
σ_1^2 (pt)	0.15	-	0.010	-	0.051	-
σ_1^2 (36 cm) $(\times 10^{-4})$	29.4	28.0	1.83	1.6	9.77	10.2
$\int C_n^2 \, h^{5/3} \, dh \ (10^{-7} \ m^2)$	15.6	-	0.976	-	5.18	-
θ_c (arcsec)	3.2	-	16.9	-	6.2	-

127

3.4.5 RTAM Data Processing

Shortly after the delivery and acceptance of the Real Time Atmospheric Measurement (RTAM) System, a brief series of simultaneous operations with this device and the Seeing Monitor were carried out.[5] The objective of these measurements was to obtain two simultaneous and independent estimates of the atmospheric correlation scale (r_o).

The experimental setup was as follows. The SM and RTAM were both mounted on the rear blanchard surface of the 1.6 m telescope. Auxiliary optics and a cube beam splitter were used to direct 28% of the light to the SM and 64% to the RTAM. SM data was processed in realtime using the PDP-8 data processing system. RTAM raw data was recorded on magnetic tape for processing off-line. In total, 10 data runs, each $\sim$ 15 min in length, were obtained on two nights using the brightest stars available as objects.

Processing of the RTAM data was accomplished using the electronics previously described.[4] Very briefly, these electronics accept the RTAM MTF output and determine the half-maximum width of the MTF on a realization by realization basis. Because the data rides on a noise pedestal, a background subtracting algorithm was required. The output of the processing electronics is a voltage proportional to the half MTF spatial frequency which is compatible with the PDP-8 processing system.

Of all data collected, only a single run was suitable for processing. The reason for this is the low sensitivity of the RTAM which yields excessive amounts of noise unless very bright stars are used. This single run was taken against Sirius (m = 1.4) on 17 February 1977 using the minimum electrical bandwidth of the RTAM. The spectral bandwidth of the measurement was determined by the extended red, S-20 response ($\lambda_c \simeq 5000 \text{Å}$) of the photomultiplier cathode. Scope traces of the MTF were similar to those displayed elsewhere (Figure 27 of Ref. 4).

During the 15-min time duration of this run, four estimates of r_o were obtained with the SM. A 5,000 point sample size corresponding to a 3 min averaging time was used. The average r_o for the period was 11.5 cm. The results indicate that seeing was reasonably constant during the period and, hence, the above value is probably accurate to within 10%.

The RTAM data (single channel) was also processed with 5,000 samples per average; however, because of a different configuration of the inputs to the PDP-8, the averaging time was $\sim$ 1 min.

128

Thirteen 1 min average voltages were obtained which had a maximum variation of ±4%, confirming that seeing conditions were resonably constant during the 15-min period of the data run.

Several issues must be addressed before an estimate of r_o can be obtained from RTAM data. The first of these is the absolute instrumental calibration of the RTAM MTF output. Because of some confusion as to the detailed optical configuration of the instrument, imprecise knowledge of several parameters, and the broadband nature of the photocathode response, it is difficult to determine a reliable and accurate estimate of the sweep time which corresponds to the diffraction limit of the telescope. This quantity is necessary to establish the absolute value of the spatial frequency at which the MTF falls to one half of its initial (frequency = 0) value; however, it is possible because of the nature of the output to obtain this estimate by looking at the MTF on an oscilloscope. The calibration used was that determined by the latter method. It should be noted that the former method was also carried out and yielded reasonably consistent results considering the difficulties noted above.

A second issue is the broadening of the MTF by the finite electronic bandwidth of the device. While a high bandwidth which would minimize this effect was available, it could not be used because of the increased noise it created. Measurements of the width of an input pulse as a function of bandwidth were carried out during the laboratory testing of the RTAM.[42] Unfortunately, the output MTF shape is not simple and hence, a deconvolution to obtain the atmospheric MTF is not straight-forward. Using several different ideal shapes yields an atmospheric width which varies by ~ ±8% around a nominal value.

Combining these two effects and several less important ones leads to the conclusion that the average half MTF normalized (relative to the diffraction limit) spatial frequency derived from RTAM data is:

$$q \text{ (nominal)} = 0.0376$$
$$q \text{ (maximum)} = 0.0429 \ (+14\%) \quad\quad (26)$$
$$q \text{ (minimum)} = 0.0320 \ (-15\%)$$

The desired estimate of r_o is obtained by fitting these values to the short-exposure average MTF.[14]

----

42. A.J. MacGovern, private communication.

$$\langle \tau(q) \rangle_{s\dot{e}} = \tau_0(q) \exp\left[-3.44(\alpha q)^{5/3}(1 - q^{1/3})\right] \qquad (27)$$

where α is the ratio of telescope diameter to r_0 and $\tau_0(q)$ is the telescope transfer function. It should be noted that as in the case of the Seeing Monitor, the instrumental technique implemented is not effected by image wander. Hence, the short exposure as opposed to the long exposure average is the appropriate model. However, the processing in both devices does not correspond exactly to the model because the half MTF frequency is determined first and then averaged, in contrast to averaging the MTF first and then determining the half MTF frequency. As had been discussed previously, [3] this difference should not lead to a very large error. In any case, it has no impact on the relative results because the processing associated with the two devices is equivalent.

Assuming a diffraction limited clear aperture of 1.6 m (as is done for the SM) yields the following values of r_0 from the RTAM:

$$r_0 \text{ (nominal)} = 12.6 \text{ cm}$$
$$r_0 \text{ (maximum)} = 14.3 \text{ cm} \qquad (28)$$
$$r_0 \text{ (minimum)} = 10.8 \text{ cm}$$

Comparing these results with the SM result show that the nominal values are within 10% and that there exist a considerable region of overlap within the error bars of the two measurements. Hence, we conclude that the RTAM data confirms the SM measurement, at least for the small data sample considered here.

REFERENCES

1. M.G. Miller and P.F. Kellen, Turbulence Characterization and Control, Interim Technical Report, Contract F30602-75-C-0012 (Avco Everett Research Laboratory, Inc.), Rome Air Development Center Technical Report #RADC-TR-75-185 (July 1975). (A015759)

2. M.G. Miller, P.L. Zieske and G.L. Dryden, Turbulence Characterization and Control, Final Technical Report, Contract F30602-75-C-0012 (Avco Everett Research Laboratory Laboratory, Inc.), Rome Air Development Center Technical Report #RADC-TR-76-189 (June 1976). (A027155)

3. M.G. Miller and P.L. Zieske, Turbulence Environment Characterization, Interim Technical Report, Contract F30602-76-C-0054 (Avco Everett Research Laboratory, Inc.), Rome Air Development Center Technical Report #RADC-TR-77-70 (March 1977). (A038632)

4. M.G. Miller, P.L. Zieske, A.J. Sofia and R.J. Pepe, Turbulence Environment Characterization, Interim Technical Report, Contract F30602-76-C-0054 (Avco Everett Research Laboratory, Inc.), Rome Air Development Center Technical Report #RADC-TR-77-232 (July 1977). (A052994)

5. M.G. Miller and P.L. Zieske, Turbulence Environment Characterization, Interim Technical Report, Contract F30602-76-C-0054 (Avco Everett Research Laboratory, Inc.), Rome Air Development Center Technical Report #RADC-TR-78-72 (April 1978). (A054951)

6. D.P. Greenwood, D.O. Tarazano, D.A. Haugen, J.C. Kaimal, J. Newman, P.F. Kellen and M.G. Miller, AMOS Seeing Quality Measurements, Rome Air Development Center In-House Technical Report #RADC-TR-75-295 (January 1976). (A021943)

7. M.G. Miller and P.F. Kellen, Proceedings of the AAS/SAO/OSA/SPIE Topical Meeting on Imaging in Astronomy, Cambridge, Mass. (1975), Paper WB-3.

8. D.P. Greenwood and D.B. Youmans, A Fine Wire Microthermal Probe for Atmospheric Measurements, Rome Air Development Center Technical Report #RADC-TR-75-240 (December 1975). (A019277)

9. R. Lawrence and J. Strohbehn, Proc. IEEE 58, 1523 (1970).

10. R.S. Lawrence, G.R. Ochs and S.F. Clifford, J. Opt. Soc. Am. 60, 826 (1971).

11. F.F. Hall in, Temperature and Wind Structure Studies by Acoustic Echo Sounding, ed. by V.E. Derr, U.S. Government Printing Office 0322-0011 (1972).

12. G.R. Ochs, Ting-i Wang, R.S. Lawrence and S.F. Clifford, App. Opt. 15, 2504 (1976).

13. C.R. Giuliano, et al., Space Object Imaging, Final Report, Contract F30602-74-C-0227 (Hughes Research Laboratory), Rome Air Development Center Technical Report #RADC-TR-76-54 (March 1976). A023497

14. D.L. Fried, J. Opt. Soc. Am. 56, 1372 (1966). Related results are given in R.E. Hufnagel and N.R. Stanley, J. Opt. Soc. Am. 54, 52 (1964).

15. A.M. Schneiderman and D.P. Karo, Opt. Eng. 16, 72 (1977). The Speckle Interferometer work was funded by other sources.

16. A.J. MacGovern, Real Time Atmospheric Monitor, Final Report, Contract F30602-74-C-0147 (Itek Corporation), Rome Air Development Center Report #RADC-TR-78-80 (April 1978). A054142

17. D.P. Karo and A.M. Schneiderman, J. Opt. Soc. Am. 66, 1252 (1976).

18. D. Korff, J. Opt. Soc. Am. 63, 971 (1973).

19. D.P. Karo and A.M. Schneiderman, J. Opt. Soc. Am. 67, 1583 (1977).

20. D. Korff, G.L. Dryden and M.G. Miller, Opt. Comm. 5, 187 (1972).

21. M.G. Miller and P.L. Zieske, J. Opt. Soc. Am. 67, 1680 (1977).

22. Section 3 of this report.

23. A.M. Schneiderman and D.P. Karo, J. Opt. Soc. Am. 68, 480 (1978).

24. A.M. Schneiderman and D.P. Karo, J. Opt. Soc. Am. 68, 338 (1978).

25. D. Korff, G. Dryden and R. Leavitt, J. Opt. Soc. Am. 65, 1321 (1975).

26. H. Yura, Aerospace Corporation Technical Report #TR-0077 (2756)-1 (1976).

27. D.L. Fried, J. Opt. Soc. Am. 56, 1380 (1966).

28. J.H. Shapiro, J. Opt. Soc. Am. 65, 65 (1975).

29. D.L. Fried, The Optical Sciences Company Report #TR-249 (March 1977).

30. J.C. Dainty and R.J. Scadden, Mon. Not. R. Astr. Soc. 170, 519 (1975).

31. D.L. Fried and G.E. Mevers, App. Opt. 13, 2620 (1974); ibid., 14, 2567 (1975); ibid., 16, 549 (1977).

32. D.L. Walters, J. Opt. Soc. Am. 67, 1377A (1977); ibid., 68, 1368A (1978).

33. R.E. Hufnagel, OSA Topical Meeting on Optical Propagation Through Turbulence, Boulder, Colorado (1974), paper WA-1.

34. P. Nisenson and R.V. Stachnik, J. Opt. Soc. Am. 68, 169 (1978).

35. S. Pollaine, Lawrence Berkley Lab., private communication.

36. R. Barletti, et al., J. Opt. Soc. Am. 66, 1380 (1976).

37. C. Hogge, Air Force Weapons Lab., private communication.

38. R. Lawrence, NOAA Environmental Research Lab., private communication.

39. G.R. Ochs, Ting-i Wang and F. Merren, NOAA Technical Memorandum ERL WPL-25 (April 1977).

40. J.L. Bufton, App. Opt. 12, 1785 (1973).

41. V.M. Koprov and L.R. Tsuang, Atmos. and Oceanic Phys. 22, 1142 (1966).

42. A.J. MacGovern, private communication.

MISSION
of
Rome Air Development Center

RADC plans and executes research, development, test and selected acquisition programs in support of Command, Control Communications and Intelligence (C^3I) activities. Technical and engineering support within areas of technical competence is provided to ESD Program Offices (POs) and other ESD elements. The principal technical mission areas are communications, electromagnetic guidance and control, surveillance of ground and aerospace objects, intelligence data collection and handling, information system technology, ionospheric propagation, solid state sciences, microwave physics and electronic reliability, maintainability and compatibility.